Utrecht University

Variability of pathways of deep water transport to the Denmark Strait

Author:
Daphne van Zanten

Daily Supervisor:
Dr. Femke de Jong (NIOZ)

Supervisor:
Prof. Dr. Leo Maas (IMAU / NIOZ)

Second Examiner:
Dr. Erik van Sebille (IMAU)

A thesis submitted in fulfillment of the requirements
for the degree of Master of Science in Climate Physics

October 16, 2019

Variability of pathways of deep water transport to the Denmark Strait

What is the role of the separated East Greenland Current and the North Icelandic Jet? What are the corresponding hydrographic properties? What is the driving force behind changes of the pathways over time?

Daphne van Zanten
Student number: 6191703

February - October, 2019

Daily Supervisor: Dr. M.F. de Jong
Tenure-track scientist, Department of Ocean Systems
Royal Netherlands Institute for Sea Research (NIOZ)
Den Burg, The Netherlands

Supervisor: Prof. dr. L.R.M. Maas
Professor, Institute for Marine and Atmospheric Research Utrecht (IMAU)
Utrecht University

Second Examiner: Dr. E. van Sebille
Associate Professor, Institute for Marine and Atmospheric Research Utrecht (IMAU)
Utrecht University

Abstract

The Atlantic Meridional Overturning Circulation (AMOC) contributes to the large-scale transport of heat and salt by water in the North Atlantic Ocean. In this project, we investigated the pathways and sources of the Denmark Strait Overflow Water (DSOW). The DSOW is the dense water which flows through the Denmark Strait (DS) over a sill. Model data described by Köhl et al. [2007] is used to investigate these pathways and corresponding hydrographic properties. Virtual particles are released using a particle tracking simulation called OceanParcels [Delandmeter and van Sebille, 2019] and resulting trajectories are investigated.

The results show the connection between the DSOW and the East Greenland Current (EGC), but do not show a stable main pathway over time between these. Both the North Icelandic Jet (NIJ) and the East Iceland Current (EIC) appear to be connected with the EGC. Moreover, it appears that the warmer path of the DSOW originates from the EGC, and the colder path from the NIJ. Some particles from the EIC may return near the Iceland shelf and flow back to the east side of the Kolbeinsey Ridge (KR). However, no differences in temperature between the east and west side of the KR are recognizable in the results of the trajectories. Additionally, no clear connection between the DSOW and the Iceland Sea gyre is found.

However, trajectories are found to be strongly fluctuating on a monthly time scale rather than inter-annual time scale. For this reason, mesoscale eddies and their influence are investigated in more detail in two locations by using an eddy tracking system of Nencioli et al. [2010]. First, the area around the DS is investigated, where relatively many anticyclonic eddies are found compared to the entire study area. The intermittent occurrence of eddies shows a strong relation with volume transport to the DS, as shown by potential vorticity and potential density. Second, a smaller area near the Spar Fracture Zone (SFZ) is investigated. The strengthening of an eddy, which is locked due to the topography, is found to be related to the diversion from the EGC into the EIC. To investigate if eddies are likely to be one of the responsible mechanisms for the variability of the sources and pathways into the DS, a confirmation by observational research is recommended, as well as further research into the possible mechanisms behind these eddies.

Lists of Acronyms

Instruments

ADCP	Acoustic Doppler Current Profilers
CTD	Conductivity Temperature Depth
RAFOS	Contrarywise of SOund Fixing And Ranging
RCM	Rotor Current Meters

Organizations

IMAU	Institute for Marine and Atmospheric Research Utrecht
NIOZ	Royal Netherlands Institute for Sea Research
NOAA	National Oceanic and Atmospheric Administration
UU	Utrecht University

Water masses

AAW	Arctic Atlantic Water
AW	Atlantic Water
DSOW	Denmark Strait Overflow Water
NADW	North Atlantic Deep Water
PW	Polar Water
rAW	return Atlantic Water

Currents

EGC	East Greenland Current
EIC	East Iceland Current
NAC	North Atlantic Current
NIIC	North Icelandic Irminger Current
NIJ	North Icelandic Jet
NwAC	Norwegian Atlantic Current
sEGC	separated East Greenland Current
shEGC	shelfbreak East Greenland Current

Topography

BB	Blosseville Basin
DS	Denmark Strait
GS	Greenland Sea
IS	Iceland Sea
JMFZ	Jan Mayen Fracture Zone
JMR	Jan Mayen Ridge
KR	Kolbeinsey Ridge
NS	Norwegian Sea
SFZ	Spar Fracture Zone

Remaining

AMOC	Atlantic Meridional Overturning Circulation
B-DS	Batch - Denmark Strait
B-EGC	Batch - East Greenland Current
OceanParcels	Ocean - Probably A Really Computationally Efficient Lagrangian Simulator
TS diagram	Temperature Salinity diagram

Contents

Acknowledgement

Presented here is my thesis, which is written in the context of my graduation internship at NIOZ, in collaboration with the IMAU, Utrecht University and is dedicated to the following people:

To start, I would like to thank Dr. Femke de Jong for her enthusiasm, time, input, project equipment, suggestions, discussions, "lab meetings", English lessons, quick and clear explanation to all my questions and of course the field work trips.

I would like to thank Prof. dr. Leo Maas for his patience and his positive approach to all my slides and descriptions I tried to give. Also, I would thank Dr. Erik van Sebille for his extensive software support. Additionally, without the chats about daily life, bakeries and feedback on my research of Nora, Elodie and Eva, I should almost forget that I got the chance to participate in the nice atmosphere of OCS, NIOZ within the lovely environment of Texel. Thank you.

Last, but definitely not least, I would like to thank Sebastian for the support since the beginning of my study until now, presumably the last part of this study. Without you, I would have given up the study during the first weeks and I would not have been able to use some more equipment and computer knowledge during this project and endless moral support during my stay at Texel. I learned a lot. To be continued, thank you.

1. Introduction

This chapter provides the required information to the main question of this project, which is divided into several sections. Some background information is given in section 1.1 and considering this information, an overview of the research area is described in section 1.2. Additionally, earlier studies, especially related to the currents and variability through the Denmark Strait, are summarized in sections 1.3 and 1.4, respectively. Finally, in section 1.5, the aim of this project is described, as well as the thesis set-up from chapter 2 and beyond.

1.1 Background information

To predict changes in climate, it is necessary to know how the Earth's climate system works. The climate system consists of various components which influence each other. One important part of the climate system is the ocean, in particular the transport of heat and salt between low and high latitudes by water. This large scale water transport is called the general overturning circulation, of which a sketch is shown in Figure 1.1. For the transport of water masses, several forcing mechanisms apply. One important mechanism is circulation forced by wind stress at the sea surface, where in the northern hemisphere, cyclonic (anticyclonic) winds induce upward (downward) Ekman pumping. Another important mechanism are density gradients which induce pressure gradients that are then driving part of the circulation. Depending on the area of interest, air-sea heat fluxes can play an important role related to the forcing of water masses. They can add or extract heat from the water masses, which influence the density. However, the mechanisms as described above affect each other [Kuhlbrodt et al., 2007].
There should be a clear distinction between water masses and currents. Water masses can flow by advection through a current. They can be identified by their hydrographic properties. Currents can be recognized by their velocity.

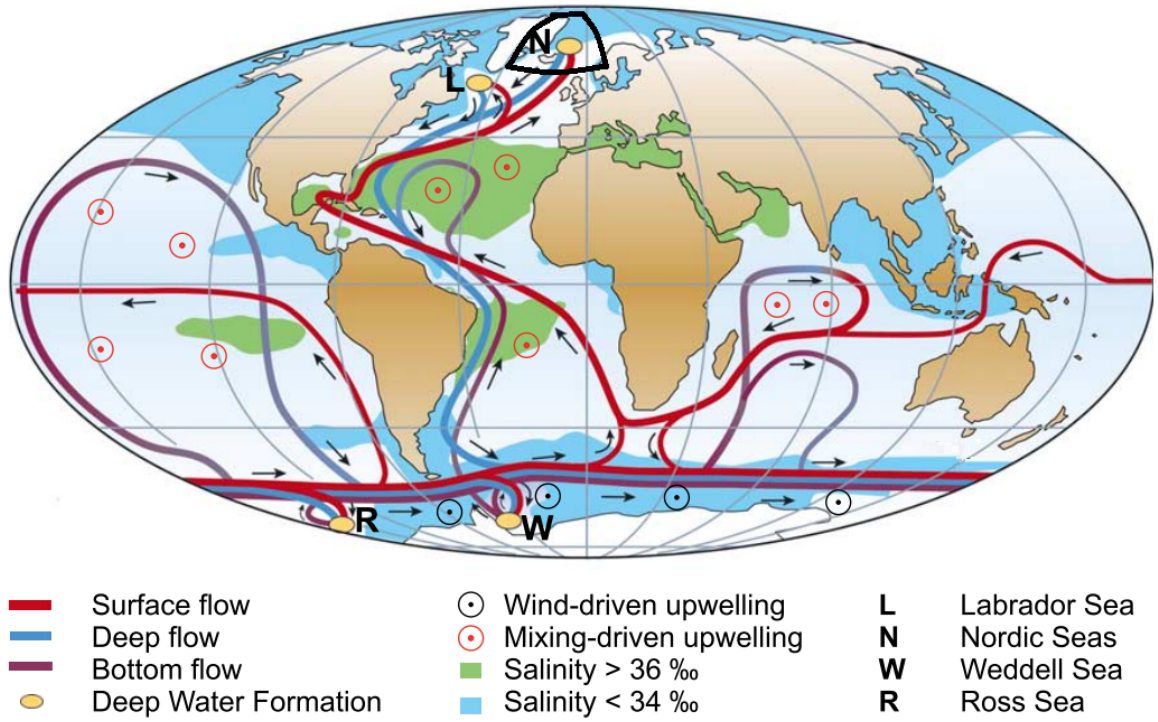

Figure 1.1: Sketch of the global overturning circulation, adopted from Kuhlbrodt et al. [2007]. The highlighted area is investigated in this project.

In Figure 1.1, warm, saline surface water flows are marked as a red line. Near the poles, heat loss takes place and the water becomes colder and denser, which refers to the deep water formation or deep convection. The combination of cold and saline water corresponds to an increase in density, which results in an overturning cell. The remaining cold water masses are the deep overflow waters, as illustrated by the blue line [Kuhlbrodt et al., 2007]. In this project, we focus on the North Atlantic and zoom into a small part of the Atlantic Meridional Overturning Circulation (AMOC), where the North Atlantic Deep Water (NADW) is formed, as indicated in Figure 1.1 with a yellow dot (N). The deep branch of the AMOC flows through the Denmark Strait (DS), as indicated in Figure 1.3, which is the main area investigated within this project.

1.2 Overview of the research area

A new circulation scheme of the transport of heat and salt water at the AMOC was proposed by Mauritzen [1996] which was based on previous data sets from the Nordic Seas and the Arctic Ocean. This scheme is schematically shown with coloured lines in Figure 1.2. The area of Figure 1.2 is related to the highlighted area in Figure 1.1.

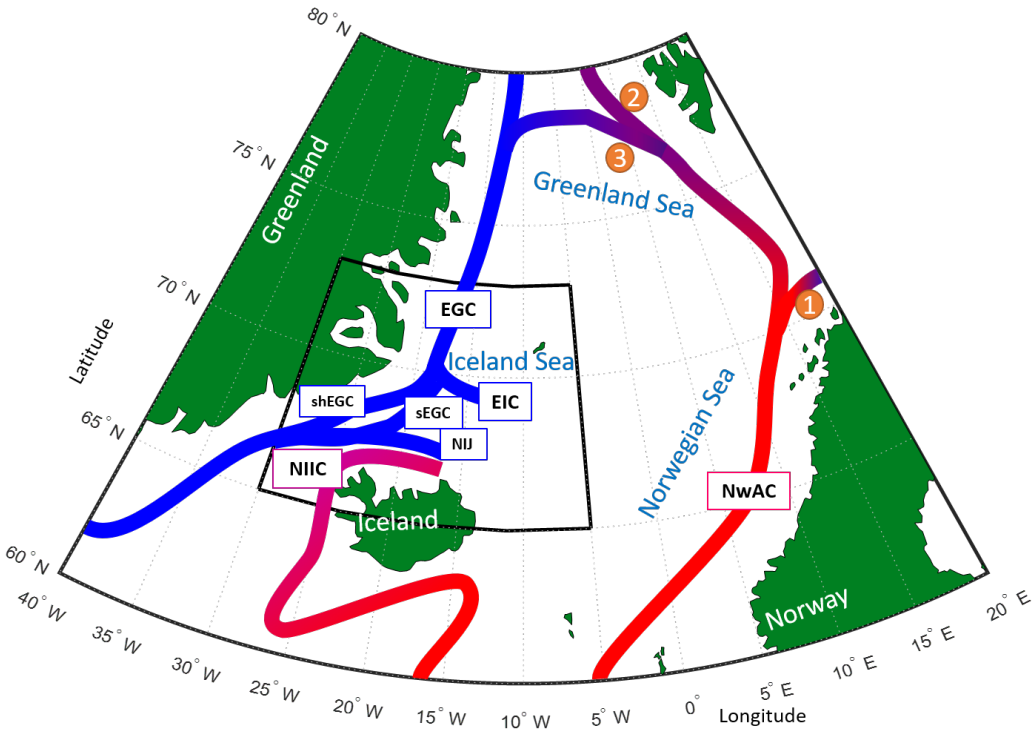

Figure 1.2: General pathways of the currents of the AMOC, based on the circulation scheme of Mauritsen, 1996. Reddish lines are related to warm, saline water. Bluish lines are related to cold, fresh water. Acronyms: East Greenland Current (EGC), East Iceland Current (EIC), separated East Greenland Current (sEGC) and shelfbreak East Greenland Current (shEGC), Norwegian Atlantic Current (NwAC), North Icelandic Jet (NIJ) and North Icelandic Irminger Current (NIIC). Numbers are related to locations where the Atlantic Water (AW) bifurcates.

The upper limb of the AMOC transports heat northward from the subtropics to the poles. As part of the AMOC, warm water flows through the North Atlantic Current (NAC). The Norwegian Atlantic Current (NwAC) and the North Icelandic Irminger Current (NIIC) can be distinguished from each other, as visible in Figure 1.2. Both currents, the NwAC and the NIIC, originate from the NAC. The NwAC continues through the Norwegian Sea, while

the NIIC flows northward along the western side of Iceland. Following the NwAC further north, around the Greenland Sea, heat is lost to the atmosphere. While cooling, the water gets denser and is then transported southward with the East Greenland Current (EGC), as marked by the blue line. North of Iceland, the EGC divert to the East Iceland Current (EIC), which flows eastward through the Iceland Sea. Another part will flow southward and bifurcates in the shelfbreak EGC (shEGC) and the separated EGC (sEGC). Right in front of the sill, the shEGC, sEGC and the North Icelandic Jet (NIJ) come together, as visible in Figure 1.2. The topography of the area within the black box of Figure 1.2 is plotted in Figure 1.3, by using data of the National Geophysical Data Center [2016].

The DS is the area around the shallow sill, highlighted with the red ellipse, between Greenland and Iceland. The Denmark Strait Overflow Water (DSOW) is defined as the dense water which flows south-westward over the sill. The DSOW is generally described by a potential density anomaly, $\sigma_0 > 27.8\ kg/m^3$ [Brown and Dickson, 1994]. Where σ_0 is the reference potential density anomaly $[kg/m^3]$, hereafter called the potential density. In earlier research, the EGC is suggested as the primary source of water for the Denmark Strait [Helland-Hansen and Nansen, 1909, Mauritzen, 1996, Rudels et al., 1999]. However, the currents in the Iceland Sea and their variability to the contribution of the DSOW still remain uncertain.

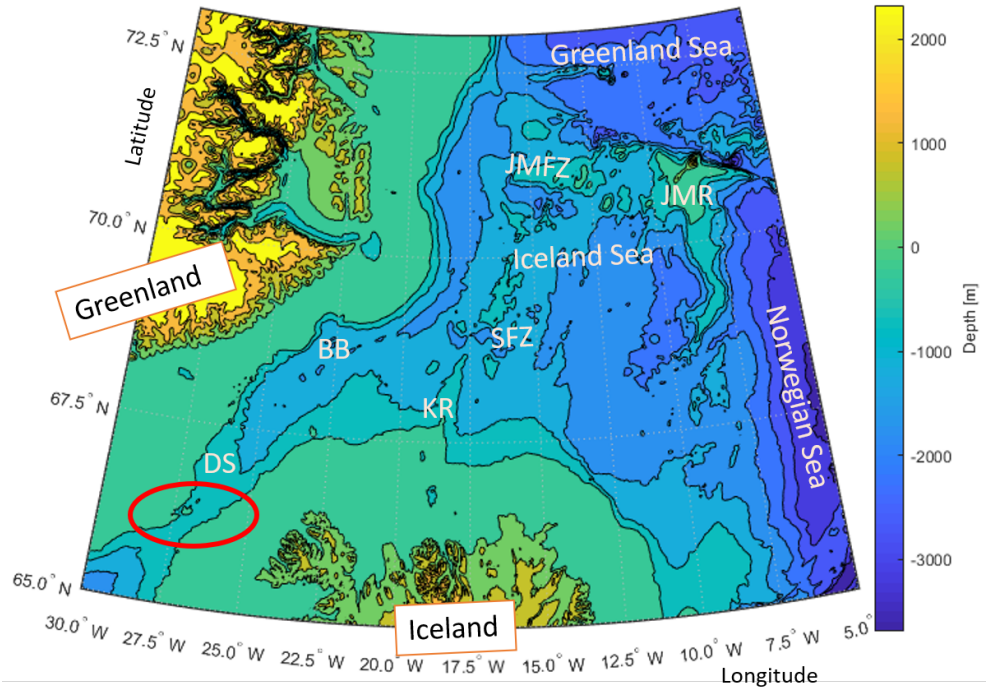

Figure 1.3: Bathymetry of the area as visible within the black box from Figure 1.2. The red ellipse highlights the sill. Isobaths are drawn every 500 meters. Colours are corresponding to depths within the legend [National Geophysical Data Center, 2016]. Acronyms: Denmark Strait (DS), Blosseville Basin (BB), Kolbeinsey Ridge (KR), Spar Fracture Zone (SFZ), Jan Mayen Fraction Zone (JMFZ) and the Jan Mayen Ridge (JMR).

Additional interesting areas in Figure 1.2 are the Blosseville Basin (BB), located slightly north of the Denmark Strait sill. The ridge north of Iceland is known as the Kolbeinsey Ridge (KR). The topographic area around Spar Fracture Zone (SFZ) has large gradients in depth, which likely influences the currents. The Jan Mayen Fraction Zone (JMFZ) and the Jan Mayen Ridge (JMR) can be found north of the Iceland Sea.

1.3 Currents in the area of the Denmark Strait

Previous studies investigate the main sources and pathways of water masses to the Denmark Strait. Earlier research related to the EGC, EIC, NIJ and NIIC are summarized briefly in subsections 1.3.1, 1.3.2, 1.3.3 and 1.3.4 respectively.

1.3.1 East Greenland Current

The Atlantic Water (AW) has a subtropical origin and flows northward through the NAC, as reported by Mauritzen [1996]. In the NAC, the AW is a surface water mass between 500 and 600 meters thick, with typical values for potential density between 27.4 and 27.8 kg/m^3, a potential temperature higher than 3°C and salinity of 35.0 or more [Mauritzen, 1996]. In this research the unit of salinity is a Practical Salinity Unit (PSU), which is dimensionless. Further north, the AW is modified and becomes colder due to atmospheric cooling. In addition, the salinity is reduced, potentially due to the ratio of precipitation versus evaporation, the fresh-water run-off from Scandinavia and mixing with the gyres, as described by Mauritzen [1996]. Hydrographic properties change the AW as a result of different branches, as indicated by numbers in Figure 1.2. One branch flows north-eastward (1). Thereafter the AW bifurcates into the return Atlantic Water (rAW)(2) and the Arctic Atlantic Water (AAW)(3). The AAW goes through both the Atlantic and Arctic regions. In contrast to the AAW, the rAW does not pass through the Arctic. Both water masses mix with surrounding waters on their way. Consequently, the rAW and AAW can be distinguished from each other by differences in temperature and salinity. As a result of modification through air-sea heat fluxes and mixing within the fresher Arctic waters, the AAW is colder compared to the rAW, and less dense. However, the modification of the AW into the AAW occurs predominantly along isopycnals [Mauritzen, 1996]. The AAW becomes colder due to mixing with the Polar Water (PW) in the Arctic Ocean. The AAW is considered as an intermediate water, found between roughly 300 and 500 meters depth. The potential density of Polar Water (PW) is found to be less than 27.8 kg/m^3 and the salinity is less than 34.5. The PW is typically found near the surface [Mauritzen, 1996]. Figure 1.4 shows observational data from the Polarstern cruise along the coast of Greenland, where the AAW, rAW and the PW are highlighted.

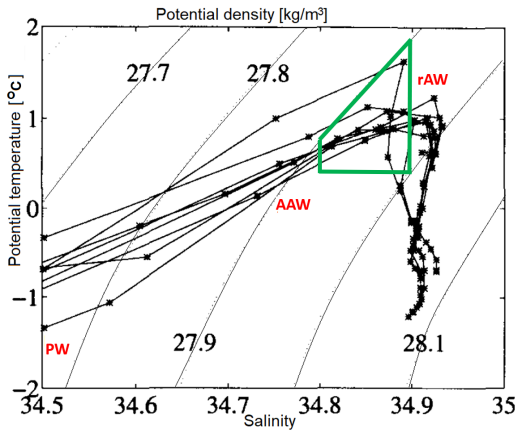

Figure 1.4: Measurements from Polarstern cruise (1988) along the coast of Greenland [Mauritzen, 1996]. Areas with characteristic values for the Arctic Atlantic Water (AAW), return Atlantic Water (rAW) and Polar Surface Water (PSW) are signed. The green contour is related to the properties found in the DSOW, as indicated by Mauritzen [1996].

According to Mauritzen [1996], it was found that the AW has a salinity maximum as it enters the EGC, typically higher than 34.9. Considering these observations, a suggestion was made that the AAW, rAW, or both water masses are responsible for this difference in salinity. However, hydrographic properties of the DSOW are observed within the area of the DS. The salinity was found to be between 34.8 and 34.9 and a potential temperature between 0.4 and 2.0 degrees Celsius, as indicated by the green contour in Figure 1.4. (Mauritzen [1996] used data from the following publications: [Erika Dun, 1962, Worthington and Wright, 1970], Hudson, 1967, Grant, 1968, Knorr 1981 (TTO/NAS), Knorr, 1983], [McCartney, 1992].) Comparing observations of the AAW, rAW and PW, as shown in Figure 1.4, with properties observed in the DS, it is likely that the rAW contributes to the DSOW. The hydrographic properties considered by the research of Mauritzen [1996] are summarized in Table 1.1.

Table 1.1: Overview of hydrographic properties of water masses as considered by Mauritzen [1996].

Name	**Depth**	σ $[kg/m^3]$	Θ $[°C]$	S [–]
AW	surface water 500-600 m thick	27.4-27.8	>3	>35
PW	50-100 m	<27.8	>0.5	<34.5
rAW	between 200-600 m	>27.9	>0.5	>34.9
AAW	under PW, 100m thin between 300-500 m	∼28	<0.5	<34.9
DSOW	over sill at ∼600m		0.4-2	34.8-34.9

Additionally, Van Aken and de Jong [2012] investigated salinity and temperature of the core of the DSOW using hydrographic observations south of the DS. They found weekly to decadal variations in these hydrographic properties. However, the mechanisms and effects of the causes were still questioned.

Combining historical in-situ data, an idealized numerical model and atmospheric reanalysis surface wind fields, the circulation and water mass transports north of the Denmark Strait were investigated by Våge et al. [2013]. They found that as the EGC approaches Denmark Strait, it bifurcates into two branches: the shelfbreak EGC (shEGC) and the separated EGC (sEGC), as indicated in Figure 1.2. Two mechanisms were proposed [Våge et al., 2013]. First, the sEGC can be the offshore branch of an anti-cyclonic gyre, which is formed due to a combination of a negative wind stress curl and a large gradient in the bathymetry of the BB. Secondly, the bifurcation can be eddy-forced, suggested by an idealized numerical simulation.

1.3.2 East Iceland Current

A study of Swift et al. [1980] proposes that the central Iceland Sea may receive water from both the west and the north-east. Since the EIC diverts with the EGC, the EIC carries a part of the fresh Arctic surface waters into the Iceland Sea, as visible in Figure 1.2. Current meters and Conductivity, Temperature and Depth (CTD) measurements were used within the EIC for one year, to gain more information of the EIC by Jónsson [2007]. During this time, the average of the fresh water flux (considered above 170 meters) was calculated to be 5.5 mSv (where 1 Sv = 10^6 m^3/s). Investigation about the long term variability in volume transport was done by Macrander et al. [2014], who concluded the existence of a large inter-annual variability in freshwater transport. They suggest that this depends on more local conditions like sea ice, variability in values of salinity related to the inflow of AW.

Additionally, they concluded that the strength of the EIC was related to changes in local wind stress north-east of Iceland. However, the freshwater transport of the EIC is considered to be small compared to the export in the EGC [Macrander et al., 2014].

1.3.3 North Icelandic Jet

Våge et al. [2011] suggested the existence of an additional deeper jet which is flowing from the east southward to the DS, centered at a depth of approximately 650 meter. This jet is called the NIJ and is indicated in Figure 1.2. However, Våge et al. [2011] suggested that the inflowing NIIC forms eddies which are cooled by the atmosphere. Subsequently, they disintegrate in the Iceland Sea gyre. This colder water is denser and Våge et al. [2011] suggested that this water flows back to greater depths to form the NIJ. This suggestion is schematically drawn by Våge et al. [2013], as shown in Figure 1.5.

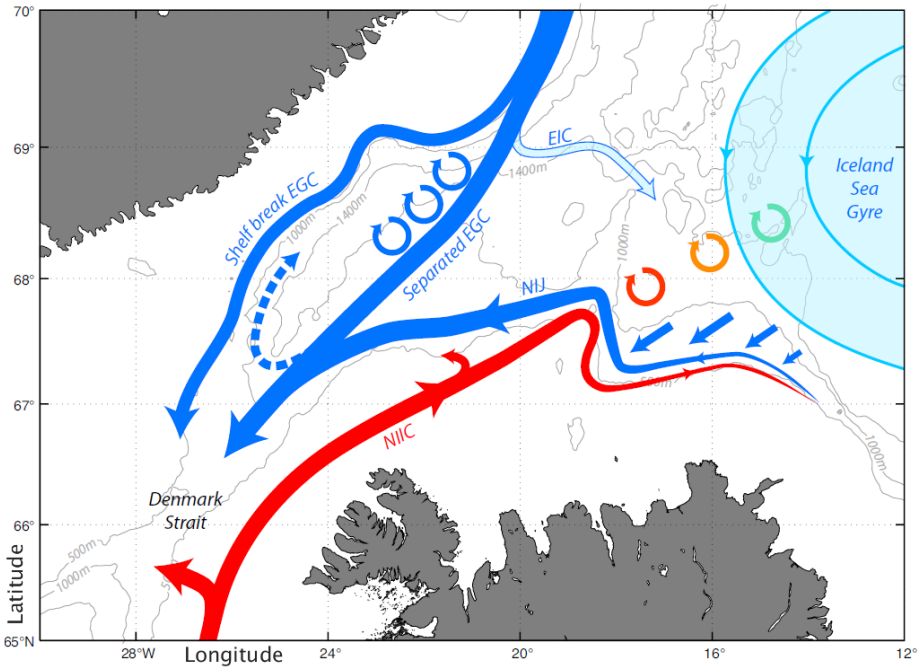

Figure 1.5: Suggested circulation scheme by Våge et al. [2013]. They propose that the sEGC forms anti-cyclonic eddies (blue circles). They also suggest that the NIIC becomes weaker, due to the advection of warm water, which cools and partly turns back into the NIJ.

Additional research by Huang et al. [2019] using mooring data between 2011 and 2013 concluded that there was a strong NIJ present occasionally present, coincident with a weak sEGC. The strong NIJ is related to the heat fluxes originating from the atmospheric forcing upstream of the DS [Huang et al., 2019].

1.3.4 North Icelandic Irminger Current

The NIIC transports warmer surface water northward from the NAC through the Denmark Strait [Helland-Hansen and Nansen, 1909], as visible in Figure 1.2. Valdimarsson and Malmberg [1999] presented a research of satellite tracked surface drifters, which showed a pathway from the NIIC back to the DSOW. It was suggested that the main flow appears to join the EGC back into the DS, after passing the KR. Additional results of Valdimarsson and Malmberg [1999] reveal the seasonal as well as inter-annual variability of the surface currents.

Moreover, a study by Pickart et al. [2017] using shipboard hydrographic and velocity data between 2004 and 2013 for different seasons results in a correlation between the NIJ and NIIC. Ypma et al. [2019] released particles in two different models and compared the results. Both models indicate that the connection between the NIIC and the DSOW is not as strong as suggested by observations. Additionally, by comparing results of mooring arrays, CTD data and a numerical model, it was found by Zhao et al. [2018] that seasonal changes of the NIIC are mainly due to changes in wind stress. They suggest that this is related to the wind-driven AW transport, which is a consequence of the location of the center of the cyclonic rotation around Iceland (also called Icelandic low).

1.4 Variability of the Denmark Strait Overflow Water

Earlier results of investigations of the variability related to the DSOW (water denser than 27.8 kg/m^3) are summarized briefly in this section. Dickson and Brown [1994] found a stable volume transport of about 2.9 Sv southward over the sill on time scales longer than weeks, from observational data and earlier research.

Measurements from Rotor Current Meters (RCM) and CTD measurements, deployed at the DS since 1987 and 1988 respectively, were analysed by Jónsson [1999]. There was no sign of recirculation of a part of the EGC found in the DS. Additionally, little to no variability at a time scale longer than a few days was found in the DSOW and the Iceland Sea, in contrast to a higher variability of the EGC. This suggests that the Iceland Sea provides a large part of the overflow water. Since several CTD measurements at the DS and EGC in 1997 and 1998 did not agree with the suggestion as stated above, this suggestion was rejected by Rudels et al. [2002]. Rudels et al. [2002] concluded that the AW, modified by isopycnal mixing with the Greenland and Iceland seas is comprised of the densest part of the DSOW. Subsequently, diapycnal mixing takes place around the sill and the overflow plume descending south of the sill.

However, a comparison by Rudels et al. [2003] of several hydrographic observations in the early 1990s led to the suggestion that sources of the DSOW are switching, with changes in the hydrographic characteristics at various time scales, from weekly up to a hundred years. Reasons for switching sources were suggested to be changes in weather conditions and wind fields or variations in the characteristics of the water masses. Additionally, inter-annual fluctuations of the DSOW specifically have been observed by Macrander et al. [2005] between 1999 and 2003 by comparing data of various ship-occupied sections and a numerical model experiment. The calculated volume transport decreased from 3.68 Sv to 3.07 Sv, which is more than 20 percent. This was coincident with a temporary temperature increase of about 0.5 degrees Celsius.

From 1996 to 2004, Jochumsen et al. [2012] monitored the velocity by using two moored Acoustic Doppler Current Profilers (ADCP) at the sill of the DS. Gaps were filled by a model, based on the daily data. This resulted in a mean overflow transport of 3.4 Sv $\pm$ 1.4 Sv, in south-west direction. No significant trend was detected in the time series, which was in contrast with the previous observation of Macrander et al. [2005]. The variability was linked to eddies and no relationship with wind stress curl was found [Jochumsen et al., 2012]. Five additional mooring arrays were deployed in 2014 and 2015. With this new information, the mean DSOW transport is estimated to be 3.2 Sv $\pm$ 1.5 Sv [Jochumsen et al., 2017].

Harden et al. [2016] used data from mooring arrays around a 24°W, 68°N, which is north of the sill. Using data from these moorings between September 2011 and July 2012, calculations were done of the mean transport of the DSOW. Results are summarized in Table 1.2.

Harden et al. [2016] propose that the DSOW consists of mainly the shelfbreak EGC, sEGC

Table 1.2: Results from research of Harden et al. [2016]

Mean Volume Transport [Sv]			st dev [Sv]
sEGC	1.04		0.15
shEGC	1.5	+	0.16
EGC	2.54		0.17
NIJ	1	+	0.17
DSOW	3.54		0.16

and the NIJ, where the NIJ and the sEGC come together at a respective location, which is time-dependent. Moreover, the shelfbreak and sEGC display a variability on periods of longer than two weeks that are anti-correlated [Harden et al., 2016]. The suggested source of this variability is wind forcing, because an association was found between the gyre-like circulation in the BB and the wind stress curl by using atmospheric reanalysis fields. Håvik et al. [2017] used several sections of CTD and ADCP data through the EGC, between the DS and the Greenland Sea, to estimate the total overflow transport at the shelfbreak EGC. This was estimated to be 2.8 $\pm$ 0.7 Sv, which agrees with the previous results of Harden et al. [2016].

The overflow transport was also investigated by Behrens et al. [2017] using a numerical model. Their overflow transport estimate is 1.5, 1.1 and 0.86 Sv for the shelfbreak EGC, sEGC and NIJ, respectively, which overlaps with observational results. While the volume transport of the sEGC and NIJ seems to be stable, the shelfbreak EGC shows a variability. This correlates with the strength of a wind stress curl. Likewise, no exchange with the interior of the Iceland Sea is found and most water of the NIJ originates from the sEGC [Behrens et al., 2017].

Another type of variability was investigated by von Appen et al. [2017] in the area north of the DS. These mechanisms were called "boluses" and "pulses". They mainly used observational data from a mooring array, deployed on the sill of the DS between 2005 and 2011. A bolus is defined as a mesoscale feature which is a relatively cold, cyclonic weakly stratified intermittent lens, which occurs every 3.4 days. A pulse is defined as a relatively warm, anti-cyclonic vortex, with a stronger increase in along-stream velocity compared to a bolus, occurring every 5.4 days [von Appen et al., 2017]. Boluses were observed by Mastropole et al. [2017] in 41 percent of transects from observational data near the sill. In a model study of Almansi et al. [2017], boluses and pulses are also detected, occurring every 3.2 and 5.5 days, respectively. Additionally, an increase of 30 percent of the yearly mean southward volume flux is estimated in the presence of boluses and pules, were argued to play a major role in controlling the variability of the transport [Almansi et al., 2017].

1.5 Purpose of this project

The switching sources of the DSOW and its variability is still questioned. Results of an observational study and a model study are summarized in this section. These studies contain the main background information for the motivation of this project, described at the end of this section, as well as the thesis set-up.

To identify the possible mechanisms that control changes in DSOW, a model simulation was made by Köhl et al. [2007]. With this model, the transport through the DS is estimated as 2.5 Sv, which is lower than estimates from observations. Additional results from this model can be categorized by time scales. On seasonal and longer time scales, a change of circulation pattern north of the sill is related to a decreasing capacity of the dense water reservoir, linked

to the overflow anomalies. On annual and shorter time scales, the barotropic flow through the DS is determined by the barotropic circulation around Iceland, related to the wind stress curl. During a high wind stress curl, the cyclonic circulation in the Iceland Sea intensifies and the rAW mixes within the Iceland Sea. In 1999, a high wind stress curl was present, when the EGC was found to be a source of the DSOW, related to the relatively cold, fresh and less dense water. In contrast, relatively warm and saline water was found in 1994 and 2003, when the Iceland Sea is considered as a main source of the DSOW, related to a low wind stress curl [Köhl, 2010]. So, during a low wind stress curl the cyclonic circulation relaxes and the rAW mixes within the EGC. Furthermore, on seasonal and annual time scales, variations of transport are determined by both the barotropic and overflow components [Köhl et al., 2007].

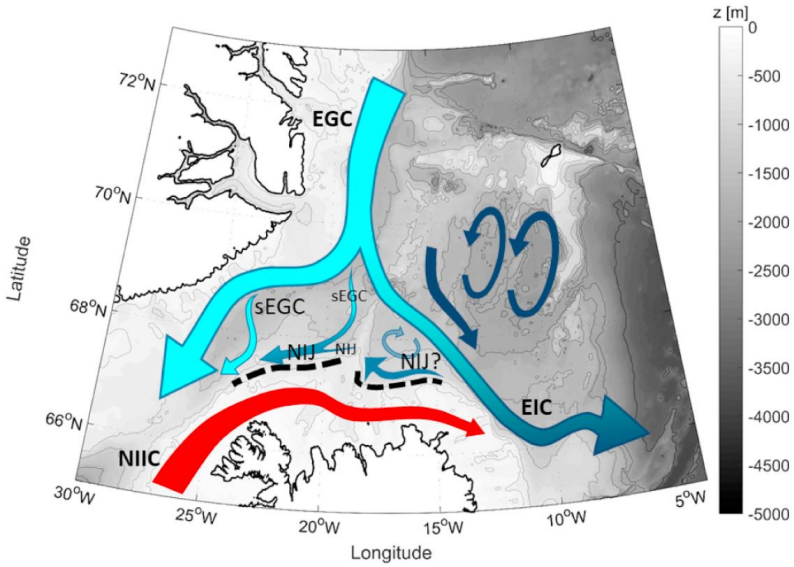

Figure 1.6: New schematic map of currents incorporating information from float experiments, adopted from De Jong et al. [2018]. Areas of up-slope motion are indicated with the thick dashed black lines. The blue arrow is related to cold, fresh water coming from the north. The red arrow is related to warm, saline water coming from the south. Acronyms: separated East Greenland Current (sEGC), East Iceland Current (EIC), North Icelandic Irminger Current (NIIC), North Icelandic Jet (NIJ).

To analyse the pathways of dense waters upstream of the sill of Denmark Strait, RAFOS floats were deployed in the Iceland Sea in July of 2013 and 2014 [De Jong et al., 2018]. The tracked RAFOS floats were developed from SOund Fixing And Ranging (of which RAFOS is the reverse) floats [Rossby et al., 1986], ballasted for 500-dbars, to drift at a target depth of about 500 meters. Analysis of the trajectories did not show a direct connection between the interior Iceland Sea and the DS overflow. Instead, floats deployed in the area around the KR were moved upslope rather than being advected horizontally from east to west of the KR. However, the float tracks show a clear connection between the EGC and the NIJ west of the KR. The pathway associated with the sEGC was also shown by the floats [De Jong et al., 2018]. A schematic map of the currents identified in this project is shown in Figure 1.6. Subsequently, the main question of this project follows:

"What mechanisms are responsible for the variability of the sources and pathways of the Denmark Strait Overflow Water?"

Since the DSOW seems to origin mainly from the north of the sill, we focus on this area. Consequently, several sub-questions arise:

- *What is the role of the separated East Greenland Current and the North Icelandic Jet?*
- *What are the corresponding hydrographic properties?*
- *What is the driving force behind changes of pathways over time?*

The conducted project is described in this report, which is organized as follows; Chapter 2 describes the data used. In chapter 3, several methods are explained, which are used to analyse and compare the available data. Chapter 4 describes the results of this project. Subsequently, in chapter 5 and 6 the results will be discussed and concluded, respectively.

2. Data

To answer the main question of this project, observational data is compared with model data. While observational data used in this study is only available on a short time scale, the model data covers a significantly longer time period. A description of the observational data is given in section 2.1, followed in the model data in section 2.2. Scales of the data are considered in section 2.3. Finally, a validation of the model data is described in section 2.4.

2.1 Observational data

Several observations are used in this project, including CTD measurements and tracked trajectories with RAFOS floats, which are both described in this section.

Hydrographic measurements were made with the Sea-Bird 911+ CTD instruments in 2011 and 2012. The instruments measure conductivity, temperature and pressure and with these properties, the depth, salinity and density can be calculated. These instruments are deployed from a scientific research vessel. The CTD measures a vertical profile at one location. Accuracies are estimated to be ± 0.3 dbar for pressure, ± 0.001 °C for temperature and ± 0.002 for salinity [Våge et al., 2013]. Locations of the CTD arrays are shown in Figure 2.1. Yellow and red dots are related to the locations of the CTD measurements in 2011 and 2012, respectively. Near the sill of the Denmark Strait, CTD measurements are available for both years.

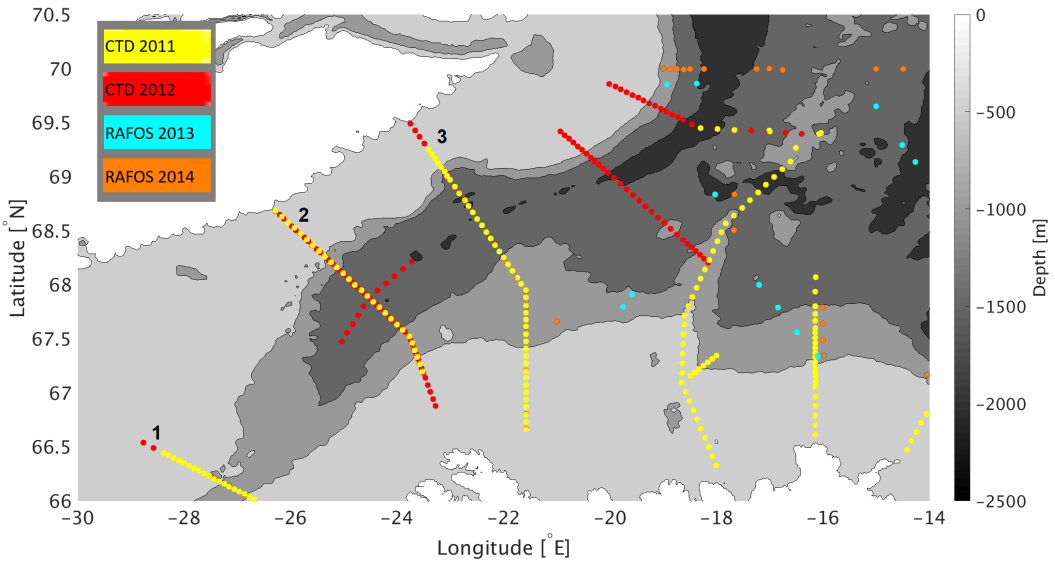

Figure 2.1: Overview of locations and the data sources of the measurements for this study. Red and yellow dots are related to CTD measurement locations, blue and orange dots are related to launch positions of RAFOS floats. Isobaths drawn at every 500 meters. Other colours are corresponding to the depths within the legend. Highlighted sections are Svalvogar (1), Fjallaskagi (2) and Kögur (3), where CTD measurements where done in both years, 2011 and 2012.

RAFOS floats were deployed in July 2013 and July 2014. These floats flow along with the current, generally at around 600 meters depth, to investigate the DSOW. The floats receive signals twice a day from six moored sound sources, to measure the position with an accuracy of ±2 km. The temperature and pressure are measured with accuracies of ± 0.005 °C and ± 5 dbar, respectively [De Jong et al., 2018]. Positions where the RAFOS floats were launched are visible in Figure 2.1, where the cyan colour is related to floats deployed in 2013 and orange are coordinates of floats released in 2014. Examples of some tracks of the RAFOS floats are shown in Figure 2.7 and explained in section 2.4.1. While CTD data measures at a fixed location (Eulerian approach), the RAFOS floats is a method of investigating pathways (Lagrangian approach).

2.2 Model data

Model data provided by Dr. Armin Köhl of the University of Hamburg is used to release virtual particles and compare results with the observational data. The model is described in Köhl et al. [2007]. The output of the simulation of Köhl is based on the Massachusetts Institute of Technology (MIT) ocean general circulation model [Marshall et al., 1998]. Between 2 January 2005 and 28 September 2016, properties with a 3 day interval are available. The available properties are velocity in three directions, salinity and temperature. The model has a resolution in latitude of 0.04° and in longitude of 0.1°, which is roughly 4 by 4 kilometers. The model grid used in this project extends from 66°N to 72°N and 36°W to 8°E. The 30 vertical levels exists from 5 to 4618 meters, ranging from 11 meters close to the surface to 500 meters at a greater depths. Figure 2.3 shows an example of the grid points from the model data. Figure 2.2 shows an example of a horizontal slice of model data. At a depth of 547 meters the mean velocities of the entire time series are shown.

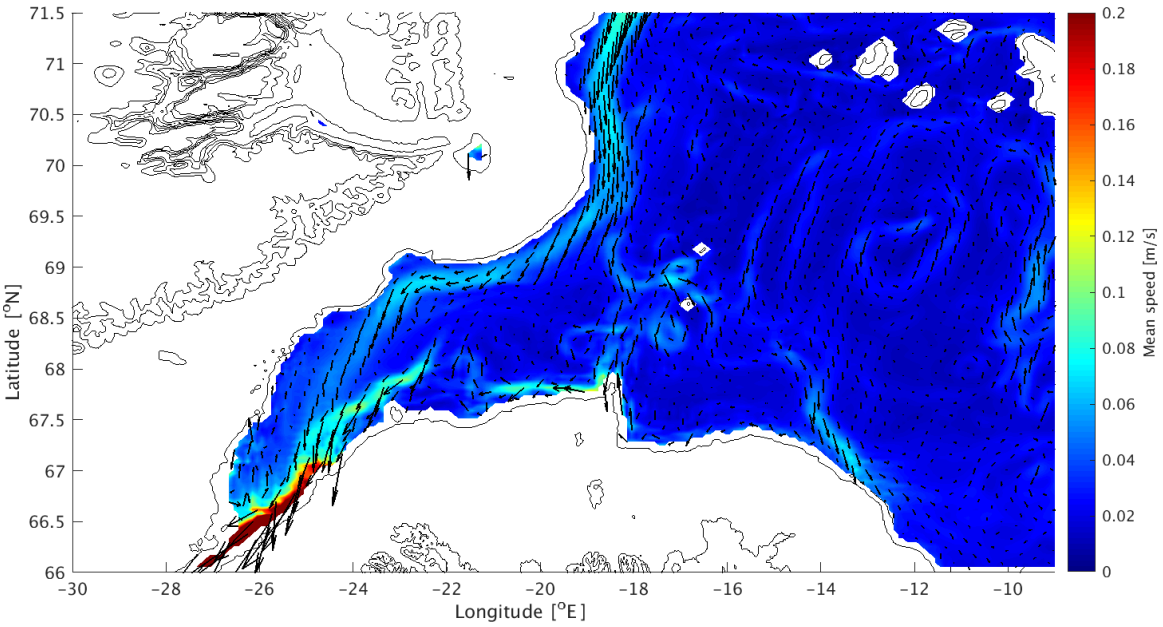

Figure 2.2: Map of the mean velocity between 02-01-2005 and 28-09-2016 at 547 meters from model data. Arrows give the mean direction of the velocity. The length of the arrows and the colours both corresponding to the strength of the velocity.

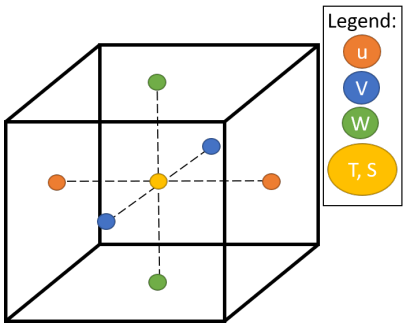

Figure 2.3: An example of the output of data from the model of Köhl et al. [2007] on a grid.

2.3 Scaling

To consider processes in the ocean, scales are important. Geostrophic eddies can be resolved by using the resolution as described above and visible in Figure 2.4 [Cushman-Roisin and Beckers, 2011]. Red lines correspond to the characteristic scales. The characteristic length is between ±4 km (grid step) and ±1000 km (total coverage). The characteristic time scale is between 3 days (grid step) and 10 years (total coverage). As shown in Figure 2.4, typical scales of geostrophic eddies in oceans, are:

- Length scale; $L = 5 - 2000$ km
- Velocity scale; $U = 0.1 - 1$ m/s
- Time scale; $T = days\ to\ years \approx 1 * 10^6 - 1 * 10^8$ s

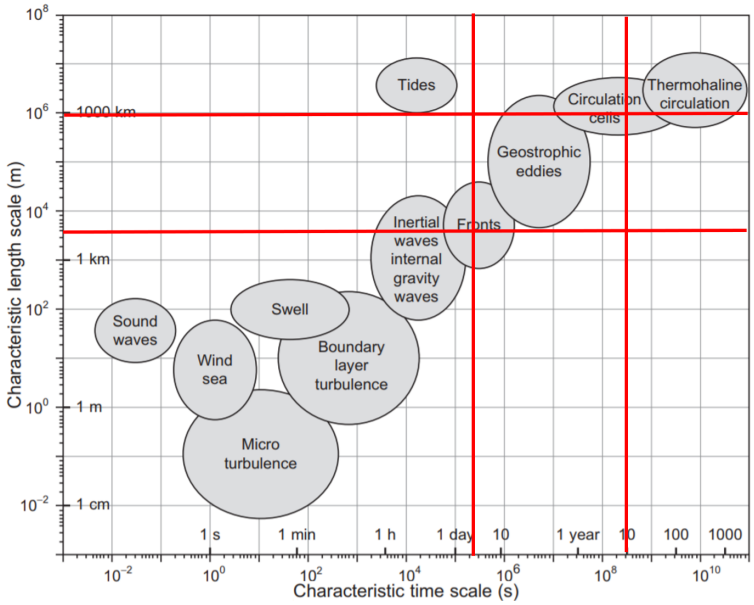

Figure 2.4: Various types of processes and structures in oceans with corresponding scales, adopted from [Cushman-Roisin and Beckers, 2011]. Red lines correspond to the grid of model data by [Köhl et al., 2007].

Large-scale geophysical flows have a small aspect ratio, which is the scale height divided by scale length, as well as a small ratio of the scale velocity in x and y direction divided by the scale velocity in z direction. However, scales of eddies described above are mostly considered as mesoscale phenomena, where the ratios become bigger.

Rotation is important if the rotation parameter ϵ is in the order of or less than one ($\epsilon \leq \mathcal{O}(1)$) [Cushman-Roisin and Beckers, 2011]. This means that the time of one revolution of the earth is smaller compared to the distance that a particle covers within a respective time, so the trajectory is probably influenced by ambient rotation. Using the typical scales of eddies in oceans, the equation can be written as equation 2.1;

$$\epsilon = \frac{2\pi U}{\Omega L} \approx \frac{2\pi * 0.5}{7.2921e-5 * 5e4} \approx 0.9 \tag{2.1}$$

Where Ω is the ambient rotation rate of the Earth [$\approx 7.2921 * 10^{-5}$ rad/s]. The result of $0.9 \approx \mathcal{O}(1)$ means that rotational effects are important. Stratification is important if the stratification parameter σ, is in the order of or slightly less than one ($\sigma \leq \mathcal{O}(1)$ [Cushman-Roisin and Beckers, 2011]. This means that the potential energy is larger compared to the

kinetic energy. The potential energy can perturb stratification effects and thereby modify the flow field. Using the typical scales of eddies in the oceans again, the equation can be written as equation 2.2;

$$\sigma = \frac{\frac{1}{2}\rho_0 U^2}{\Delta\rho g H} \approx \frac{0.5 * 1027 * (0.5)^2}{0.4 * 9.81 * 550} \approx 0.06 \tag{2.2}$$

Where a density, ρ, is taken to be 1027 $[kg/m^3]$. The difference in density is in the order of $\Delta\rho$ 0.4$[kg/m^3]$ and a depth scale H of 550 $[m]$ is taken for this project. The result of $0.06 \leq \mathcal{O}(1)$ means that stratification has to take into account. As a result, this study takes both rotation and stratification into account. Finally, the Rossby number compares advection to the Coriolis force, as written in equation 2.3;

$$Ro = \frac{U}{\Omega L} \approx \frac{0.5}{7.2921e-5 * 5e4} \approx 0.1 \tag{2.3}$$

A result of $0.1 \approx \mathcal{O}(0.1)$ for the Rossby number means that the non-linear advective term of the momentum equations of Navier-Stokes is negligible. A balance remains between the Coriolis force and the pressure gradient force, also considered as a geostrophic balance for a homogeneous fluid. However, the velocity is probably less at a depth of 500 meters, which means the Rossby number becomes even smaller. Consequently, the non-linear advective term becomes smaller, which leads to a more convincing argument to neglect this term. Additionally, the currents in the ocean are not exactly homogeneous, which leads to the concept of stratification. Stratification is taken into account in the quasi-geostrophic equations. The Rossby radius is a measure of mesoscale variability, which can be used to investigate if a model can resolve eddies related to the model grid. Taking both stratification and rotation into account, the Rossby radius of deformation is calculated by equation 2.4.

$$R_d = \frac{\sqrt{g\frac{\Delta\rho}{\rho}H}}{f} \approx \frac{\sqrt{9.81 * \frac{0.4}{1027} * 550}}{2 * 7.2921e-5 * sin(67°)} \approx 10.8\ km \tag{2.4}$$

In this formula, the height $[m]$ is given by H and g is the constant gravitational acceleration $[m^2/s]$. The Coriolis parameter $[rad/s]$ is described as $f = 2\Omega sin(\phi)$, where ϕ is the latitude coordinate [°]. Since the Rossby radius of deformation is calculated to be approximately 10 kilometers, eddies can be resolved.

2.4 Validation of the model

This section is divided into two subsections. In section 2.4.1 model data is compared with a section of CTD data. In section 2.4.2, trajectories of particles released within the model data are compared with some trajectories of the RAFOS floats.

2.4.1 Model data versus CTD

To validate the suitability of the model for this study, properties like salinity and density of several sections from the model data are compared with the CTD data. Figure 2.5 shows an example of two transects which show values of salinity and potential density. Corresponding results are shown in Figure 2.6, where in 2.6(a), a section of the model data is visible and 2.6(b) shows a section of the CTD data from 2012. The model data consist of mean values between 2005 and 2016. It should be noted that the values of density are more smooth as compared to the CTD data.

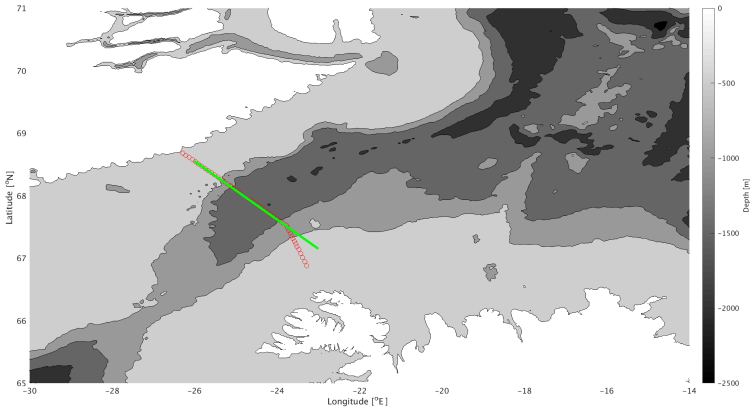

Figure 2.5: Map of sections of the model data (green line) and observational data (CTD, red dots)

Generally, isopycnals are found around approximately the same depth, drawn by green lines. Also, the structure is similar for both. A downward displacement of isopycnals is visible at the west side, as well as an upward displacement closer to the east. In this transect, the EGC is recognizable in the west, near the Greenland shelf, related to light, fresh water. The DSOW is related to the dense, saline water. More saline water is found in the upper east corner, as visible in Figure 2.6(b), which is related to the NIIC, indicated by the purple contour. Nevertheless, the pattern of salinity is considered similar, since in both figures, 2.6(a) and 2.6(b), fresh water is found in the east and is decreasing to both directions eastward and downward. The CTD data is more irregular, because the data is a snapshot instead of mean values over a longer time series. At the surface, the model data seems to underestimate the salinity. Overall, the main pattern of density and salinity is considered as roughly the same, which is also concluded from other investigated sections (not shown).

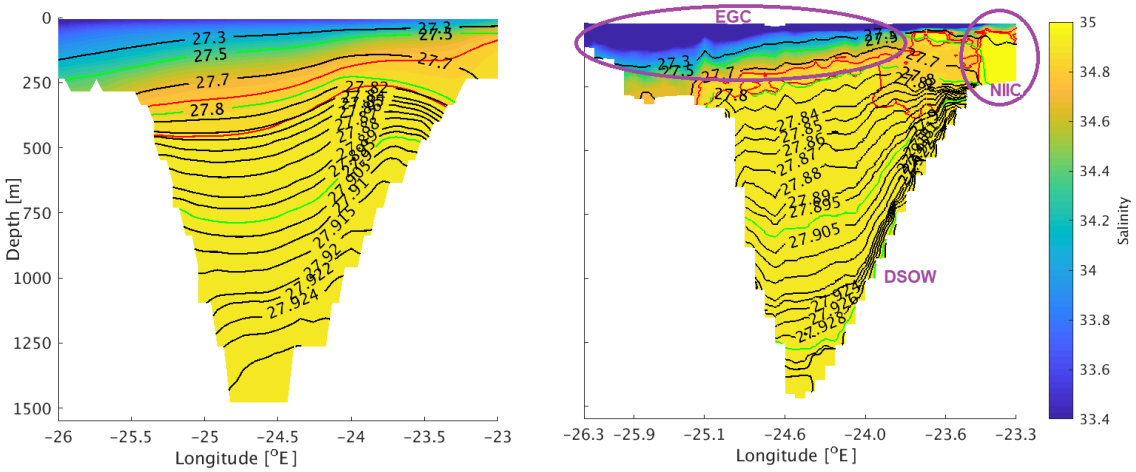

(a) Model data, mean values calculated between 02-01-2005 and 28-09-2016.

(b) Measurements with CTD data in 2012.

Figure 2.6: Sections of model data and CTD data. Salinity is shown in colour, related to the colour bar. The red lines correspond to values of salinity equal to 34.8 (above) and 34.9 (below). Potential density is shown with the black lines. Green lines show values of σ_0 equal to 27.5 kg/m^3, 27.8 kg/m^3, 27.9 kg/m^3 and 27.93 kg/m^3. Highlighted areas correspond with recognizable characteristics of the EGC and the NIJ. Water with a potential density above 27.8 kg/m^3 is considered as the DSOW.

2.4.2 Model data versus RAFOS floats

Particles are released in the model velocity fields by using a particle tracking simulator, as will be explained in section 3.1. A combination of launched particles and forward integration result in trajectories, in this section called "trajectories from model data". The trajectories from model data are compared to the tracks from RAFOS floats, as shown in Figure 2.7. Examples of a few trajectories of RAFOS floats are shown in red. These RAFOS floats are all launched on July 2014, with a 320 day mission. Examples of trajectories from model data are shown in Figure 2.7 by blue lines. The examples shown are launched at 01-07-2014 at the closest coordinates of the particle of the RAFOS released float at 70°N, at a depth of 550 meters. The trajectories are plotted for 320 days, to compare the length with the RAFOS floats. Only locations of the trajectories are shown in a 2D map, which means the differences in depth along the trajectories are not shown in this graph.

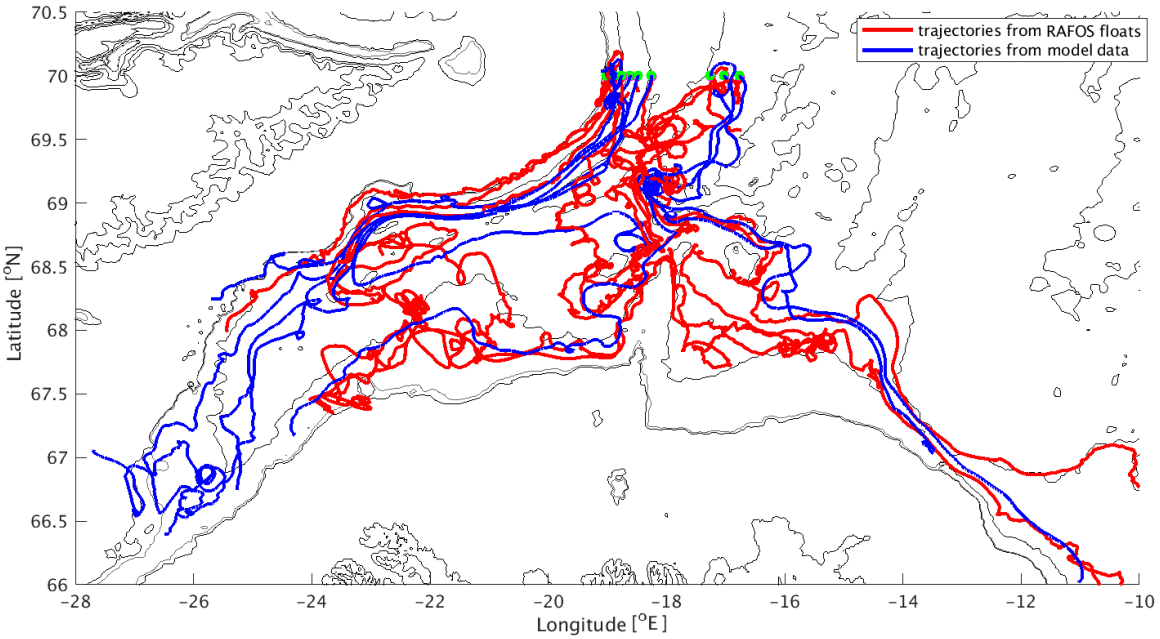

Figure 2.7: Map with several trajectories from RAFOS floats (red lines), compared with virtual particle trajectories of the model data (blue lines). Both trajectories are plotted for 320 days. Green dots correspond to the launch positions.

The trajectories from model data results and RAFOS floats are considered to be roughly similar on a large scale. Directions of both observational and model sources are comparable; all trajectories go along the EGC or go in a south-easterly direction, following EIC. Some of the trajectories go outside of the research area. On the other hand, most of the shown trajectories ended within the same area (DS and BB). The length of the trajectories after 320 days is roughly the same for the trajectories of the model data and RAFOS floats. None of the trajectories passed the sill during this time. The mean velocity of the particles over a this period is roughly comparable. However, additional differences are seen, for example the model data is more smooth, while the RAFOS floats have more small scale features, as described by De Jong et al. [2018]. One possibility for this difference is the resolution of the model; since the grid size of the model is around 4 kilometers, it is too coarse to resolve the smaller scale features as visible at the trajectories of the RAFOS floats.

3. Method

In this chapter, the method is explained. First, virtual particles are released using a particle tracking simulator, as described in section 3.1. Using the potential vorticity, explained in section 3.2, several eddy parametrization methods can be applied. The method for detection of eddies in this project is described in section 3.3 and the differences between cyclonic and anticyclonic eddies are explained in section 3.4.

3.1 Particle tracking simulator

Particles are released offline using the fourth-order Runge–Kutta method on a three-dimensional Arakawa C-grid with OceanParcels ("Probably A Really Computationally Efficient Lagrangian Simulator"), version 2.0.0b2 [Delandmeter and van Sebille, 2019]. Only advection is taken into account, since diffusion is not available yet for a 3D field.

To consider the most optimal integration step, short tests are done by releasing eight particles at different locations near the surface. The locations have high current velocity and mesoscale variability. Errors are expected to be larger at higher velocities and sharper angles. An example of a particle trajectory is shown in Figure 3.1(a). This particle is released at 12°E, since the water flows fastest near the surface in this area. The trajectories are shown by several colours, which indicate the resolution of time step. Since the model fields contain time steps of three days, the calculations are interpolated linearly. The red colour shows the trajectory when the locations of the particle is calculated for every 24 hours and the dark blue colours indicating smaller time steps. Figure 3.1(b) is a zoom in, related to the black box in Figure 3.1(a). The appropriate time interval is chosen to be one hour, because it is the optimum between computational time and errors related to the scale which is going to be observed. At a smaller resolution, the results converge at the resolution of one hour at the current scale. Figure 3.1(b) shows the trajectory of one hour in red and other trajectories in black.

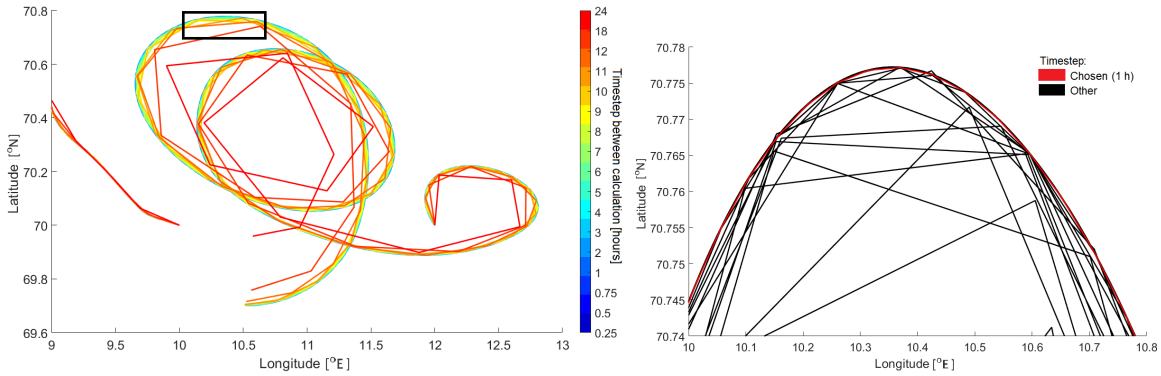

(a) Different resolutions as shown by colours

(b) A closer look of the final result (red) and other results (black)

Figure 3.1: Examples of trajectories of one virtual released particle using different time resolutions.

Besides an integration step, an integration length needed to be chosen. Considering Figure 2.7 again, 320 days seems an appropriate time for particles to travel from the release-locations into the Denmark Strait by a direct way. However, not all particles would flow into the DS directly, some particles are more rotating on their way compared to other particles. To sum up, a subset of a time resolution of one hour in combination with a simulation time of 400 days is chosen for this project.

With the settings described before, two batches of particles are launched. Particles are released on the first day of a each month and linearly interpolated by OceanParcels.

The first batch is released in the EGC, hereafter named as B-EGC. 100 particles are released at a depth of 550 meters and 100 particles are released at 650 meters depth. The locations of these particles are at 70°N and between 19.28°W and 16°W. Particles are released each month, between February 2005 and August 2015. They are released forward in time, to investigate which way particles will flow and whether they reach the DS. The expectation was that those particles released in deep water will flow southward. This test was used to answer the question on how many particles would reach the DS from the EGC with a certain trajectory.

The second batch is released in the DS, hereafter named as B-DS. To separate the surface water from denser water with $\sigma_0 < 27.8$, particles are released at two different depths above the sill (approximately 600 meter). 70 particles are released at a depth of 425 meters. Locations of these particles are between 66.3°N, 27.3°W and 66.12°N, 26.75°W. An additional set of 30 particles is released at 525 meters depth, between 66.18°N, 26.95°W and 66.15°N, 26.85°W. Particles are released again each month, between March 2006 and September 2016. The B-DS is released backward in time, to investigate which path particles have flown before the DS and whether all particles originate from the EGC. Since they are traced backward in time, the expectation was that some of these particles from the deeper area above the sill in the DS will originate from the EGC.

The main differences between both batches are summarized in Table 3.1.

Table 3.1: Primary differences between releases of virtual particles within the model data of the two batches, both run for 400 days. Particles are released every month for 127 months.

	B-EGC	**B-DS**
Integration in time	Forward	Backward
Date of first release	01-02-2005	01-03-2006
Released at latitude	70°N	$\sim$ 66.2 °N
Upper release depth	550 meters, 100 particles	425 meters, 70 particles
Lower release depth line	650 meters, 100 particles	550 meters, 30 particles

3.2 Potential Vorticity

With the TEOS-10 GSW Oceanographic toolbox [McDougall and Barker, 2011], the conservative temperature and absolute salinity can be calculated from in-situ temperature, practical salinity, depth and latitude of a data point. Using the equation of state, the potential density anomaly is calculated from the conservative temperature and absolute salinity [McDougall and Barker, 2011]. The potential density anomaly with a reference pressure of 0 dbar is calculated by equation 3.1 [McDougall and Barker, 2011].

$$\sigma_0 = \rho(\theta, S, 0) - 1000 \ \frac{kg}{m^3} \tag{3.1}$$

$\rho(\theta, S, 0)$ is the original potential density $[kg/m^3]$, calculated by using the potential temperature and absolute salinity. Using scales as described in section 2.2, it can be concluded that rotation and stratification are important. By considering both effects, the equation for potential vorticity can be written as equation 3.2.

$$q = \frac{f + \frac{\partial v}{\partial x} - \frac{\partial u}{\partial y}}{\rho_*} \frac{\partial \rho}{\partial z} = \frac{f + \zeta}{\rho_*} \frac{\partial \rho}{\partial z} \tag{3.2}$$

Where q is the potential vorticity $[1/(ms)]$ and ζ is the vertical component of vorticity, the relative vorticity $[1/s]$. ρ_* is the reference potential density $[kg/m^3]$.

The static stability is investigated by using the Brunt-Väisälä frequency or buoyancy frequency, calculated by equation 3.3.

$$N^2 = -\frac{g}{\rho_*}\frac{\partial \rho}{\partial z} \tag{3.3}$$

In equation 3.3, N is the Brunt-Väisälä frequency $[1/s]$ and z is the depth [m]. ρ is the density $[kg/m^3]$. When $N^2 > 0$, this results in $\frac{\partial \sigma_\theta}{\partial z} < 0$, which means the higher densities are below the lower densities, which is considered a stable situation. In contrast, if $N^2 < 0$ and $\frac{\partial \sigma_\theta}{\partial z} > 0$, it means the higher densities are above and the water column is considered as statically unstable. If the relative vorticity can be neglected with respect to the planetary vorticity (so $f > \zeta$), then q reduces to equation 3.4.

$$q = \frac{f}{\rho_*}\frac{\partial \rho}{\partial z} = -f\frac{N^2}{g} \tag{3.4}$$

Using the concept of potential vorticity conservation, several eddy parametrization methods can be applied.

3.3 Eddy detection

As already shown in Figure 2.2, some eddies are probably visible between 16°W and 18°W, and between 68°N and 69.5°N. Using the output velocities of the model, an eddy detection method is applied on an Eulerian approach. The Eulerian approach means that eddies are detected by using fixed locations of measurements. The opposite is the Lagrangian approach, where eddy-like behaviour can be traced in a trajectory, for example used for the RAFOS floats by De Jong et al. [2018]. The method of tracking eddies by the Eulerian approach used in this project is described by Nencioli et al. [2010] and applied to detect eddies in 2D fields at a time step, based on the geometry of the flow field. Eddies are defined as a region in which the velocity field exhibits a rotary flow, which means that the velocity vectors rotate clockwise or counter-clockwise around a center. Eddy boundaries (hereafter called "edges") are in this case defined from contour lines of the streamfunction field, as the outermost closed streamline from the eddy center across which the velocity still increases outward of the eddy center. Four constrains have to be satisfied to define an eddy, as described by Nencioli et al. [2010]:

- Along an east–west (EW) section, y has to reverse in sign across the eddy center and its magnitude has to increase away from it. Two examples are shown in Figure 3.2 by the green vectors.
- Along a north–south (NS) section, u has to reverse in sign across the eddy center and its magnitude has to increase away from it: the sense of rotation has to be the same as for y. Two examples are shown in Figure 3.2 by the magenta vectors.
- The velocity magnitude has a local minimum at the eddy center. Two examples are shown in Figure 3.2 by the red vectors.
- Around the eddy center, the directions of the velocity vectors have to change with a constant sense of rotation and the directions of two neighbouring velocity vectors have to lay within the same or two adjacent quadrants. Two examples are shown in Figure 3.2 by the orange vectors.

If all four constraints are satisfied, shapes of eddies are calculated. The output of this method gives various properties of eddies like the coordinates of the edge, as shown by the black lines in Figure 3.2, the coordinates of the centers, radius, type (anti- or cyclonic) and the trajectories over time.

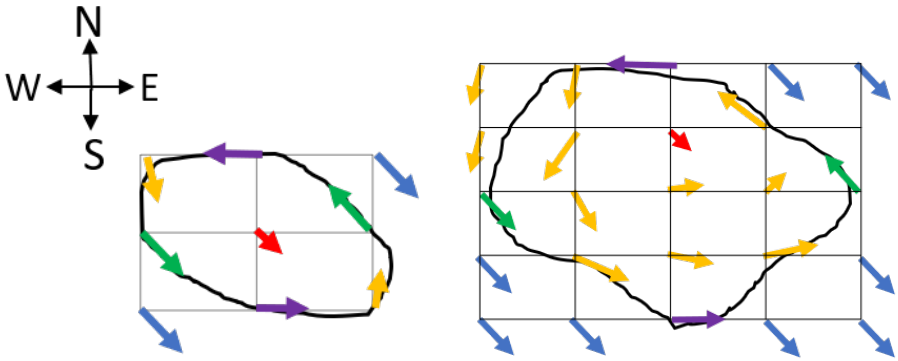

(a) n=2 *(b) n=4*

Figure 3.2: Examples of eddies tracked in a grid used in the method of Nencioli et al. [2010]. Vectors are related to four different constraints, which had to be satisfied. n gives the minimum amount of gridpoints between purple vectors, as well as the green vectors.

To apply this method for several grids, several parameters can be chosen. One parameter is available for the number of grid points for u and v velocity reversal, (hereafter named as parameter n) and another parameter related to the area to detect a velocity minimum. The last parameters are for the initial area to compute the eddy dimensions and the distance between two eddies, to derive eddy tracks. For example, Nencioli et al. [2010] used a grid of approximately 1 by 1 km, and choose $n = 4$, as shown in Figure 3.2(b), where the purple vectors are 4 gridpoints away from each other, as well as the green vectors. The grid of the model data used in this project is approximately 4 by 4 km and the Rossby radius is ± 10 km. This means the expected eddies are smaller compared to the example used in Nencioli et al. [2010]. The option of $n = 2$ is taken into account as well, as shown in Figure 3.2(a).

To focus on more details north of the DS, the study area for this project is chosen to be between 66°N and 72°N, and between 12°W and 30°W. Two plots are made with the amount of eddy centers detected over the entire available time series with different parameters for n, as visible in Figures 3.3 and 3.4. Both are taken at a depth of 547 meters, which is one layer of the model data. Hydrographic properties related to the DSOW are found in this layer.

As visible in Figure 3.4, at some places no eddies are found for $n = 2$. However, no eddies are found at a larger area when using $n = 4$, as visible in Figure 3.3. For example, within the orange box, almost no eddies are found over the entire time series for $n = 4$ in contrast to the results of $n = 2$. Additionally, the total amount of eddy centers found within the plotted area is 7754 for $n = 4$ and 48247 for $n = 2$. This is a mean of 1.8 and 11.3 eddies per day, respectively. Overall, comparing results with Figure 2.2, velocity and density fields does show evidence of eddies. Highlighted areas in orange and red are investigated further in this project.

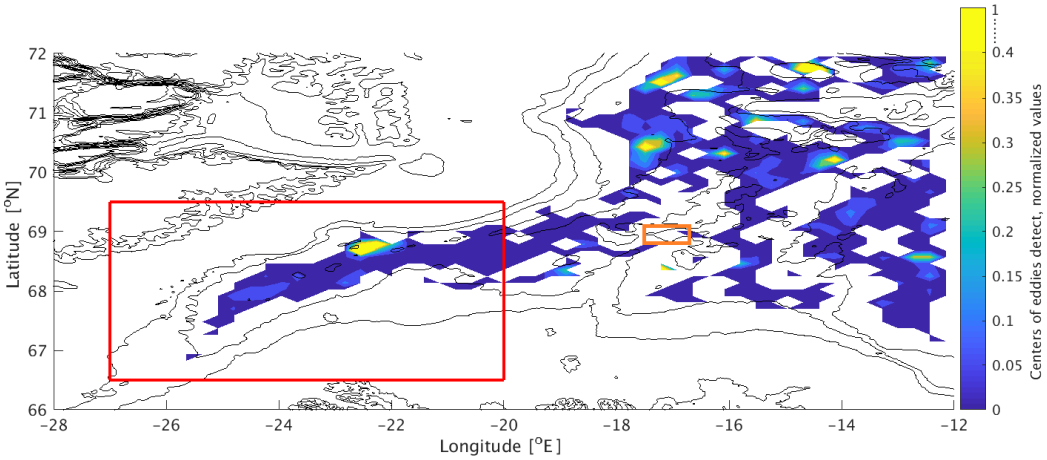

Figure 3.3: Density of eddy centers found by eddy tracking software at 547 meters depth between 02-01-2005 and 28-09-2016. Four grid points are detected for v and u velocity reversal (n=4). Note: Values are normalized by dividing each value by 218, which is the maximum amount of eddies detected at a location, related to the (non-linear) colour bar. Highlighted areas are investigated in this project.

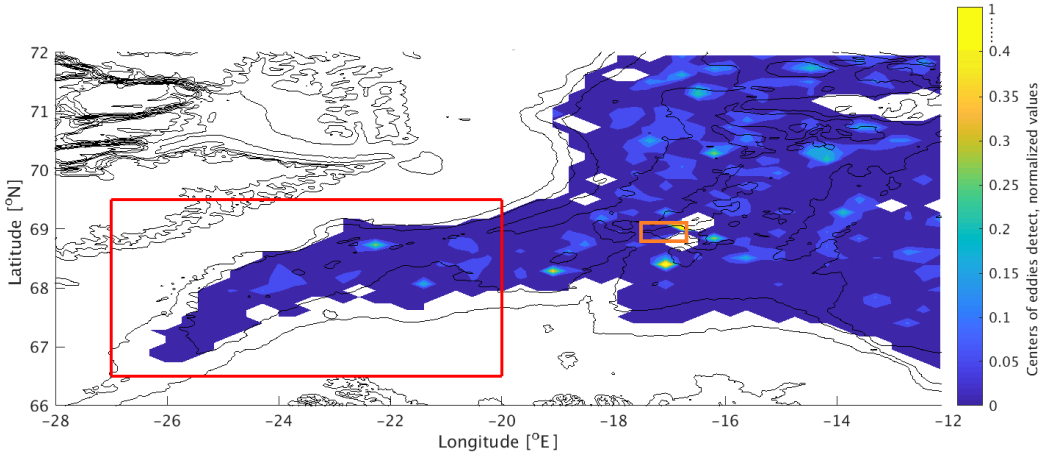

Figure 3.4: Similar to Figure 3.3, but two grid points are detected for v and u velocity reversal (n=2). Note: Values are normalized by dividing each value by 1139.

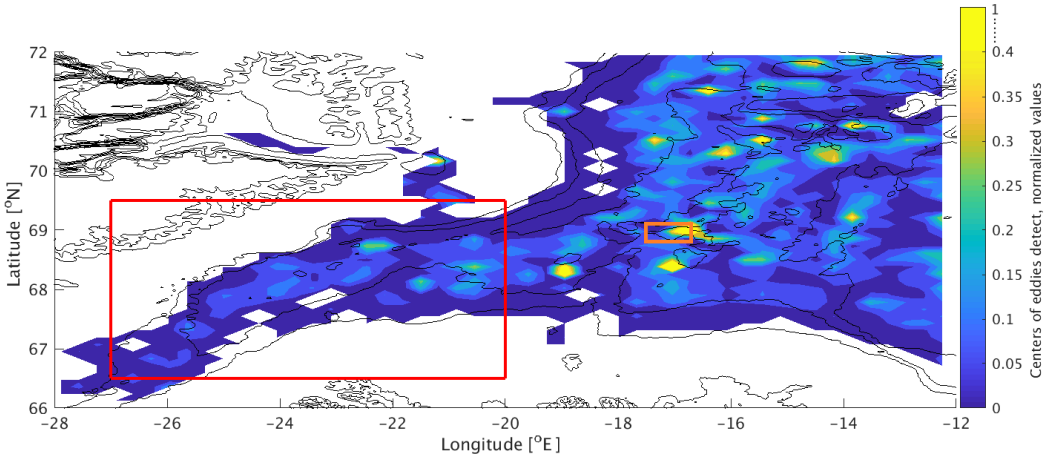

Figure 3.5: Similar to Figure 3.3, but two grid points are detected for v and u velocity reversal (n=2) at a depth of 337 meters. Note: Values are normalized by dividing each value by 661.

Additionally, Nencioli et al. [2010] considered ideal parameters settings to be $n = 4$, determined for the area of Southern California Bight from the results of a 1-km-resolution numerical experiment using the Regional Ocean Modelling System. Although the resolution is smaller compared to the data in this project, the parameter is set larger, to prevent the noise of detecting meanders as eddies. Additionally, the Rossby radius of deformation is also larger in the area Nencioli et al. [2010] investigated, since they look into an area closer to the sea surface and equator. However, within the two investigated areas (red and orange boxes in Figure 3.4), no meanders were seen yet, so they are considered as negligible in the investigated area of this project. The parameter used in Figure 3.4 is chosen for this project, which is $n = 2$.

A layer at 337 meters depth is also investigated and compared with a layer at 547 meters depth. Results of eddy detection at the layer of 337 meters depth are shown in Figure 3.5. A total amount of 60693 eddies are detected, which is an overall mean of 14 eddies per day. Compared to the results found at 547 meters, more eddies are found. This is visible by comparing the covered area by colours in plots for both layers. This is probably due to the topography, because the area at 337 meters is bigger compared to the area at 547 meters. Since values are both normalized and plotted with the same colour bar, patterns of eddies can be compared. Locations where more eddies are found over time in Figure 3.4 are at roughly the same locations where relatively a large amount of eddies are found in 3.5. Areas where a lot of eddies are found (yellow) do overlap roughly in both layers, at 337 and 547 meters depth. Since eddies are found at roughly the same places, this means that the eddy is present over a larger depth. To conclude, 547 meters seems representative for deep flow waters, separated from purely surface eddies.

3.4 Cyclonic and Anticyclonic eddies

The eddy detection method, as described in section 3.3, assumes maximum radial velocities at the edge of an eddy, which is the definition of a Rankine vortex [Lilly and Rhines, 2002], as described by equation 3.5.

$$v(r) = \begin{cases} \frac{Vr}{R} & \text{for} \quad r < R \\ \frac{VR}{r} & \text{for} \quad r > R \end{cases} \tag{3.5}$$

Where v(r) describes the radial velocity profile of this (azimuthally symmetric) eddy $[m/s]$, which is positive for cyclonic currents [Lilly and Rhines, 2002]. V gives the maximum azimuthal velocity $[m/s]$. R is the distance between the center of the eddy to the edge [m] and r describes the distance to the eddy center $[m]$. This description of a very simple model eddy consists of solid-body rotation within a core (r , R) and 1/r decay elsewhere [Lilly and Rhines, 2002]. This is visualized by the grey line in Figure 3.6, where the velocity is measured perpendicular to the advecting flow, also called swirl velocity.

If the flow is in quasi-geostrophic balance, the Rankine vortex is the solution to a uniform potential vorticity anomaly within radius R of magnitude $q = 2V/R$ [Lilly and Rhines, 2002]. Besides the direction of the velocity, Assassi et al. [2016] found that cyclonic and anti-cyclonic eddies can be recognized by the shapes of the isopycnals, which can be seen in transects of the PV-anomaly, as sketched in Figure 3.7.

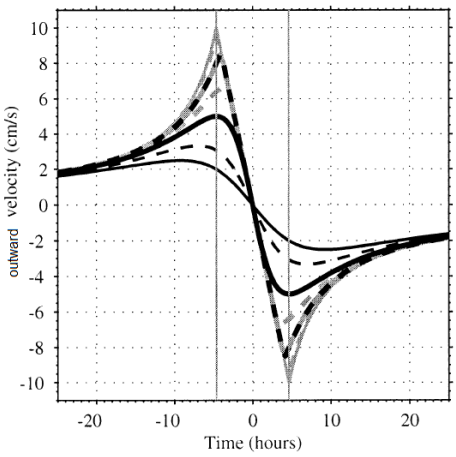

Figure 3.6: The perpendicular velocity component of an advected cyclonic model eddy, which has a maximum speed at the eddy rim (gray line) of 10 cm/s. At several locations slices are made through the eddy, as shown by the different lines. The grey line shows an example of a "Rankine vortex". Adopted from Lilly and Rhines [2002].

As explained in section 3.3, a layer at a depth of 547 meters is investigated in more detail. It is assumed in the area of the DS that the core of the eddy is above a depth of 547 meters, since the sill has a depth of approximately 600 meters. With this assumption, the deeper parts are investigated in more detail. In Figure 3.7, it is visible that at deeper parts of the subsurface layers, isopycnals are displaced compared to a situation without any eddy. The density at an anticyclonic eddy is less than normal, as visible in Figure 3.7(a). However, the density in a cyclonic eddy is increased, as visible in Figure 3.7(b). Also visible is the encapsulated fluid, as highlighted in blue in 3.7(a). However, Assassi et al. [2016] show that in a more complex environment, errors can be expected, in particular when strong currents exist in the vicinity of the vortex.

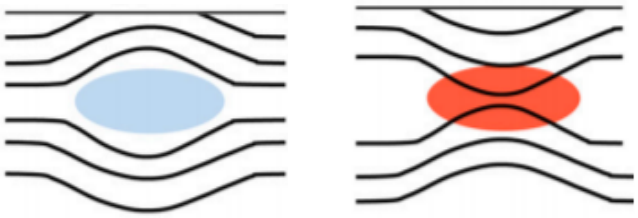

(a) Anticyclonic case *(b) Cyclonic case*

Figure 3.7: Isopycnal displacement (black lines), for two different types of eddies (cores are highlighed by colours). The y-axis shows a relative depth. Adopted from Assassi et al. [2016].

4. Results

In this chapter, results of this study are described. After releasing the particles, an overview of the results is given in section 4.1. The variability of the trajectories are investigated as well as the related properties, described in sections 4.2 and 4.3. Furthermore, mesoscale eddies are analysed using the model data, presented in section 4.4.

4.1 Overview of trajectories

Two overviews of pathways of the released particles are shown in Figure 4.1 and Figure 4.3 for both the B-EGC and B-DS batches, respectively. Colours in the plots show the amount of particle trajectories that passed a respective grid box. A grid box has a resolution of roughly 8 by 8 km. Hence, for all trajectories in a batch, the total amount of trajectories which passed the grid box are counted. When a particle flows through a grid box twice, it is still counted as one trajectory. These values are normalized, as explained in appendix A.1.1. To see several pathways, the colour bar is plotted non-linear, where above a value of 0.5 is considered as a "saturated" grid box for the B-EGC in this case.

In Figure 4.1, it is recognizable that particles are going through the EGC (south of the remarked number 1) to the Denmark Strait. Additionally, some particles flow to the east. After this turn, particles will go through the west (south-west of 2) or east side of the KR. Particles going to the east side of the KR appear to go through either the NIJ (north of 3) or the sEGC (north of 4), or both. Another possibility is that some particles from the EGC will pass through the sEGC as well. Additionally, since particles are released at 550 meters and 650 meters, both situations separately are investigated (not shown). Nevertheless, results show roughly the same pattern after normalization.

In Figure 4.2, the mean amount of days is visible when particles reach a respective grid box. This mean value is calculated for all trajectories of the B-EGC, where the first day is related to the day after the release date of a particle. In Figure 4.2, it is clearly visible that particles which are going through the EGC to the DS are much faster compared to the particles which moved through the NIJ to the sill.

An overview of the density distribution of the B-DS is given in Figure 4.3. A backward integration has been used for this batch, where the last computed location of a particle is defined as the starting point in time in this text. Again, these values are normalized, as explained in appendix A.1.1. At the B-DS, a value of 0.25 is considered as "saturated", which means that most of the particles pass the reddish areas (south of the remark number 1). Over time, particles separate into several pathways (south of 2). Some particles originate from the EGC (4), but the main group of particles seems to originate from the east, where some particles will originate from the NIJ (north of 3). Finally, some particles even come from the northern or southern part next to the KR (around 5) within the time frame of the experiment.

Additionally, an overview of the distribution of mean days before particles are passing a grid box of the B-DS is given in Figure 4.4. This figure stresses the fast travel time from the EGC and KR to the DS (yellow). The travel time of particles which passed out of these areas is longer (blue).

To conclude, from the investigation of the resulting trajectories of both batches, the EGC is recognizable, however no clear main route of the DSOW to the sill is visible. Although it seems that the EGC is the fastest connection to the sill, a connection with the sEGC or the NIJ is not excluded.

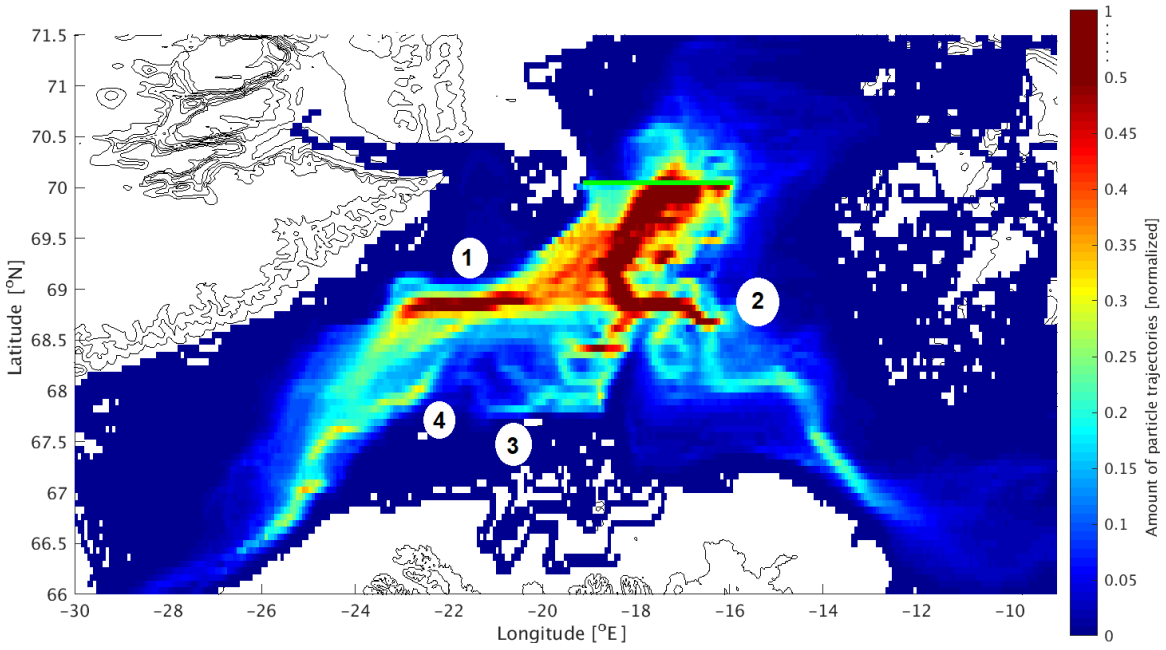

Figure 4.1: Overview of density distribution of all trajectories of the B-EGC launched between 02-2005 and 08-2015 at the green line in a forward time integration. See text for explanation of the numbers. Note: The colour bar is non-linear to make the different pathways more clear.

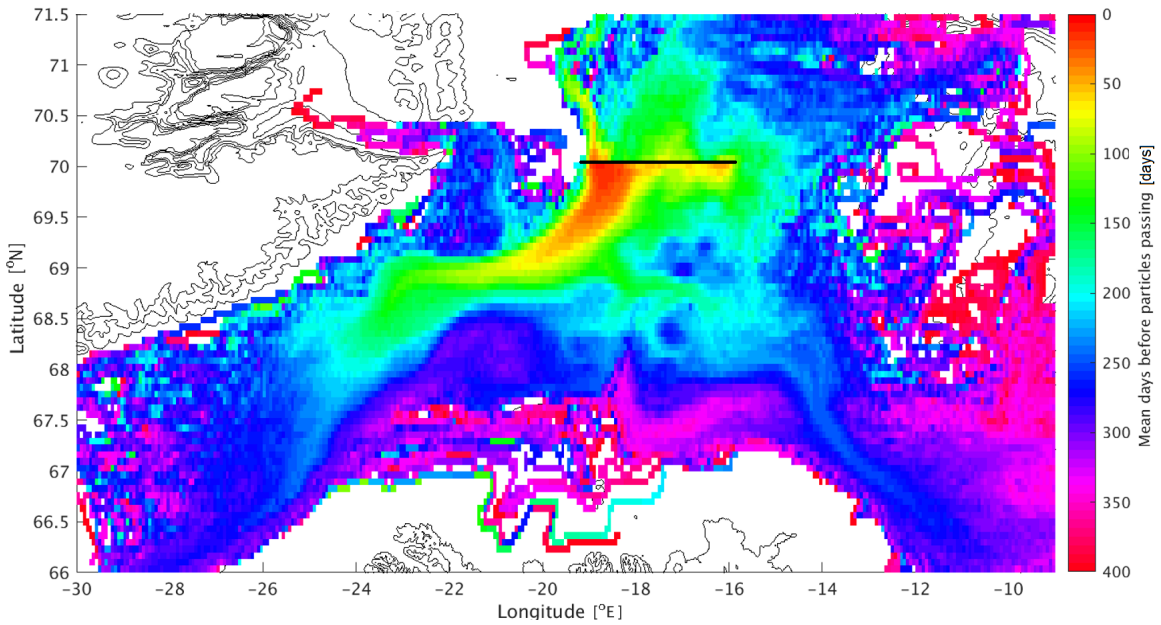

Figure 4.2: Overview of mean days before particles of the B-EGC pass a respective grid box. The release locations are shown by the black line.

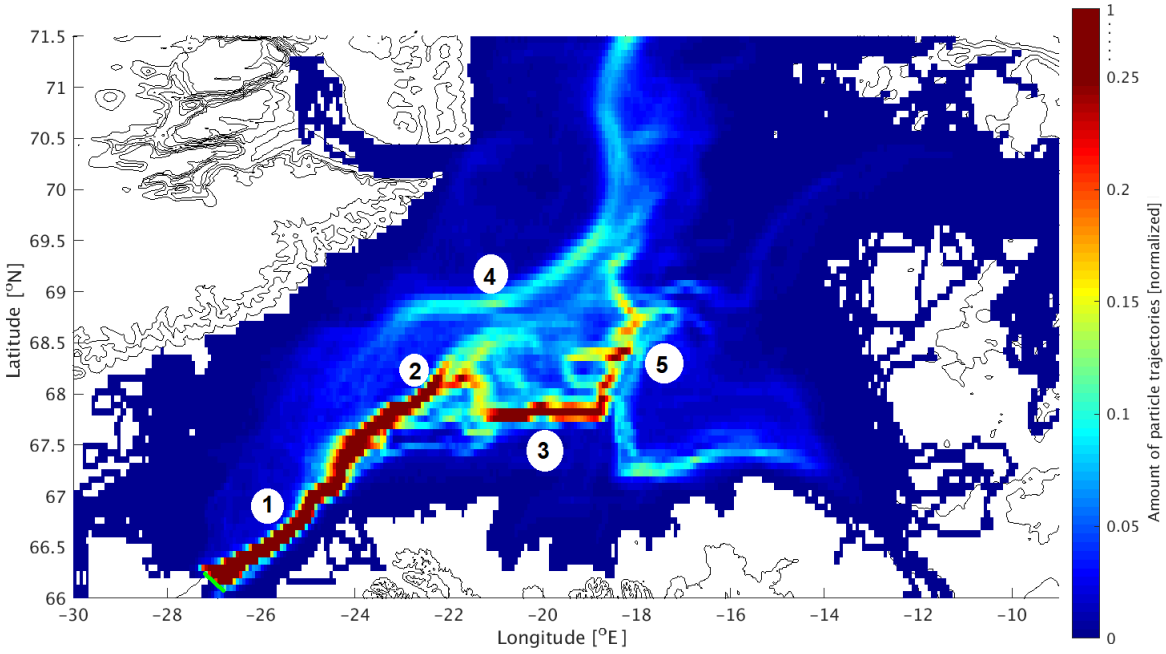

Figure 4.3: Overview of density distribution of all trajectories of the B-DS launched between 03-2006 and 09-2016 at the green line in a backward time integration. See text for explanation of the numbers. Note: The colour bar is non-linear to make the different pathways more clear.

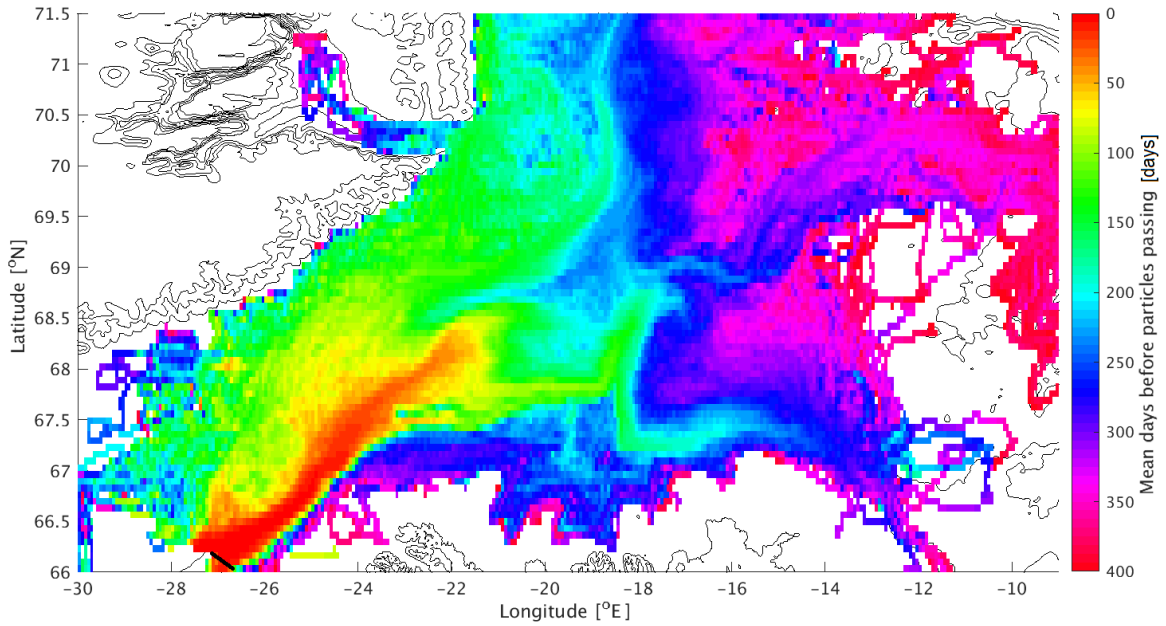

Figure 4.4: Overview of mean days before particles of the B-DS pass a respective grid box. The release locations are shown by the black line.

4.2 Variability of trajectories

In Figure 4.5 and Figure 4.6, examples are shown that depict particle trajectories, released in certain months as described in the figures. If a particle has not been moving for at least 24 hours, it is still traced but defined as stuck. This is probably due to shallow bathymetry, because it is recognizable at the edges of the model data, marked with (very small) black dots.

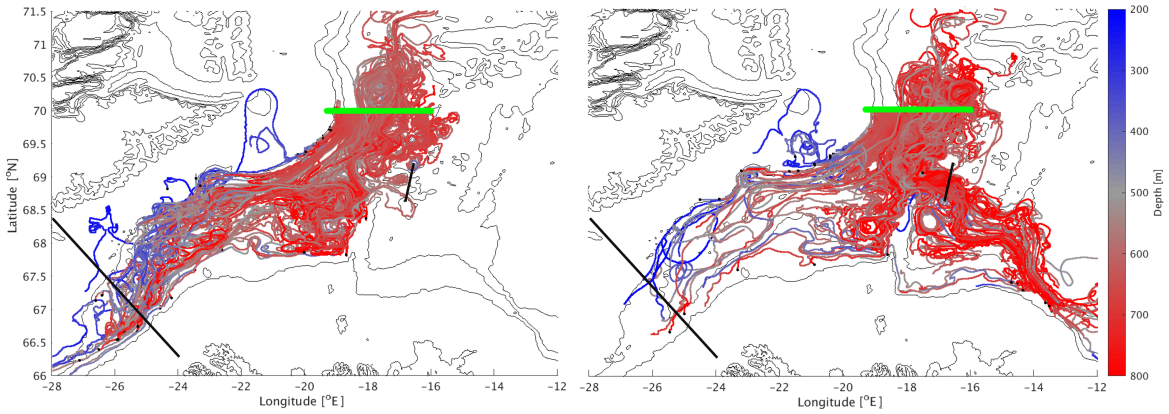

(a) Launch date: 01-01-2012 *(b) Launch date: 01-11-2014*

Figure 4.5: Particle trajectories of the B-EGC from a certain release date. Green dots correspond to the release coordinates of the particles. Small black dots correspond to a location where particles are "stuck" (see text). Colours indicating the depth of the particles along the track. Particles are counted over black transects. Note: the latitude y-axis and colour bar can be applied for both Figure (a) and Figure (b).

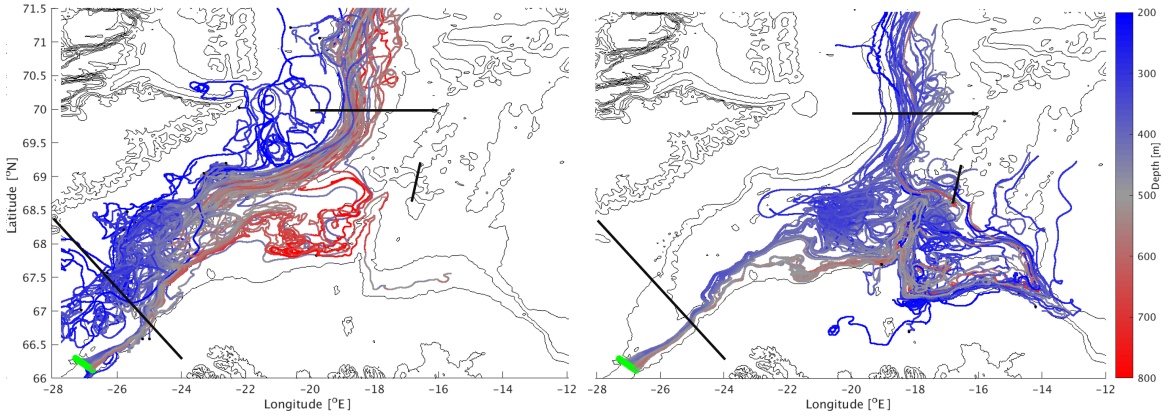

(a) Launch date: 01-03-2010 *(b) Launch date: 01-09-2014*

Figure 4.6: Similar to Figure 4.5. In this case results are part of the B-DS.

Particles in Figure 4.5(a) are released at 01-01-2012, as part of the the B-EGC. Particles mainly turned to the west into the DS. In addition to this, at a lower depth they turned more southward, which might be related to the NIJ. In contrast, visible in Figure 4.5(b), particles were released at 01-11-2014 and widely spread, which means more particles went to the east, compared to the situation shown at 4.5(a). Near the DS (left corner), particles moved upward (blue-ish parts of the trajectories). When particles turn to the eastern side (right corner), it seems like particles turned more downward (reddish colours). More examples are shown in appendix B.

Particles which travel trough several sections (black lines) are counted. 25400 particles are released as part of the B-EGC, between 70°N and between 19.28°W and 16°W (green line). 22297 particles are passing the horizontal line at 69.5°N, which is approximately 88 percent of the total released particles of the B-EGC. Other particles are probably stuck in the topography or moved northward of the release location. 5382 and 4066 particles passed the transects (black) in the DS and SFZ, which is 24 and 18 percent of the total particles released, respectively.

In Figure 4.6(a) and Figure 4.6(b), particles are shown which are released at the B-DS at 01-03-2010 and 01-09-2014, respectively. In Figure 4.6(a), more particles are coming from the west from the EGC. Again, the last computed location of a particle is defined as the starting point in time in this text, since a backward integration in time is used. Mainly particles which are relatively less deep (blue) are crossing the sill of the DS. This is a contrast to the particles shown in 4.6(b). In 4.6(b), particles are mainly coming from the east, probably related to the NIJ. Further back in time, they are coming from either the northern side (EGC) or more eastward next to the KR. Another interesting feature are the particles which seem to turn around at 67.5°, 14°W, where they probably originate from the EIC. Except for the first few days where deeper particles move upwards (red dots near the green line), the depth of a trajectory seems roughly constant.

As done for the B-EGC, particles which travel trough the sections in the EGC, DS and SFZ are counted. 12700 particles were released as part of the B-DS. 11989 particles came from the northern direction, through the section in the DS, which is almost 95 percent. However, 1073 particles went through the section at the SFZ, which is 8 percent. 5663 particles passed through the release location of the B-EGC, which is almost 45 percent of the particles released during the B-DS.

To conclude, during the monthly releases from both batches, the trajectories show a clear variability in pathways. The fluctuation appears to occur strongly on a monthly time scale rather than of inter-annually. According to this, it is thought that small scale processes are probably more important than assumed previously. Consequently, eddies are further investigated in this research, described in section 4.4. Additionally, some particles from the EIC seem to return near the Iceland shelf and flow into the westward direction, to the KR.

4.3 Mean hydrographic properties

The resulting hydrographic properties of trajectories of both batches the B-EGC and the B-DS are compared with the mean values of the model data in the following sections. Mean values of the model data are calculated between 02-01-2005 and 28-09-2016, over horizontal layers between 399 and 635 meters depth. These depths span the depth where particles are released which are at 425 and 547 meters for the B-DS and at 550 and 650 meters for the B-EGC. Results of the mean depth of the trajectories are given in section 4.3.1.

Figure 2.2 shows mean values of velocity from the model data at 547 meters. The EGC and NIJ are recognizable by their higher velocity, compared to the surroundings. Also, an area exists with higher velocities east of the KR, around 67°N, 13°W. The direction seems to be from the EIC to the Iceland shelf. Within the SFZ, anticyclonic and cyclonic eddy behaviour is visible at the south and north side. At the Iceland Sea gyre, cyclonic eddy behaviour is recognizable as well. The mean velocity between 399 and 635 meters (not shown) results in a similar pattern as mean velocities at 547 meters.

Values of salinity and temperature are calculated using the coordinates at each time step of the particles from both batches, as a result of using OceanParcels. Subsequently, a linear interpolation is applied to obtain values of salinity and temperature from the model

data. It has to be taken into account that the particle tracking simulation does not include diffusion, so density can change along the route of a particle, almost independent of the ascent or descent of a particle. This is further discussed in section 5.3. Overall, results of the trajectories show a colder, more saline and denser result than the model data. One suggestion for this is that particles are not confined between 399 and 625 meters (correlated to the calculated mean values of the layers of the model data), because some particles travel deeper and they are taken into account as well. Results of the mean potential temperature, mean salinity and mean potential density are given in sections 4.3.2, 4.3.3 and 4.3.4, respectively.

4.3.1 Depth of trajectories

To separate the dense overflow water from the surface water, only trajectories are taken into account which remain below a depth of 425 meter. In Figure 4.7, the mean depth of the particles in a grid box is shown, taking only the results from the B-EGC into account. At the B-EGC, particles are released every month for 127 months starting at 01-02-2005. Locations where particles usually travel upward (blue) or downward (red) are recognizable. In some cases, particles travel deeper compared to their release location. Locations of some currents are recognizable, like the sEGC around 68°N, 23°W, where particles go deeper. To a lesser extent, this is also the case north of the sEGC, at the shEGC. Particles also travel downward around the KR at 68°N, 18°W and slightly before the sill. The mean depth of particles west of the KR, near the Iceland shelf, seems to have a sharp transition, probably due to the topography. Particles went upward near the Iceland shelf, and slightly northward they clearly moved deeper. Particles from the EIC probably turn around at 67°N, 14°W, where particles are relatively deep on average. Fewer particles went to the eastern side of the map, to the Iceland Sea gyre. Particles which reach this area generally seem to travel upward in this area.

In Figure 4.8, the mean depth of particles in a grid box is shown, as part of the results of the B-DS. Again, the last computed location of a particle is defined as the starting point in time in this text, since a backward integration in time is used. At the B-DS, particles are released every month for 127 months starting at 01-03-2006. Locations are visible where particles usually are more travelling to upward (blue) or downward (red), using the same colour bar as in Figure 4.7. Note that these particles are released at shallower depths. Therefore, it seems that particles travelled more upward during the B-DS compared to the B-EGC. In the area around 69°N, 18°W, depths are varying more compared to the results of the B-EGC. This is probably because the particles of the B-EGC are launched very close to 69°N, 18°W, compared to the particles of the B-DS.

A few particles seem to flow from the Iceland Sea gyre into the DS within 400 days. These particles possibly came from the NwAC. Areas were particles went deeper (red) are mainly visible near the KR, which means that particles came from greater depths before they flow over the sill. Near the sill, particles went to a relatively shallower depth. No sharp transition in depths is visible near the sill within the results of the B-DS, in contrast to the mean depths as a result of the B-EGC. This is probably because the release locations of the B-DS were higher and closer to the sill. The pathway through the DS is clearly visible, since almost all particles seem to come from one direction in the north. Some particles seem to be somewhat circling near 425 meters west of the sill. At the south-eastern part of the map, it is clearly visible that no particle remaining below a depth of 425 meters has reached the area around 67°N, 11°W. This is in contrast to the results of the B-EGC, probably due to a combination of the release locations, the directions of the currents, and the length of the simulation (400 days).

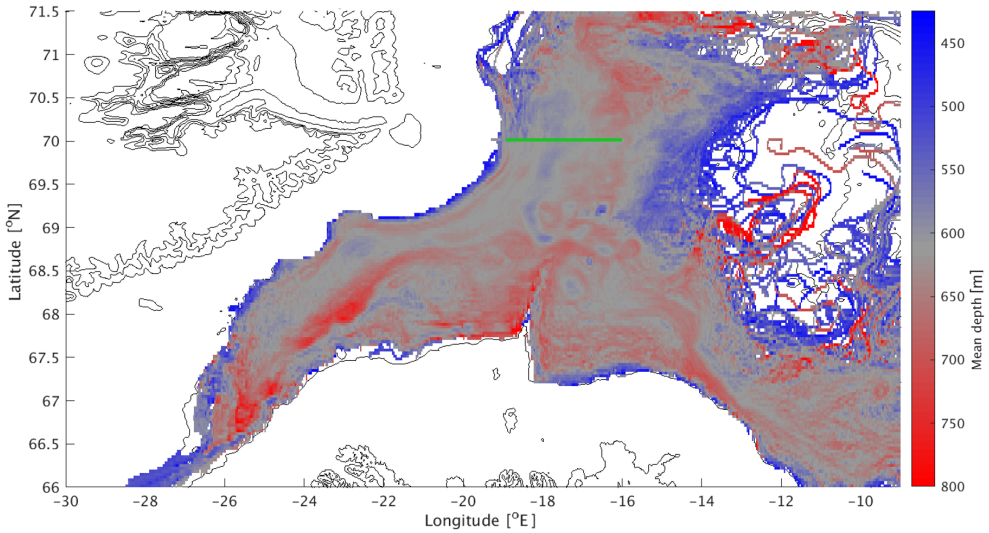

Figure 4.7: Mean depth of trajectories remaining below a depth of 425 meters, as part of the B-EGC. Particles are released every month for 127 months starting at 01-02-2005. The green line shows the release location of the particles.

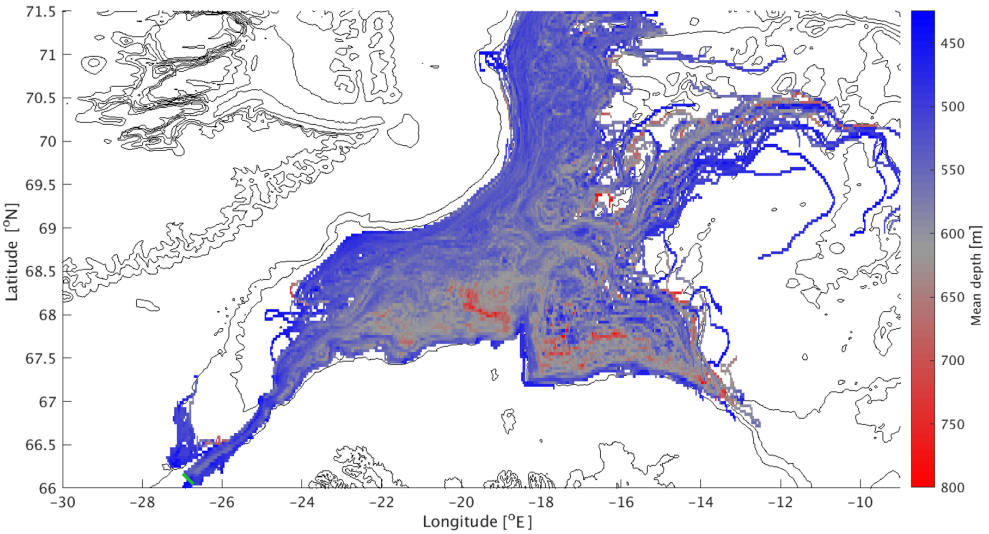

Figure 4.8: Similar to Figure 4.7. In this case, results are part of the B-DS. Particles are released every month for 127 months starting at 01-03-2006.

4.3.2 Temperature

The mean temperature is shown for the model data, the results of the B-EGC and B-DS in Figure 4.9, Figure 4.10 and Figure 4.11, respectively.

In the model data (Figure 4.9), warm water is found near the Greenland shelf. This can be related to the warmer rAW which flows southward through the EGC. Further south, near the sill, a sharp transition of cold water to warm water takes place. Further north, at the Iceland shelf, a rim of colder water is visible, which is probably related to the NIJ, where the coldest water is found east of the KR. Close to the shelf, a sharp transition takes place to warmer water. A colder core is visible at the Iceland Sea gyre. North of this core, warm water is found, which probably originates from the NwAC, because this water does not cross the pole.

Figure 4.10 shows results of the trajectories from the B-EGC. The overall temperatures are lower compared to the model data. Relatively high temperatures are found north of the release locations, around 70°N, 18.5°W. These are probably related to a time step where some particles went north and upward, as can be seen by the blueish colours in Figure 4.7. This pathway contrasts to the more common southward direction. However, both sides north and south of 70°N, 18.5°W show temperatures above 0.5°C, which can be recognized as the rAW mass. The AAW is probably more east of the rAW, for example around 70°N, 18°W, recognizable by the lower temperatures in this map. Unfortunately, too few particles made it to the center of the Iceland Sea gyre to get a clear overview of reliable temperatures. Like in the model data, colder water is found near the Iceland shelf due to the trajectories of the B-EGC. Although in the model data the west of the KR is clearly colder, results from the B-EGC show colder temperatures at both sides west and east of the KR.

In the map which shows results of the B-DS (Figure 4.11), a roughly similar pattern is found in the mean temperature compared to the model data and the results of the B-EGC. Although the pattern seems to be similar, the overall temperature found seems to be warmer than the B-EGC and still colder compared to the model data. The warmer line starting around 70°N, 18.5°W is visible again, however in this case, no sharp transition is visible. The rAW and AAW are less recognizable. The colder water near the KR is still visible, however in this case the coldest water is found at the east side of the KR again, similar to the model data. In a few trajectories north of the Iceland Sea gyre, water flowing directly from the NwAC is recognizable by the higher temperature, because the water mass which flows through the NwAC and splits to the Icelandic gyre probably did not cross the pole. Additionally, the sharp transition of cold water into warm water near the sill is recognizable in both results of the B-EGC and B-DS.

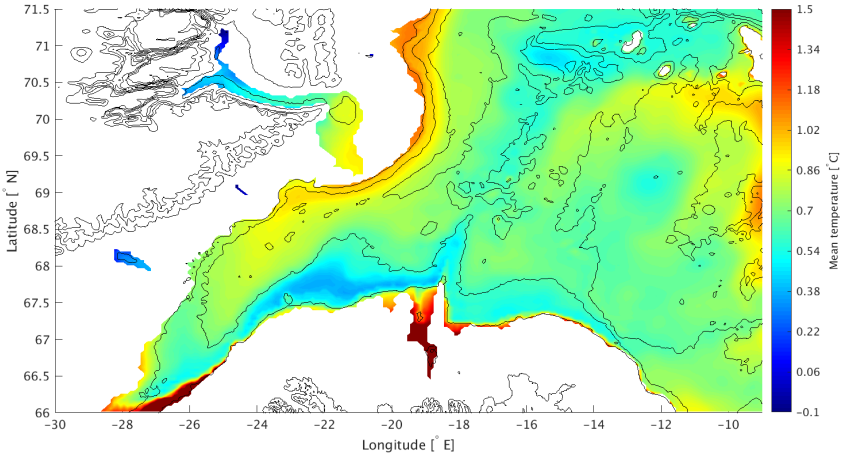

Figure 4.9: Map of the mean potential temperature between 02-01-2005 and 28-09-2016, at a depth between 399 and 635 meters from model data. Isobaths are drawn every 500 meters.

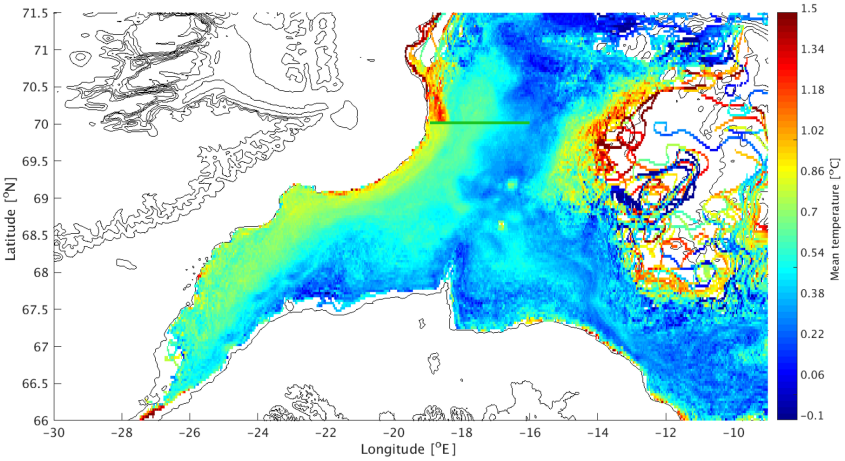

Figure 4.10: Mean temperature of trajectories remaining below a depth of 425 meters, as part of the B-EGC. The green line shows the release location of the particles.

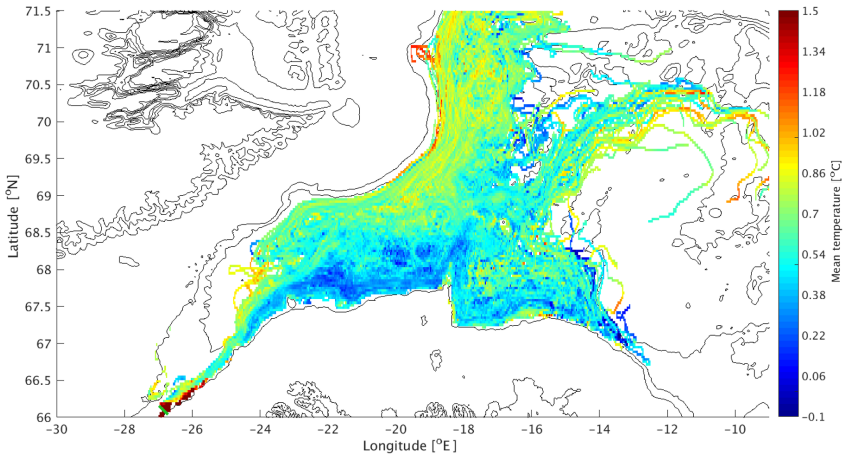

Figure 4.11: Mean temperature of trajectories remaining below a depth of 425 meters, as part of the B-DS. The green line shows the release location of the particles.

4.3.3 Salinity

The mean salinity is shown for the model data, the results of the B-EGC and B-DS in Figure 4.12, Figure 4.13 and Figure 4.14.

Saline water is found near the sill and the Iceland shelf, as visible in the map of the model data (Figure 4.12). North west of this saline water, a sharp transition to fresh water is visible. The EGC is recognizable due to its saline water, compared to the surroundings. Near the KR, fresh water is recognizable, as well as the core of the Iceland Sea gyre. Saline water is also found north of the Iceland Sea gyre, where particles probably came from the NwAC.

The map of mean salinity from results of trajectories of the B-EGC is visible in Figure 4.13. In contrast to the model data, three main pathways of the EGC are roughly recognizable by their saline water, compared to the surroundings. One pathway exists near the Greenland shelf, related to the EGC. A second pathway seems to pass the west of the KR and a third pathway follows the EIC, which seems to reach the shelf at the east of the KR. A sharp transition to fresh water is found near the sill, at the side of the Iceland shelf. The saline water found at the sill in the model data is not clearly recognizable from the results of the B-EGC. Additionally, relatively saline water is found north of the release locations, around 70°N, 18.5°W, at the place where higher temperatures are found as well. Again, the saline trajectories found northward are in contrast with the fresher trajectories found southward.

The pattern of salinity resulting from the B-DS is shown in Figure 4.14. Overall, more saline water is found compared to the B-EGC. However, the figure shows stronger gradients compared to the mean model data and results of the B-EGC. These gradients seem to overlap with the gradients visible at the map of the temperature of the B-DS. North of 70°N, 18.5°W, a few saline trajectories are recognizable, however no sharp transition is visible like in the results of the B-EGC. At the location of the shEGC, the water seems to be fresher compared to the results of the B-EGC. Around 68.5°N, 23°W, the water is less saline and particles seem to have eddy-like behaviour. The water still becomes fresher near the shelf of Iceland, both west and east of the KR.

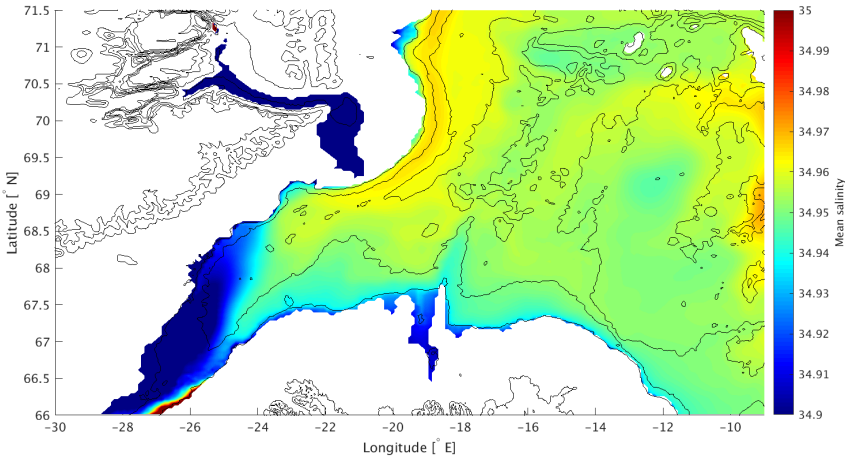

Figure 4.12: Map of the mean salinity between 02-01-2005 and 28-09-2016, at a depth between 399 and 635 meters from model data. Isobaths are drawn every 500 meters.

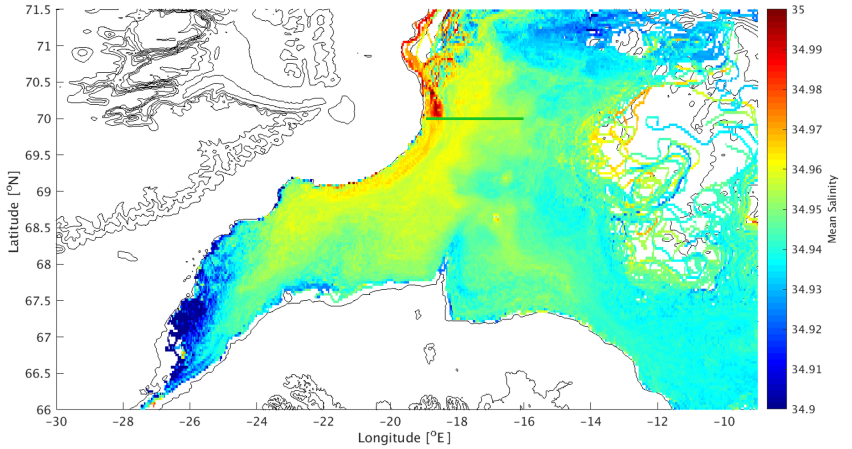

Figure 4.13: Mean salinity of trajectories remaining below a depth of 425 meters, as part of the B-EGC. The green line shows the release location of the particles.

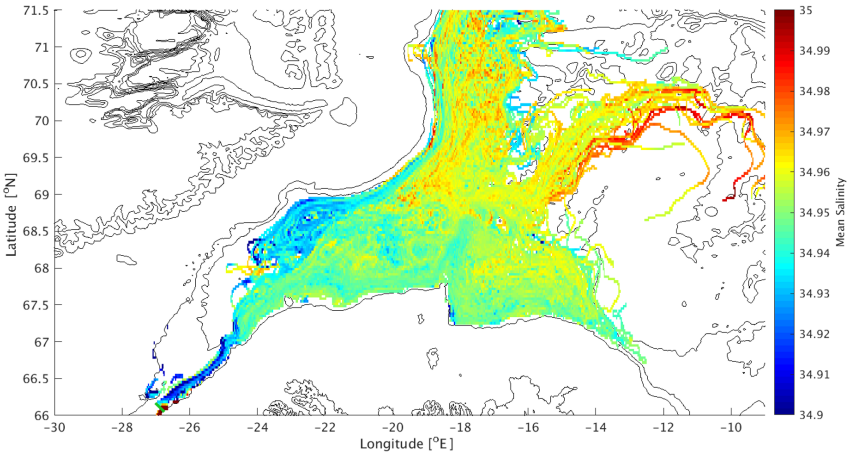

Figure 4.14: Mean salinity of trajectories remaining below a depth of 425 meters, as part of the B-DS. The green line shows the release location of the particles.

4.3.4 Potential density

The mean potential density is shown for the model data, the results of the B-EGC and B-DS in Figure 4.15, Figure 4.16 and Figure 4.17.

An overview of potential density which is calculated from the layers in the model data, is visible in Figure 4.15. Variations are visible at similar locations as the salinity and temperature. Near the sill, the density decreases. Fresher and colder water are found north-west of the sill, while warm, saline water is also found near the sill at the side of the Iceland shelf, indicating that no sharp transition in potential density took place near the sill. A change of the potential density is visible from less dense water near the shelf of Greenland to denser water. This change is also found near the shelf of Iceland. The core of the Iceland Sea gyre is found to be less dense than its surroundings.

Results of the B-EGC of potential density are visible in Figure 4.16. Overall, less dense water is found compared to the model data. Like in the model data, near the sill the water became less dense. Additionally, no sharp transition is visible by the density north of the release locations, around 70°N, 18.5°W. Since diffusion is taken into account in the model data, the density should be constant at the combination of relatively warm and saline water which is found.

In Figure 4.17, results of the B-DS are visible. As found in the results of potential density of the B-EGC, less dense water is found near the sill. Also in this case, no outstanding trajectories are found around 70°N, 18.5°W, because of the combination of warmer and more saline water which is found.

Suggestions of pathways of the EGC (1), EIC(2), NIJ(3), sEGC(4), shEGC(5) are marked in Figure 4.16 and Figure 4.17. The EGC shows less dense values, compared to the EIC. However, the rAW is still recognizable related to a density below 27.9 kg/m^3 as part of the B-EGC. Compared to the density from the B-EGC results, the EGC is less dense at results of the B-DS. The pathway of the EIC seems to be more clear in the results of the B-DS with a relatively higher density compared to the surroundings. The shEGC seems to be less dense compared to the sEGC, which is probably due to the warmer and fresher water which flows through the shEGC. Because of the differences in topography, particles in the shEGC can not travel as deep as in the sEGC. The NIJ seems the densest current and is becoming less dense when mixing with the sEGC and shEGC. The relatively cold temperatures found near the shelf of the KR are also found in the RAFOS trajectories [De Jong et al., 2018], which is further discussed in section 5.2. The NIJ is approximately similar in the B-EGC and the B-DS, as well as the sEGC. Density at the location where the shEGC flows is somewhat lower in results of the B-DS compared to the B-EGC. This pathway is likely to fluctuate more over time compared to the pathway given at sEGC. Differences in salinity north of (5) might be due to the eddies which are probably present in that area.

To conclude, several currents like the EGC, shEGC, sEGC, NIJ and EIC are recognizable by their hydrographic properties. An example is the rAW mass which flows through the EGC. There seems to be a warmer water originating from the EGC and a colder water which originates from the NIJ. Although in the model data the west of the KR is clearly colder, results from the both batches show colder temperatures at both sides west and east of the KR. Due to salinity, pathways which originate of the EGC are recognizable in the results of the B-EGC. The NIJ seems to be recognizable within the results of the trajectories due to the denser water. Since the trajectories vary in depth, the exact values related to a respective depth are still questionable.

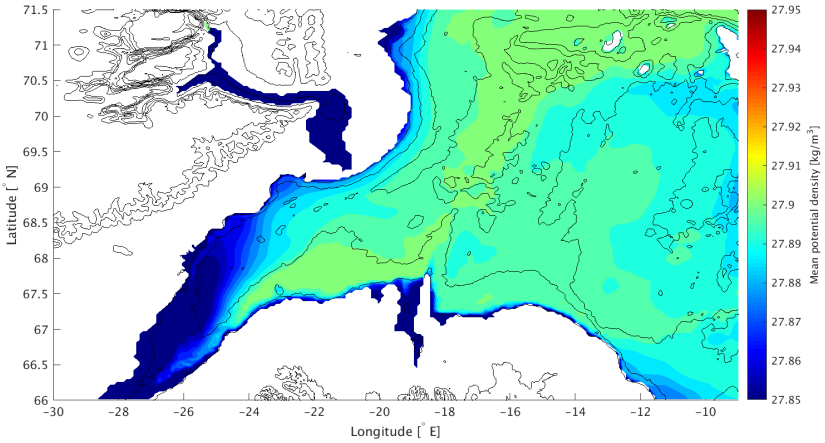

Figure 4.15: Map of the mean potential density between 02-01-2005 and 28-09-2016, at a depth between 399 and 635 meters from model data. Isobaths are drawn every 500 meters.

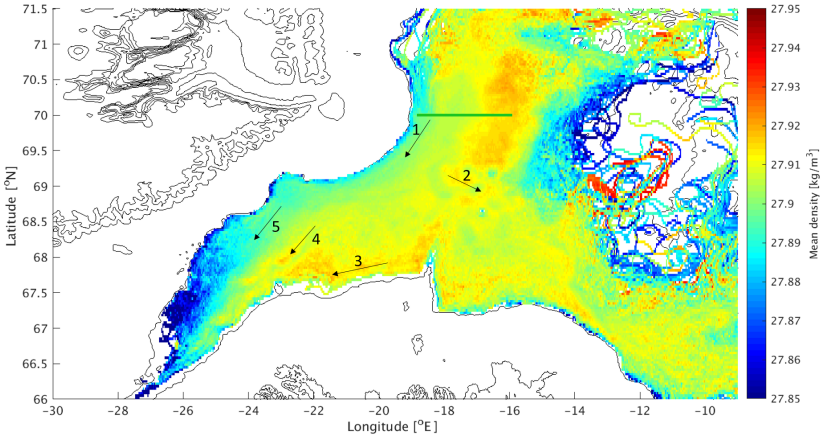

Figure 4.16: Mean potential density of trajectories remaining below a depth of 425 meters, as part of the B-EGC. The green line shows the release location of the particles. Suggestions of pathways of the EGC (1), EIC(2), NIJ(3), sEGC(4), shEGC(5) are marked.

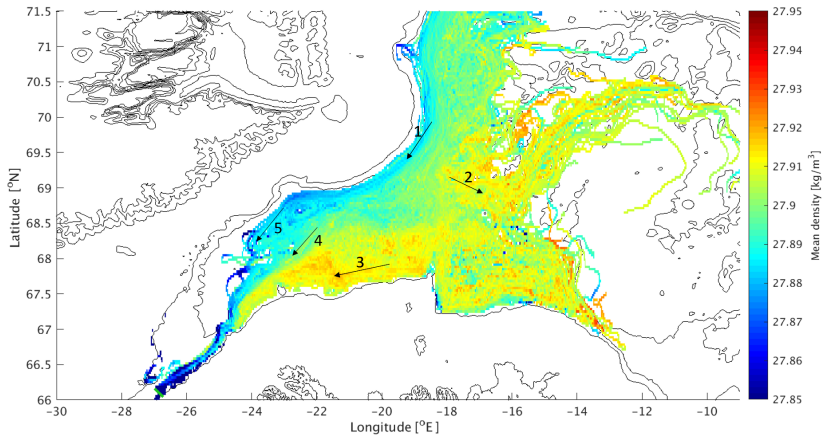

Figure 4.17: Mean potential density of trajectories remaining below a depth of 425 meters, as part of the B-DS. The green line shows the release location of the particles. Suggestions of pathways of the EGC (1), EIC(2), NIJ(3), sEGC(4), shEGC(5) are marked.

4.4 Mesoscale Eddies in model data

Trajectories are found to be strongly fluctuating on a monthly time scale. Additionally, Figure 2.2 shows features which seems to be related to eddy behaviour. It might be possible that these eddies play a significant role in the results of the particle trajectories. For this reason, mesoscale eddies are investigated in more detail. The eddy tracking software, which is already described in section 3.3, is used to find eddies. An overview of the results is shown in section 4.4.1. Section 4.4.2 describes properties of eddies which probably cross a transect near the DS. Finally, the possibility of a relation between the strengthening of a locked eddy and the deviation from the EGC to the EIC is described in section 4.4.3.

4.4.1 Overview of eddy results

Using the eddy tracking software described in section 3.3, some results about the detected eddies are summarized in Table 4.1. This table is split in two parts, one part with the results of the entire studied area, as visible in Figure 3.4. This area is defined between 66°N and 72°N, and between 12°W and 30°W. The second part of Table 4.1 is about the area around the DS only, which is the area of latitude 66.5°N and 69.5°N and longitude 27°W and 20°W. This area corresponds to the highlighted red contour, as visible in Figure 3.4.

Table 4.1: Properties of eddies found with eddy tracking software.

Property	**units**	**Complete study area**				**Around the Denmark Strait**			
		at center		**at edge**		**at center**		**at edge**	
		mean	**st dev**	**mean**	**st dev**	**mean**	**st dev**	**mean**	**st dev**
density	$[kg/m^3]$	27.9004	0.016	27.9008	0.015	27.9002	0.016	27.888	0.027
salinity	[-]	34.950	0.023	34.952	0.022	34.951	0.024	34.943	0.04
temperature	$[°C]$	0.59	0.25	0.60	0.24	0.60	0.25	0.70	0.33
velocity	$[m/s]$	0.01	0.01	0.02	0.02	0.01	0.01	0.04	0.03
radius	$[km]$			7.0	3.6			7.1	3.8
		amount	**percent**			**amount**	**percent**		
cyclonic		25977	53.8%			3374	49.2%		
anticyclonic		22270	46.2%			3491	50.9%		
total		48247				6865			

Mean properties are calculated at the center and at the edge of the eddies. The calculation of the standard deviation (st dev) is explained in appendix A.2. Properties like density, salinity and temperature are roughly the same in both areas. The overall mean radius of eddies is ±7.0 km. The mean radius within the area of the DS is ±7.1 km. It has to be taken into account that these values are averaged over both the cyclonic and anticyclonic eddies. The amount of cyclonic eddies is approximately similar to anticyclonic eddies in both cases, within the complete study area and around the DS.

From the center to the edge of an eddy, the temperature gradient of the eddy is steeper in the area near the DS, compared to the total area. The salinity is slightly increased in the complete study area. In contrast, the salinity in an eddy is slightly decreasing in the area around the DS. The same holds for the density, it is slightly increased to the edge in the complete study area and decreased to the edge in the area around the DS. Additionally, the swirl velocity at the edge is higher in this smaller area, which means that eddies have are probably stronger in the area around the DS, compared to the overall situation.

The relative probability distribution of the potential density within the center is shown for the anticyclonic and cyclonic eddies in Figure 4.18. Cyclonic eddies tend to have a higher potential density (blue), compared to the anticyclonic eddies, which include lighter densities (red). This is in agreement with the geostrophic balance, which states that the density in the core of a cyclonic (anticyclonic) eddy is higher (lower) compared to a situation without any eddy, as explained in section 3.4.

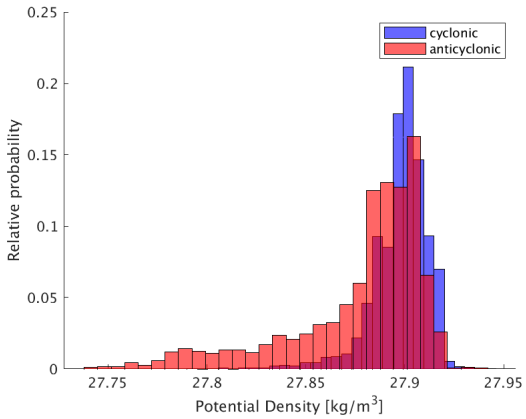

Figure 4.18: Relative probability of the potential density over centers of detected eddies in the area of the DS, at 547 meters depth.

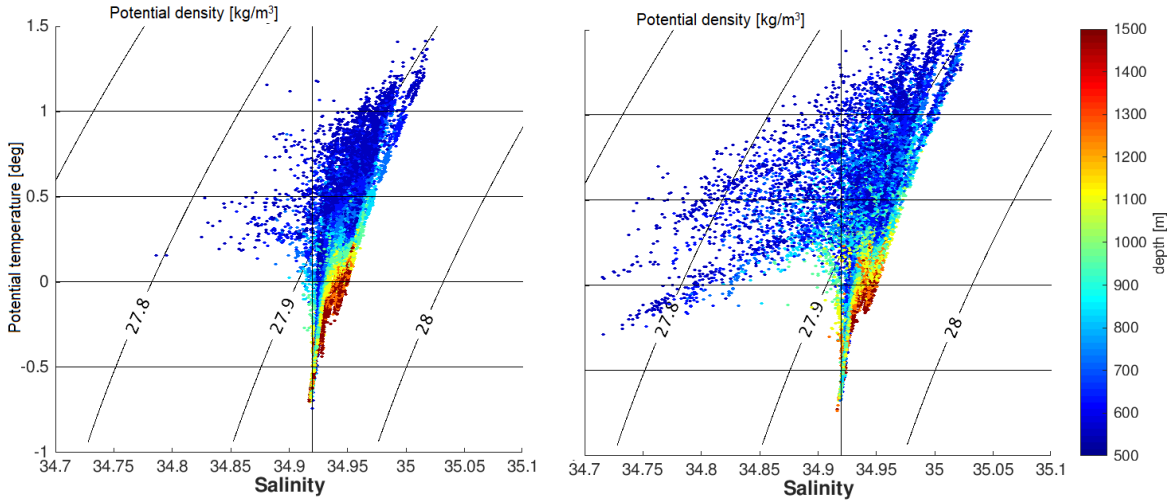

(a) Cyclonic *(b) Anti-cyclonic*

Figure 4.19: Temperature Salinity diagram (TS diagram) using properties found at the centers of eddies which are detect by the eddy tracking software at 547 meters. The properties at these locations are collected between 500 and 1500 meters. Horizontal black lines are plotted at a potential temperature of -0.5, 0, 0.5 and 1 degrees Celsius. The vertical line is plotted at a salinity of 34.92, to compare locations of the depth.

To investigate the differences between cyclonic and anticyclonic eddies in the entire study area, two Temperature Salinity diagrams (TS-diagrams) are shown in Figure 4.19. For all time steps and locations where eddies are found, values are plotted in the diagram over all depths in the model. For example, if a cyclonic eddy center is found at 68.8°N and 22°W at 01-01-2010, the properties from 500 to 1500 meters depth from the model data are plotted in Figure 4.19(a).

A combination of a relatively high temperature and a low salinity results in a relatively low density in case of an anticyclonic eddy. In contrast, at the same depth the density of a cyclonic eddy is relatively high. Comparing Figure 4.18 with Figure 1.4, hydrographic properties of the rAW and the AAW are clearly visible, especially in the case of the anticyclonic eddies. This suggest that the rAW found on greater depths are compared to the colder AAW. Near the surface, values of the PSW are also recognizable in both cases (not shown in Figure 4.18, since only properties of depths below 500 meters are taken into account).

4.4.2 Eddies on a transect near the Denmark Strait

In this section, we focus on the area near the DS. Properties like volume transport, potential density and potential vorticity are investigated over a transect near the DS, using calculations as described in chapter 3.2. The mean velocity and density are calculated between 02-01-2005 and 28-10-2016, which covered the entire time series of the dataset which is used in this project. In Figure 4.20, results of mean velocity (arrows) and mean density (colours) are plotted for a depth of 547 meters of the area near the sill around the DS. In this figure, small variations of velocity and density are visible over the area. A transect is made (purple line), using a linear interpolation of the model data. The location of this transect is chosen to be through the center of action. A center of action is defined as a maximum of the potential density variability. The location of the center of action is calculated by taking the highest standard deviation of potential density over a horizontal layer at 547 meters depth.

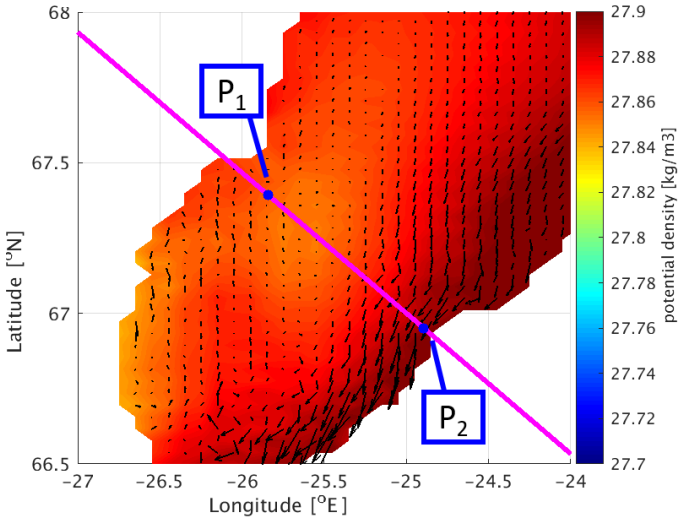

Figure 4.20: Mean velocity field (arrows) at 547 meters depth. Colours are related to the potential density, as shown by the colour bar. The purple line marks the location of the transects. Blue dots, marked by P_1 and P_2, correspond to coordinates of which the difference in potential density is investigated ($\Delta\sigma_0 = \sigma_{0,atP_1} - \sigma_{0,atP_2}$).

Mean properties perpendicular to the velocity, potential density and potential vorticity over the transect are shown in Figure 4.21. In this case, the velocity is predominantly south-westwards to the sill. The velocity in north-westward direction near the surface, (south at the plot) is the NIIC. To show the variations over depth, the potential vorticity is plotted on a logarithmic scale. The potential vorticity is almost horizontal, as well as the isopycnals, although both have a slightly upward displacement on the northern side (right).

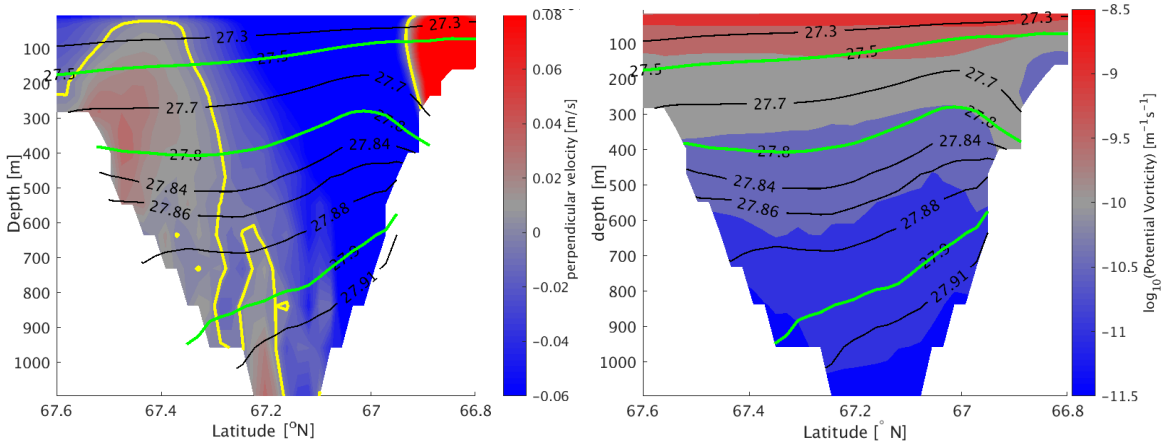

(a) Perpendicular velocity, where positive values correspond to a north-eastward flow and negative values correspond to a south-westward flow. Yellow lines correspond to a velocity of 0 m/s.

(b) Potential vorticity

Figure 4.21: Mean values of the transect as shown by the purple line in Figure 4.20. Black contour lines represent the potential density, of which values are written in the figure. Green lines correspond to a potential density of 27.5, 27.8 and 27.9 $[kg/m^3]$.

The variability over time of properties like volume transport, difference in potential vorticity and difference in potential density are shown in Figure 4.22. This figure shows normalized values to compare properties over time. Horizontal coloured lines show the original location of the zero-value. The normalization is explained in appendix A.1.2. The volume transport is calculated by using the perpendicular velocities taken over all depths of the transect at the purple line between points P_1 and P_2, as described in appendix A.3. Volume transport has values between -6.00 and 0.55 mSv, where a positive sign means a transport in north-east direction. The mean potential vorticity is calculated at the transect between P_1 and P_2, which is highlighted by the blue dots in Figure 4.20. The "Difference in potential vorticity" in this section means the difference between both sides of the transect (shown in Figure 4.21(b)) of the potential vorticity anomaly, which is the difference between the mean situation and a situation at a time step. Values of the difference in potential vorticity are between -3.69 and 4.43. The difference in potential density is defined in this project as the difference between P_1 and P_2 at 547 meters ($P_1 - P_2$). The difference in potential density has values between -0.141 and 0.067 $[kg/m^3]$.

Table 4.2: Results of calculated R-values of several properties like potential density (PD), potential vorticity (PV) and volume transport (VT).

R-value	**VT between P_1 and P_2**	**Δ PV**	**Δ PD**
Δ PD	0.5686	0.2731	
Δ PV	0.3575		0.2731
VT between P_1 and P_2		0.3575	0.5686
VT between P_1 and P_2 and with $\sigma_0 < 27.8$		0.3808	0.2784
VT		0.1692	0.1062
VT with $\sigma_0 < 27.8$		0.4081	0.2353

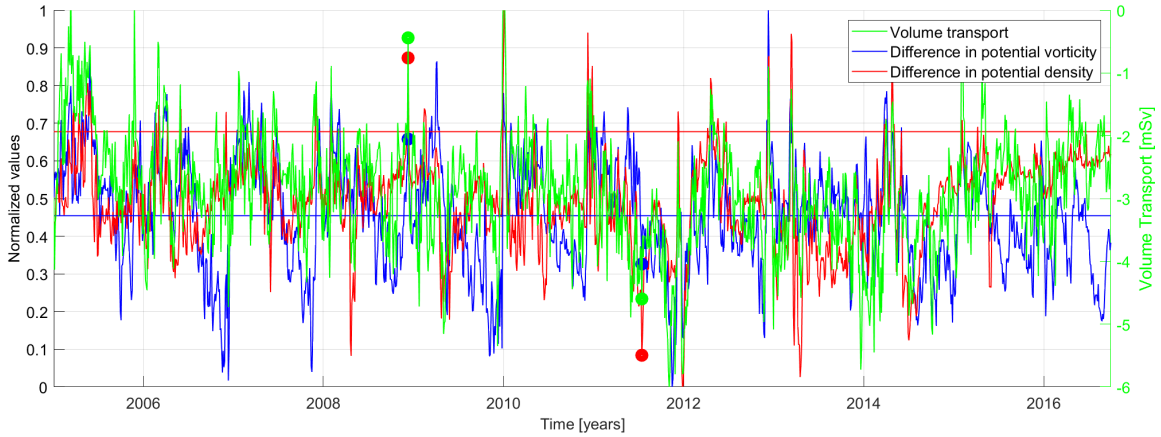

Figure 4.22: Time line of different properties, as shown by colours in legend. Differences in potential vorticity and potential density are scaled in a range between 0 and 1 (normalized, origin of the values are explained in text). The volume transport is related to the right y-axis. Vertical coloured lines show the original location of the zero-line. Dots are plotted as an example for high values (low values), corresponding with weak (strong) volume transport to the DS at a time step, which is investigated in more detail in this project.

In time, values are highly fluctuating as visible in the graph. Overall, a seasonal cycle at the difference in potential density seems to be visible, with lower values in winter and higher values in summer. The correlation coefficient is calculated with the Pearson linear correlation, as explained in appendix A.4. Results are shown in table 4.2. Additionally, the R-value is calculated between the volume transport of the denser water, which is considered as a density more than 27.8 kg/m^3. Although the correlation coefficient is relatively low, all p-values are approximately zero, which corresponds to a significant correlation in R and a low probability of observing the null hypothesis. The volume transport over the entire section seems to be less correlated. The correlation between the difference in potential density and volume transport between P_1 and P_2 is probably highest because the difference in potential density is also related to these points. The difference in potential vorticity and volume transport of a water which is denser than 27.8 kg/m^3 is has the highest correlation, probably because the denser water is less stratified. The properties are correlated, but differences at one depth does not explain everything.

Two time steps are investigated in more detail in this project, marked with coloured dots related to their property in Figure 4.22. A case with a weak volume transport to the DS and relatively higher values of the difference in potential density and vorticity is taken at 09-12-2008. A case with stronger volume transport to the DS and lower values of the difference in potential density and vorticity is taken at 15-07-2011.

A case of study for weak volume transport to the DS

Figure 4.23(a) and Figure 4.24 show examples from a situation related to relatively high values for the difference in potential density and a weak volume transport. Comparing values of the velocity and the potential density at the mean situation and at the time step with relatively high values, Figure 4.20 and Figure 4.23(a) respectively, differences are clearly visible. Comparing the high velocity with the mean velocity at a depth of 547 meters, velocities are higher at some locations, for example near point P_2. A clear anomaly of a low potential density is visible near point P_2, which means the difference between P_1 and P_2 is getting bigger, related to relatively higher values for the difference in density. This is due to

the presence of an eddy nearby P_2 at this time, as visible by the direction of the velocity. However, no eddy is traced at this time step with the eddy tracking software.

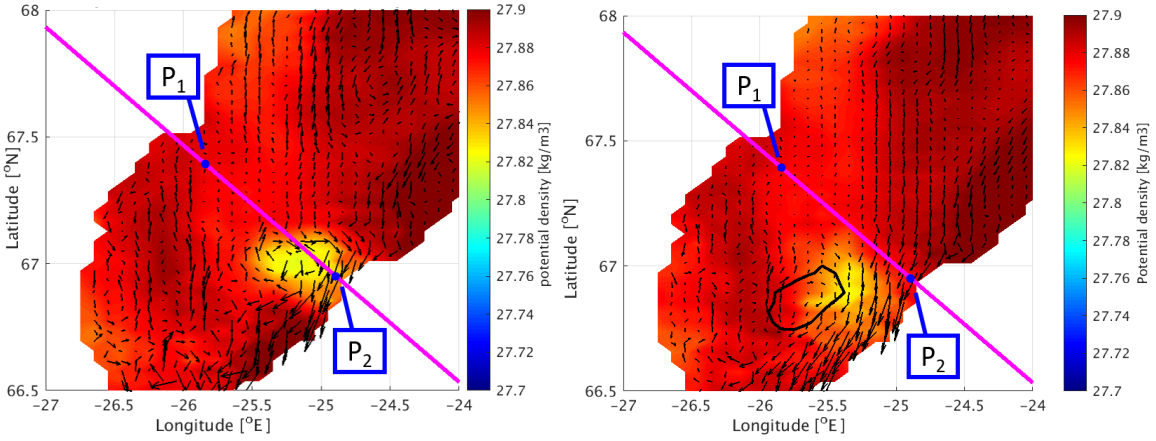

(a) 09-12-2008 *(b) 12-12-2008*

Figure 4.23: Similar to Figure 4.21. In this case values are for one day, related to a weaker volume transport to the DS and high values for the difference in potential vorticity and density, as shown in Figure 4.22. The black contour shows the eddy tracked by the eddy tracking software.

Additionally, the map of the next time step (12-12-2008) is shown in Figure 4.23(b). At this time step, an eddy is traced by the eddy tracking software of Nencioli et al. [2010], as shown by the black contour. Values of volume transport and difference in potential density at the transect are not extremely high for this time step, since the eddy no longer exist through the transect. The tracked eddy is as an anticyclonic eddy with a mean radius of ± 11.4 km, which is relatively large compared to the mean radius of eddies found in the area of the DS. The eddy has a temperature of $1.02°C$, a salinity of 34.9 and a density of 27.9 kg/m^3 at the center. This is warmer compared to the surroundings. The swirl velocity of the eddy is 0.08 m/s.

Transects of the perpendicular velocity and potential density of the mean situation and the time step with high values are visible in Figure 4.21 and Figure 4.24, respectively. Comparing both transects of the perpendicular velocity (Figure 4.21(a) and Figure 4.24(a), respectively), the velocity seems to be more in the north-eastward direction (more positive values (red) are recognizable). In this case the volume transport becomes more positive, related to relatively higher values for volume transport as shown in Figure 4.22.

Considering the isopycnal at 27.8 kg/m^3 (green) in the transects, a slightly downward displacement is visible, as well as an upward displacement (Figure 4.21). In the case with relatively high values, two downward displacements of the isopycnal are recognizable. This is in contrast with the mean situation, where an upward displacement was visible. At this downward displacement, the perpendicular velocity sharply turns from the north-eastward direction (red) to the south-westward direction (blue). Considering the subsurface as well, this transition can be considered as the location of a core of an eddy. Since the isopycnal at 27.5 kg/m^3 does not show a clear downward displacement, it seems like the core of the eddy lies within these isopycnals, at 27.5 kg/m^3 and 27.8 kg/m^3. This is in agreement with the theory explained in section 3.4, which states that at the location of an anticyclonic eddy, isopycnals are further apart from each other. Compared to the mean values, the pattern of potential vorticity is not almost horizontal anymore. Instead, a lens is visible at the south side (right) of the transect. The thickening of the layer between the isopycnals leads to a

lower potential vorticity. This means that the situation is less stratified compared to the mean situation.

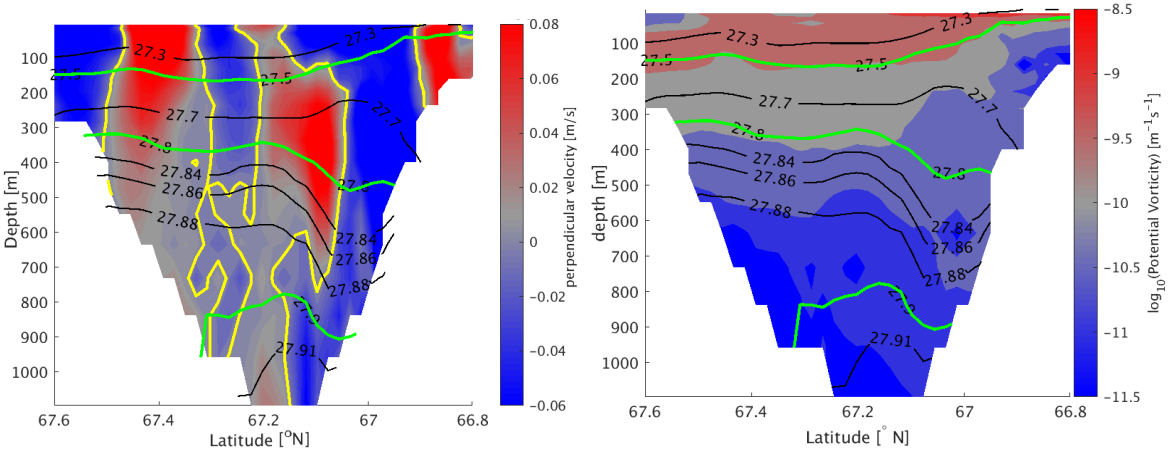

(a) Perpendicular velocity *(b) Potential vorticity*

Figure 4.24: Similar to Figure 4.21. In this case transects are plotted for just one day, at 09-12-2008, related to a weaker volume transport to the DS and high values for the difference in potential vorticity and density, as shown in Figure 4.22.

A case of study for strong volume transport to the DS

Figure 4.25 and Figure 4.26 correspond to the case with stronger volume transport and lower values for the differences in potential vorticity and potential density. This time step can be compared to the mean values and the case with relatively high values. A clear difference is visible at the map which shows the potential density, in Figure 4.25. In the case with weak volume transport, the lowest density is found at point P_2. In contrast, in the case of stronger volume transport, the lowest density is clearly visible at point P_1. This is probably because an eddy is passing the transect nearby P_1 at this time step, as visible by considering the velocities, although this structure is again not recognized as an eddy by the eddy tracking software.

Figure 4.26 shows the transects of this time step. The transect of the perpendicular velocity show a clear contrast to both the mean values and the case with weaker transport. In the case with strong volume transport, the direction of the velocity is mostly south-west (negative velocity), in contrast to the case with weak volume transport. This results in a negative value for the volume transport. Additionally, considering the isopycnal of 27.8 kg/m^3 (green) in the transects, a downward displacement as well as an upward displacement is visible. In contrast to the case with a weak volume transport, in this case the shape of the isopycnal seems to be an exaggerated version of Figure 4.21, the mean situation. At the location of the downward displacement in Figure 4.24(a), it appears that the perpendicular velocity is turning around at roughly 67.1°N. This pattern is also visible at the location of the downward displacement at roughly 67.4°N in the case with of a strong volume transport, in Figure 4.26(a). The eddy is clearly visible in the transects. In contrast to the case with weak volume transport, the shape of the isopycnal and corresponding downward and upward displacements are still recognizable at the isopycnal of 27.5 kg/m^3, although they become smaller, which means the core of the eddy is found higher, corresponding to a less dense environment. The potential vorticity in this case seems to be the opposite of the case with

relatively high values. This means that the northern side of the transect is less stratified, which corresponds to the suggested location of the eddy.

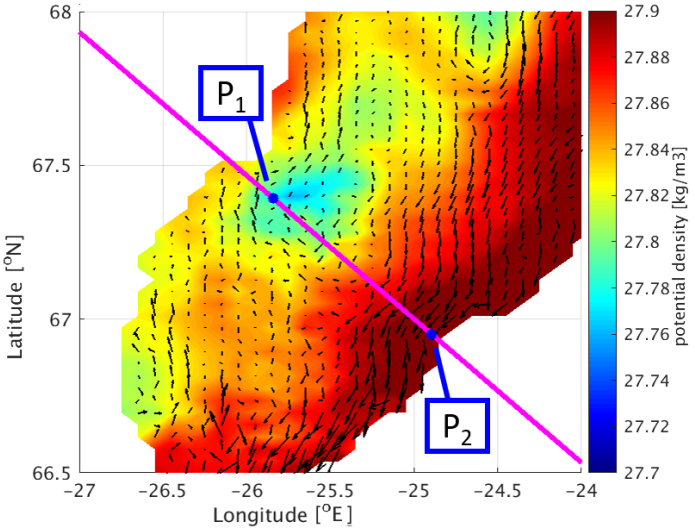

Figure 4.25: Similar to Figure 4.20. In this case values are for one day, taken at 15-07-2011, related to a stronger volume transport to the DS and low values for the difference in potential vorticity and density, as shown in Figure 4.22.

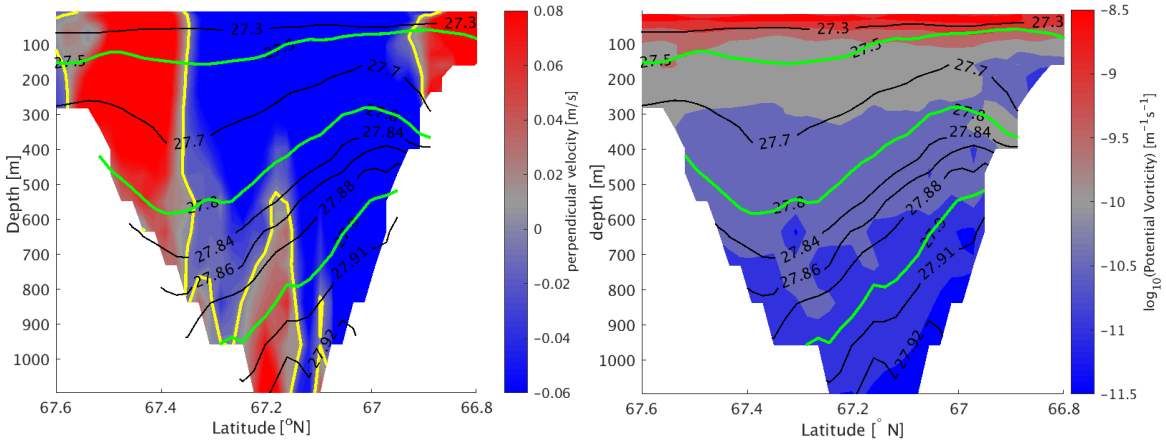

(a) Perpendicular velocity *(b) Potential vorticity*

Figure 4.26: Similar to Figure 4.21. In this case transects are plotted for just one day, at 15-07-2011, related to a stronger volume transport to the DS and low values for the difference in potential vorticity and density, as shown in Figure 4.22.

To conclude, changes in volume transport, potential vorticity and potential density are found, pointing the presence of varying eddies at a depth of 547 meters.

4.4.3 Diversion of the East Iceland Current from the East Greenland Current

In this section, we focus on an area where a part of the EGC diverts into the EIC. During investigation of the results of the trajectories which are part of the B-EGC, it appears that particles flow north-eastward through the EIC or south-westward through the EGC, as roughly described in section 4.2. For this reason, the area between latitude 68.8°N and 69.1°N and longitude 17.5°W and 16.7°W, is investigated in this section. As visible in Figure 2.2, it seems that an eddy, which is locked due to the topography, is recognizable by the mean values of velocity at this location. This area corresponds to the highlighted orange box in Figure 3.4, as well as the highlighted orange box in Figure 4.27.

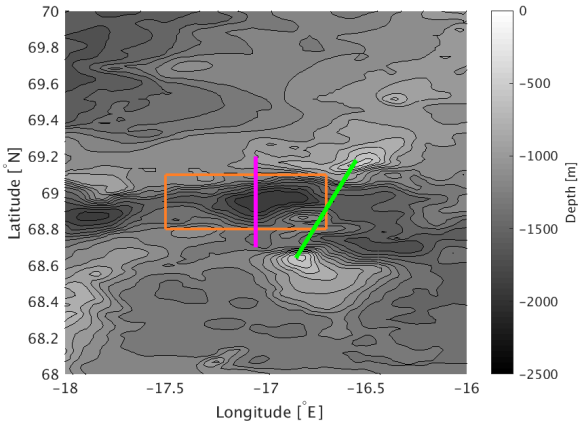

Figure 4.27: Topography in the investigated area, isobaths are drawn every 100 meter. The orange box highlights the area of which eddies are tracked with the eddy tracking software. The purple line correspond to location where transects are made. The volume transport and particles are counted over a transect of the green line.

Using the eddy tracking software, 1165 cyclonic and 4 anticyclonic eddies are found in this box between 02-01-2005 and 28-09-2016 at a depth of 547 meters in the model data. The mean radius of these eddies is ±6.1 km. The strength of the cyclonic eddies found within this area is fluctuating. The anticyclonic eddies are considered as negligible in this case.

Figure 4.28 shows two examples of time steps of the velocity and potential density over the investigated area. The plots are made using the model data at 28-04-2012 in Figure 4.28(a) and at 24-02-2015 in Figure 4.28(b), to compare two different cases of an eddy in the investigated area. As described above, the expectation was that a locked eddy exists. Differences of velocities are visible in arrows. Using the eddy tracking system, an eddy can be detected in the velocity field. In Figure 4.28(b) a traced eddy is shown, while at the same location in Figure 4.28(a) no eddy is detected. The potential density anomaly (gradient in colours) corresponds to the arrows. The tracked eddy is an cyclonic eddy with a mean radius of ±6.7 km, which is smaller compared to the mean radius found in the entire investigated area. The eddy has a temperature of $0.41°C$, a salinity of 34.95 and a density of 27.91 kg/m^3 at the center. The swirl velocity is 0.06 m/s. The temperature is lower compared to the mean temperature of the entire study area, and both the swirl velocity and density are higher, which are related to cyclonic features.

For the same time steps, transects are made through the eddy, between 68.7°N and 69.2°N and at a longitude of 17.05°W, as shown by the purple line in Figure 4.27. Results are visible in Figure 4.29. In Figure 4.29(a), the weakening of the perpendicular velocity is clearly visible at a depth around 500 meters and a latitude of between 68.8°N and 68.9°N.

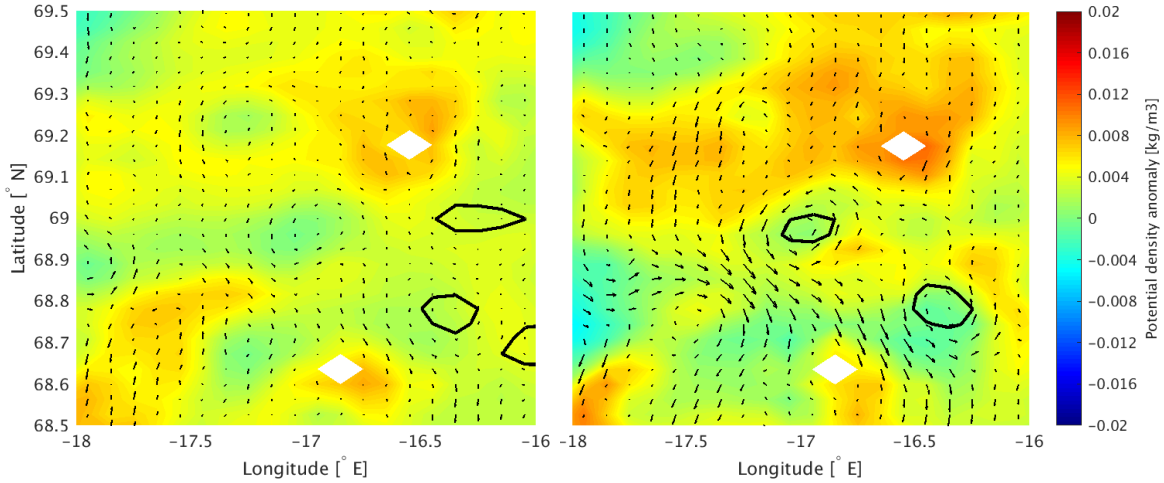

(a) Date: 28-04-2012, related to a time step with low volume transport.

(b) Date: 24-02-2015, related to a time step with high volume transport.

Figure 4.28: Mean velocity field (arrows) at 547 meters depth. Colours are related to the potential density, as shown by the colour bar. The black lines are the edges of eddies found by the eddy tracking system.

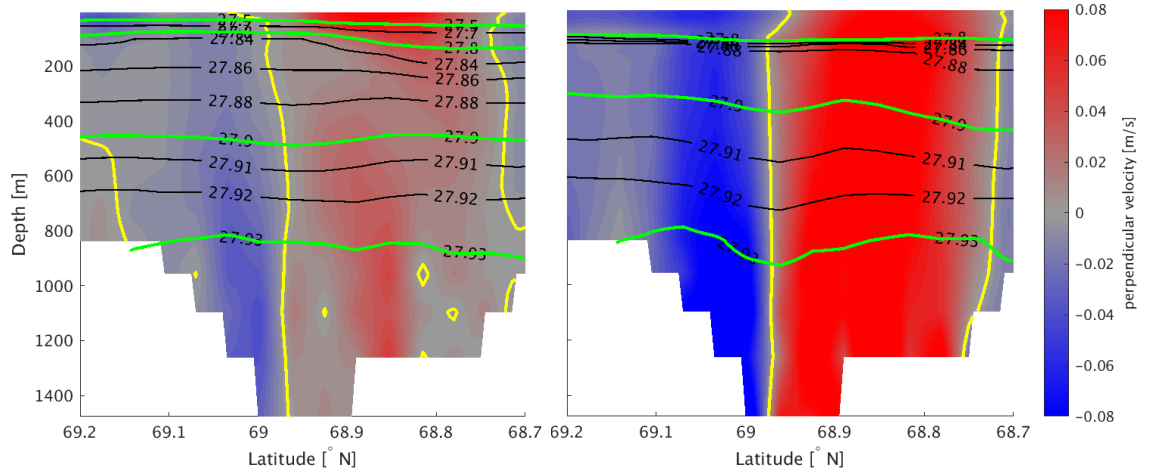

(a) Date: 28-04-2012, related to a time step with low volume transport.

(b) Date: 24-02-2015, related to a time step with high volume transport.

Figure 4.29: Transects are made at the location of the purple line in Figure 4.30, at two different time steps. Values of perpendicular velocity (positive values correspond to a north-eastward flow and negative values correspond to a south-westward flow) correspond to the colour bar. Black lines correspond to the potential density, values are written in figure. Green lines correspond to a potential density of 27.5, 27.8 and 27.9.

Comparing this with Figure 4.29(b), the strengthening is visible due to the bright red colour. Additionally, differences in the pattern of the isopycnals are roughly visible. As visible in Figure 4.29(a), near the surface at the point where velocities switch sign, the structure of the isopycnals become more like the structure of a typical cyclonic eddy, compared to the theory described in section 3.4. At a depth of roughly 500 meters, differences in strengthening of this eddy at both time steps is clearly visible.

To investigate a potential link between the strengthening of the eddy and the direction of the particles from the trajectories, several parameters are investigated, as shown in Figure 4.30 and Figure 4.31. In Figure 4.30, the mean velocity at the edge of all cyclonic eddies found in the area described above is shown by the black line. The volume transport is shown by the green line, related to the right y-axis. This volume transport is calculated over all depths of the transect between 68.64°N, 16.85°W and 69.18°N, 16.55°W, as shown by the green line in Figure 4.27. A positive volume transport is defined north-eastward. Calculation of the correlation is explained in appendix A.4. The correlation between the eddy velocity and the volume transport is 0.5467 (R-value), with a p-value of 0, which corresponds to a significant correlation in R.

Figure 4.31 shows the amount of particles which cross the same section of which the volume transport is calculated, from results of the B-EGC. The date when the particles cross the line ("cross date") is shown by the red line. The release date ("launch date") on which the particles start at latitude 70°N is shown by the blue line. However, considering Figure 4.2 again, it seems like particles are roughly passing the investigated area between 90 and 140 days. Consequently, the amount of 115 days is added to the original launch date, which is considered as mean the time between the launch date and the date when the particles have to cross the line.

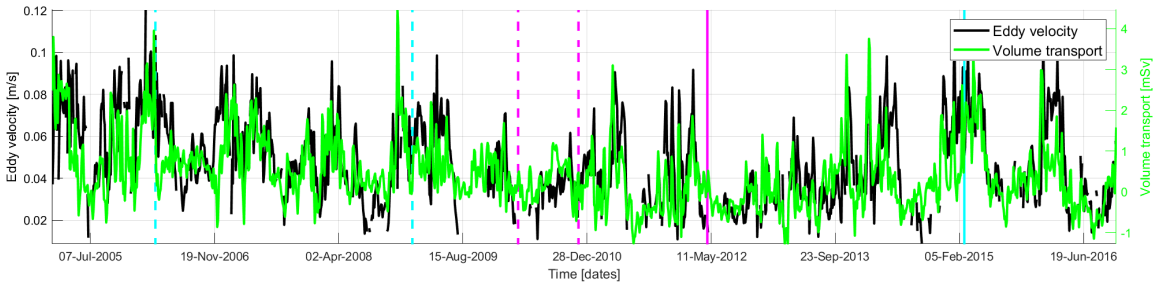

Figure 4.30: Timeline using the dataset of Köhl et al. [2007] showing the mean velocity at edge of the eddies at the right y-axis and the volume transport related to the right y-axis. Cyan (purple) lines correspond to examples of situations with relatively high (low) values, which are shown in section 4.2 and appendix B.

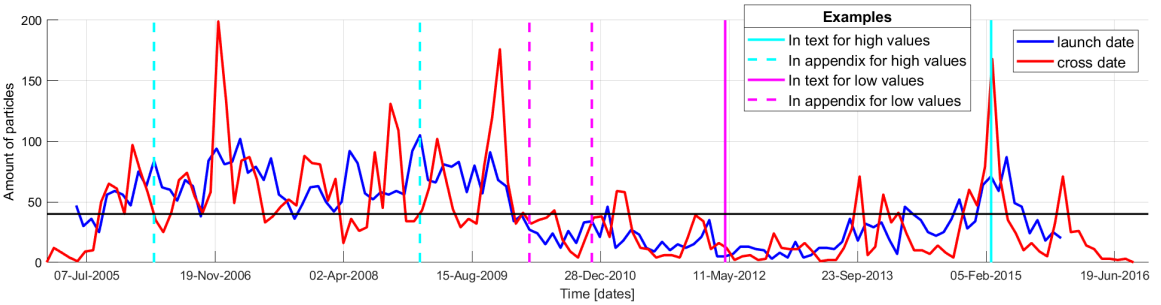

Figure 4.31: Timeline using the dataset of Köhl et al. [2007] showing the amount of particles which cross the a line (green line in Figure 4.27). The red line shows the counted amount of particles related to the cross date and the green line shows the counted amount of particles related to the launch date (added 115 days), which corresponds to the right y-axis. Cyan (purple) lines correspond to examples of situations with relatively high (low) values.

A start-up error is taken into account by considering the cross date. Since particles need time to travel from the release location to the investigated area, in the first months are less particles counted. However, particles of the B-EGC which cross the section are comparable

over time since the launches are consistently done each month. An advantage of taking the cross date into account is gaining a better reflection of the situation at a respective date. When counting from the cross date, it is not necessary to add an amount of days to overlap distance which particles have already travelled from their release coordinate.

The mean amount of particles which crosses the line is roughly 42 for the cross date, while the mean amount of particles is roughly 38 for the launch date. Particles counted by the cross date are more spread out. To investigate relatively high or low values, a line of mean values is plotted horizontally at a number of 40 particles (black line).

In both cases where particles are counted over the transect (red and black lines in Figure 4.31), they are roughly following the calculated mean velocity at edge of an eddy and volume transport (black and green lines in Figure 4.30). For example, in Figure 4.30 both amounts or particles are relatively high, at the cross date and launch date at the time step visualized by the cyan line (28-04-2012). This overlaps with a situation with high volume transport and a high velocity at the edge of an eddy, as is visible in Figure 4.31. The opposite pattern is visible at the time step with the purple line (24-02-2015).

The direction of the particles is probably related to the strengthening of the eddy. This is investigated in more detail at a time step with relatively high and low values, marked with cyan and purple lines, respectively. These lines are visible at the same time steps in Figure 4.30 and Figure 4.31. At 24-02-2015 (solid cyan line), all values are relatively high, while at 25-04-2012 (solid purple line), values are relatively low. The solid lines for relatively low and high values of counted particles, volume transport and eddy velocity can be compared to Figure 4.5(a) and 4.5(b), respectively from section 4.2. Within these figures, particles went clearly to different directions; in Figure 4.5(a) they flow more south-westward into the DS, which overlap with the case no eddy is detected.

While the launch date in Figure 4.5(a) was given as 01-01-2012, the solid purple line is stated at 28-04-2012, by taking the travel time into account. The same applies to the strengthening of the eddy, which is linked to Figure 4.5(b), with a launch date at 01-11-2014. The solid cyan line is set at 24-02-2015, where 115 days are added again to compare the results of the trajectories with the graph. At this solid line, relatively high values for volume transport are visible, as well as high speeds at the edges of the eddies. Additional examples for a relatively strong volume transport at 25-03-2006 and 23-01-2009 can be found in appendix B, for the cases indicated by the dashed cyan lines. Additional examples for a relatively weak volume transport at 25-03-2010 and 23-11-2010 can be found in appendix B as well, as indicated by the dashed purple lines.

To conclude, considering the results of the particle trajectories in the model data, it appears that strengthening of the eddy within the investigated area is probably related to the diversion of the EGC and the EIC.

5. Discussion

This chapter discusses results from several investigations. First, a suggestion of pathways of the DSOW is presented in section 5.1. Results are compared with previous studies, as described in section 5.2. Errors and accuracy are considered in section 5.3 and subsequently recommendations of further research is given in section 5.4.

5.1 Suggestion of DSOW pathways

Based on the results of this project, a sketch is made of the suggested pathways of the sources of the Denmark Strait Overflow Water (DSOW), which is visible in Figure 5.1. Blue lines show the pathways with arrows corresponding to the direction (the length of the arrow does not correspond to a suggested magnitude). Circles with a light blue colour correspond to suggested cyclonic eddies at a fixed location over time. Transparent elliptical areas in red (blue) correspond to anticyclonic (cyclonic) eddies which vary in location and strength. One suggestion is that due to these fluctuating eddies, the source and of the pathways of the DSOW can change between the strengthening of the currents over time.

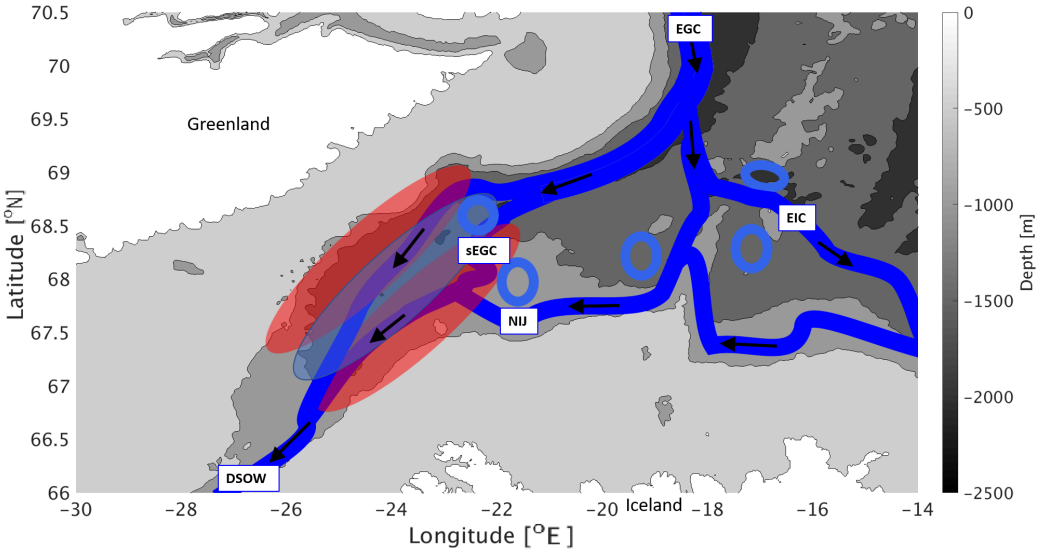

Figure 5.1: Suggested pathways of the sources of the Denmark Strait Overflow Water (DSOW). Light blue circles are related to staggered cyclonic eddies. Time dependent cyclonic (anticyclonic) eddies can be present, which is highlighted by the blue (red) areas. Acronyms: East Greenland Current (EGC), East Iceland Current (EIC), separated East Greenland Current (sEGC), North Icelandic Jet (NIJ).

5.2 Previous research

Foldvik et al. [1988] investigated results of year-long moored measurements at the EGC, more northerly compared to the investigated area in this research (near 79°N). They found mesoscale structures in the records, where they interpret much of these as trains of eddies and eddy-pairs with cross-stream length scales of order 10 km near the surface. This is the same order as found in the model. However, since Foldvik et al. [1988] concluded that the impact on fluxes of the EGC is too small. On the other side of the sill, southward of the DS, Bruce [1995] observed numerous cold cyclonic eddies at the surface in satellite infra-red imagery. The eddies move south-westward along the south-east edge of the EGC. Considering eddies on both sides of the DS, Bruce [1995] concluded that the existence of eddies at the surface in between their investigated areas is not excluded. Since the sill has a depth of around 600 meters, an option is that surface eddies around the DS do have a relatively higher impact on fluxes in this area.

Observational data from 2012 in the area around the DS is investigated by Håvik et al. [2017]. They found both cyclonic and anticyclonic eddies. They suggest that the eddies were formed due to baroclinic instability of the sEGC and both types of eddies are formed. Due to baroclinic instability, cyclonic eddies tend to spin down more readily, so that anticyclonic eddies typically dominate [Lilly et al., 2003]. This agrees with the overview of suggested pathways, as already shown in Figure 5.1, where anticyclonic eddies seem to dominate in the area near the DS. It has to be taken into account that the presence of eddies is probably a highly time dependent process.

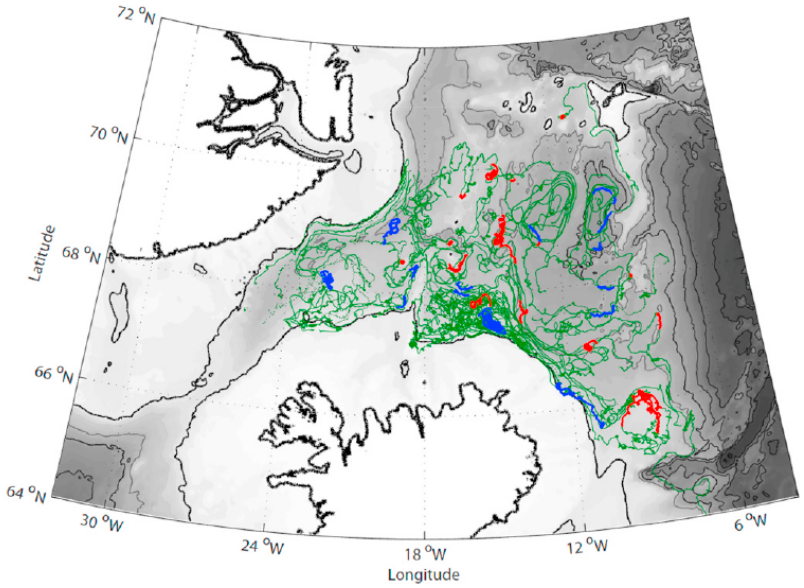

Figure 5.2: Results of the eddy detection wavelet analysis, as shown by De Jong et al. [2018]. Original float tracks are drawn in green. Sections of float tracks identified as exhibiting coherent cyclonic (anticyclonic) behaviour are drawn in blue (red).

Observational trajectories were investigated by De Jong et al. [2018], as described in section 1.5. Although the amount of released RAFOS floats is a fraction of the released particles in the model data, resulting trajectories can still be compared with each other. Figure 5.2 shows results of eddy detection by wavelet analysis of all analyzed trajectories from the RAFOS floats by De Jong et al. [2018]. Tracked cyclone (anticyclone) behaviour is visible in blue (red). In general, the observed eddies were smaller than the eddies which can be resolved in the model data. The shown tracks can be compared to the suggested pathways of sources, as visible in Figure 5.1. Within the areas where fluctuating eddies were suggested, some cyclonic behaviour is tracked within the float trajectories. Also some cyclonic behaviour is visible at locations were fixed eddies were suggested.

RAFOS floats which travelled through the investigated areas in this project are plotted in Figure 5.3. Several areas are investigated in this project. Within the area near the DS, related to box A, time depended anticyclonic eddies are suggested. Although there is no cyclonic behaviour visible in the blue trajectory through box A, the float related to the red pathway is turning around to the north and back. The floats were released at the location where the EGC is suggested, as visible by the black dots in box B. Slightly after the release, some eddies are already visible, for example at the green trajectory in box B. Locations of these eddies are not investigated in more detail in this research. The area near the KR (box C) is investigated, where sharp transitions in hydrographic properties were found.

For example, the relatively colder temperatures which were found in the floats near the shelf [De Jong et al., 2018], were also found in the trajectories as a result from the model data. De Jong et al. [2018] suggested that this could be deeper, colder water being driven up the slope. Additionally, no connection of floats which were released east of the KR and flow to the west of the KR is visible in box C.

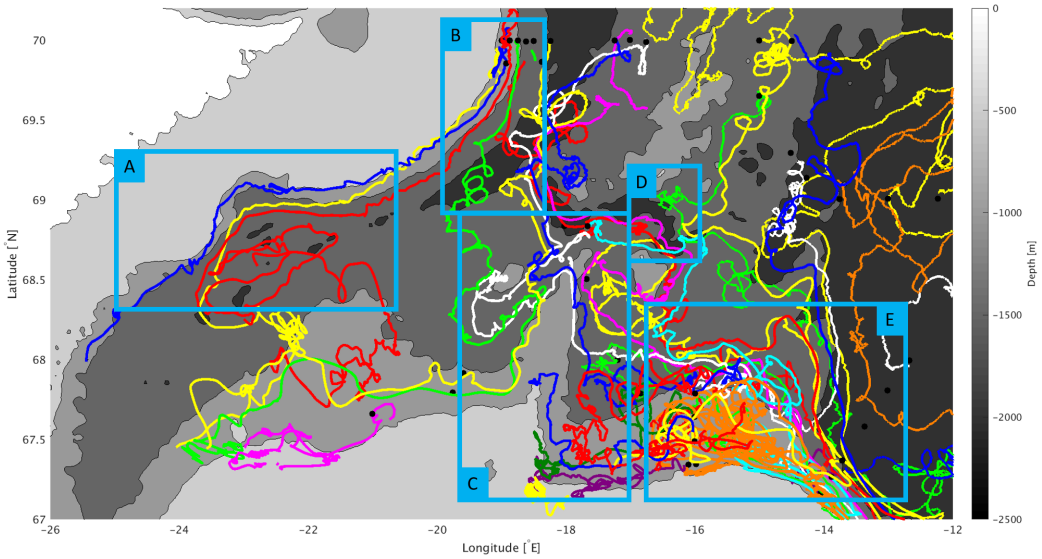

Figure 5.3: Float tracks of RAFOS floats (colours) with in black the launch positions. Boxes are drawn to highlight areas interesting areas where floats travelled through, which are explained in text. The 500m isobath is drawn in black. RAFOS float data used is described by [De Jong et al., 2018].

Results of this project suggest an eddy-related diversion from the EGC into the EIC. Floats through the EIC should pass box D. Within this box, an eddy is indeed visible at one trajectory of the floats (red). However, no eddy-like behaviour is visible at the trajectory in purple in box D. Results of the B-DS suggest that some particles seem to be turning within the area in box E. Probably due to the EIC particles flow to the eastward direction, however some particles turn into the westward direction and flow along the Iceland shelf to the KR. The turning of particles is not visible at the floats, as described by De Jong et al. [2018]. Våge et al. [2013] suggested that the NIJ exists west side of the KR, related to several mechanisms between the water mass through the NIIC and water from the Iceland Sea gyre, as described in section 1.3.3. A flow along the Iceland shelf west of the KR to the NIJ east of the KR is found at greater depths in the results of the particles released in the model data. However, no connection of the EIC nor the Iceland Sea gyre is found. To conclude, the connection between the east side and west side of the KR with their hydrographic properties and its mechanisms is still questioned.

Saberi et al. [2019] have released particles in a higher resolution model with a time series of one year. They consider that it was possible to detect different properties of the water mass which are related to different directions where the particles came from. Particles from the north to the DS became warmer, more saline and slightly lighter during their trajectory. Particles from the south became colder, fresher and denser during their trajectory. Additionally, they suggest that the separation of the EGC happens at multiple locations in the form of intermittent currents, where particles do not stay at one current at all time like the EGC, sEGC and NIJ. This overlaps with the results of this research, where the intermittent currents can be related to the time-depended eddies and no clear main route of the DSOW is found.

Comparing results of Saberi et al. [2019] with results of section 4.3, in both cases the temperature is increasing over the sill of the DS, as well as the salinity. Saberi et al. [2019] suggested that this is due to the overlying warmer and saltier water mass. Since both temperature and salinity are increasing, the potential density is decreasing, which is also visible in the results of the mean model data and trajectories from the B-DS and B-EGC. However, Saberi et al. [2019] found that the hydrographic properties remain almost constant before passing the sill. Slightly different results are visible in the results from this project, where the hydrographic properties seemed to be dependent to the pathway (EGC or NIJ) of which a particle came from.

5.3 Consideration of caveats

Like every research, this project has several caveats. In this section, some caveats are discussed:

- Only advection is taken into account by OceanParcels. If diffusion was taken into account as well, this would have influenced the results of the trajectories and these should be more realistic. One example of a resulting trajectory is shown in Figure 5.4. In this figure it is visible that the particle crosses different isopycnals. Since the particle is released at a depth of 525 meters, the particle is changing a lot, down to almost 1000 meters. At this location, there might be an eddy. This change in depth seems too much for just a process with conservation of density. Since mesoscale eddies are probably more important than thought before, it is possible that the diffusion is more important than thought before.

  If the particle is ascending, the density decreases, which means the water becomes warmer and fresher. However, this energy has to be compensated by other particles, since energy can not be lost. In this simulation, the energy of the particles is not relative to other particles and thus the ascending and descending of particles is probably exaggerated.

- Although the model data has a relatively high resolution, a higher resolution should be better to resolve eddies. In this project, it is possible that smaller scale eddies are missed, for example smaller eddies which are found in observations. Though eddies are found within the current model resolution and on a relatively long time series. Consequently, this research assume that the effect of missing eddies is negligible for the scale of this research.

- The model data depends on the input parameters of the model, for example to the viscosity and diffusivity. It appears that the depth of the isopycnal at 27.8 kg/m^3 become less deep over time, which means the overall density increases. This seems to be mainly due to the increase of salinity over time. Since the output of a model was available for this project and this research did not focus at longer time-scales than 10 years, this is not investigated in more details.

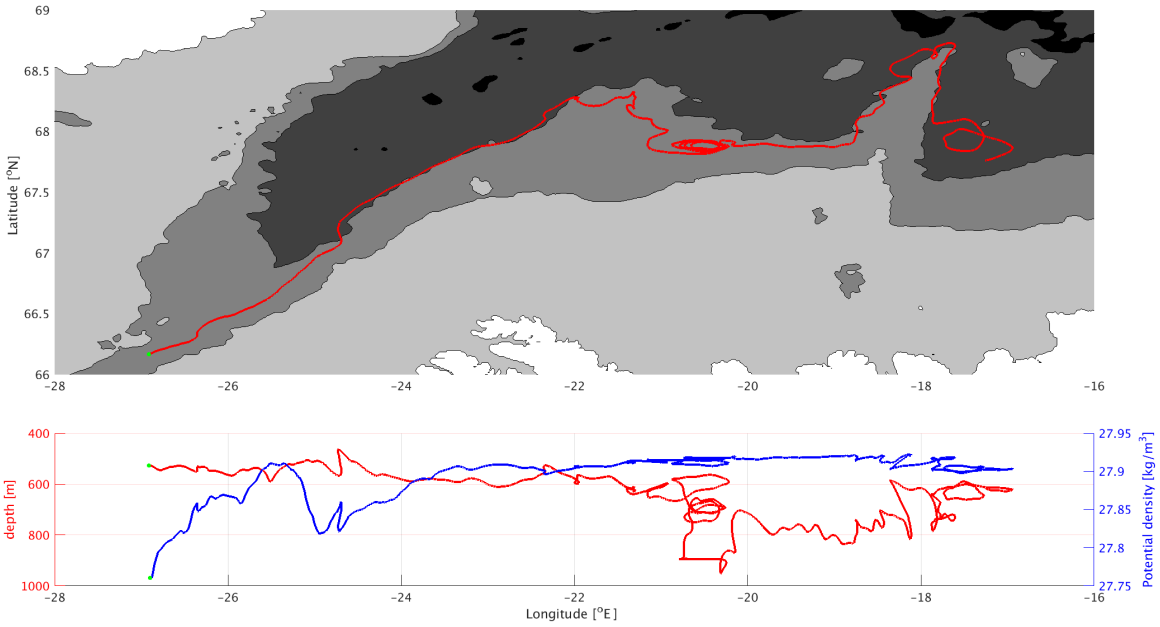

Figure 5.4: One example of a trajectory in red, launched at 01-02-2010 (and integrated backwards in time) at 525 meters, part of the B-DS. Isobaths are drawn every 500 meters, related to the colours at the map. The green dot correspond to the launch position (backward tracking). At the right y-axis, corresponding values of salinity are shown, related to the blue line.

5.4 Recommendations

The connection between the east side and west side of the KR with the corresponding hydrographic properties and its mechanisms is still questioned. Subsequently, the source of the NIJ is still unclear. To obtain more information of the origin of pathways of the DSOW, the origin of the difference between model data and observational data should be further investigated.

Overall, eddies which were fixed over time due to the topography and moving eddies north of the DS appear to be more significant for the changes in pathways of the DSOW than earlier assumed. It might be interesting if a model with a smaller resolution can be applied to trace smaller eddies. For example, this can be reached by obtaining a smaller resolution of the altimetry. Additionally, the hydrographic properties within the eddies can play an important role by tracking of the water masses. To confirm or reject the results of this project, which were based on model data, more observations of smaller scale eddies can be performed and investigated. If the existence of eddies is clear, the mechanisms of formation of eddies should be figured out to investigate the relevance for the DSOW and possibly the AMOC.

6. Conclusion

In this chapter, conclusions are described by answering the sub questions of this project:

- *What is the role of the separated East Greenland Current and the North Icelandic Jet?*

  The results show the connection between the DSOW and the East Greenland Current (EGC), but do not show a stable main pathway over time between these. Pathways showed strong variation on monthly time scales rather than inter-annual time scales. Because of this, we think that processes on smaller time and length scales are more important than assumed previously.

  At times, a connection of the EGC with the sEGC or the NIJ occurs. At other times, the EIC is diverted from the EGC. In this case, some particles return near the Iceland shelf and flow back into the westward direction, to the KR. Contrary to the results of De Jong et al. [2018], we do see a connection between the east side of the KR, possibly due to the higher number of particles released in this study over a larger time series. However, the source of the NIJ in this study is not the Iceland Sea gyre as suggested by Våge et al. [2011], but the EIC. No clear connection between the DSOW and the Iceland Sea gyre is found within the 400 days tracks of the particles.

- *What are the corresponding hydrographic properties?*

  Several currents like the EGC, shEGC, sEGC, NIJ and EIC are recognizable by hydrographic properties. An example is the relatively warm and saline rAW mass which flows in the EGC. Pathways which originate from the EGC seem to have relatively saline water, compared to the surroundings. Additionally, it appears that the warmer path of the DSOW originates from the EGC, and the colder path from the NIJ. The NIJ is recognizable by the denser water which is found in the results of hydrographic properties of the released particles. Additionally, no difference in temperature between the east and west side of the KR is recognizable in these results. Since some particles of the EIC return to the KR, the hydrographic properties of the water mass which flows from the west side to the east side of the KR are still questioned.

- *What is the driving force behind changes of the pathways over time?*

  Since we found a variability on monthly time scales, this research investigated mesoscale eddies and their influence at two locations. First, the area around the DS is investigated, where relatively many anticyclonic eddies are found compared to the entire study area. The intermittent occurrence of eddies shows a strong relation with volume transport to the DS, as shown by potential vorticity and potential density. Relatively high temperatures are found at the centers of mostly anticyclonic eddies and consequently the center of the eddy is less dense, compared to the surroundings. Second, a smaller area near the SFZ is investigated. The strengthening of an eddy, which appears to be locked due to the topography, is found to be related to the diversion from the EGC into the EIC.

Results of this project indicate that eddies are likely to be one of the responsible mechanisms for the variability of the sources and pathways into the DS. To investigate if this is indeed the case, a confirmation by observational research is recommended, as well as further research into the possible mechanisms behind these eddies.

Bibliography

Almansi, M., Haine, T. W., Pickart, R. S., Magaldi, M. G., Gelderloos, R., and Mastropole, D. (2017). High-frequency variability in the circulation and hydrography of the denmark strait overflow from a high-resolution numerical model. *Journal of Physical Oceanography*, 47(12):2999–3013.

Assassi, C., Morel, Y., Vandermeirsch, F., Chaigneau, A., Pegliasco, C., Morrow, R., Colas, F., Fleury, S., Carton, X., Klein, P., et al. (2016). An index to distinguish surface-and subsurface-intensified vortices from surface observations. *Journal of Physical Oceanography*, 46(8):2529–2552.

Behrens, E., Våge, K., Harden, B., Biastoch, A., and Böning, C. W. (2017). Composition and variability of the d enmark s trait o verflow w ater in a high-resolution numerical model hindcast simulation. *Journal of Geophysical Research: Oceans*, 122(4):2830–2846.

Brown, R. E. and Dickson, J. G. (1994). *Swainson's Warbler: Limnothlypis Swainsonii*. American Ornithologists' Union.

Bruce, J. (1995). Eddies southwest of the denmark strait. *Deep Sea Research Part I: Oceanographic Research Papers*, 42(1):13–29.

Center, N. G. D. (2006). 2-minute gridded global relief data (etopo2) v2.

Cushman-Roisin, B. and Beckers, J.-M. (2011). *Introduction to geophysical fluid dynamics: physical and numerical aspects*, volume 101. Academic press.

de Jong, M. F., Søiland, H., Bower, A. S., and Furey, H. H. (2018). The subsurface circulation of the iceland sea observed with rafos floats. *Deep Sea Research Part I: Oceanographic Research Papers*, 141:1–10.

Delandmeter, P. and van Sebille, E. (2019). The parcels v2. 0 lagrangian framework: new field interpolation schemes. *Journal of Physical Oceanography*.

Dickson, R. R. and Brown, J. (1994). The production of north atlantic deep water: sources, rates, and pathways. *Journal of Geophysical Research: Oceans*, 99(C6):12319–12341.

Foldvik, A., Aagaard, K., and Tørresen, T. (1988). On the velocity field of the east greenland current. *Deep Sea Research Part A. Oceanographic Research Papers*, 35(8):1335–1354.

Harden, B. E., Pickart, R. S., Valdimarsson, H., Våge, K., de Steur, L., Richards, C., Bahr, F., Torres, D., Børve, E., Jónsson, S., et al. (2016). Upstream sources of the denmark strait overflow: Observations from a high-resolution mooring array. *Deep Sea Research Part I: Oceanographic Research Papers*, 112:94–112.

Håvik, L., Pickart, R. S., Våge, K., Torres, D., Thurnherr, A. M., Beszczynska-Möller, A., Walczowski, W., and von Appen, W.-J. (2017). Evolution of the east greenland current from fram strait to denmark strait: Synoptic measurements from summer 2012. *Journal of Geophysical Research: Oceans*, 122(3):1974–1994.

Helland-Hansen, B. and Nansen, F. (1909). *The Norwegian Sea: its physical oceanography based upon the Norwegian researches 1900-1904*. Det Mallingske Bogtrykkeri.

Huang, J., Pickart, R. S., Valdimarsson, H., Lin, P., Spall, M. A., and Xu, F. (2019). Structure and variability of the north icelandic jet from two years of mooring data. *Journal of Geophysical Research: Oceans*.

Jochumsen, K., Moritz, M., Nunes, N., Quadfasel, D., Larsen, K. M., Hansen, B., Valdimarsson, H., and Jonsson, S. (2017). Revised transport estimates of the d enmark s trait overflow. *Journal of Geophysical Research: Oceans*, 122(4):3434–3450.

Jochumsen, K., Quadfasel, D., Valdimarsson, H., and Jónsson, S. (2012). Variability of the denmark strait overflow: Moored time series from 1996–2011. *Journal of Geophysical Research: Oceans*, 117(C12).

Jónsson, S. (1999). The circulation in the northern part of the denmark strait and its variability. *ICES CM*, 50:06.

Jónsson, S. (2007). Volume flux and fresh water transport associated with the east icelandic current. *Progress in Oceanography*, 73(3-4):231–241.

Köhl, A. (2010). Variable source regions of denmark strait and faroe bank channel overflow waters. *Tellus A: Dynamic Meteorology and Oceanography*, 62(4):551–568.

Köhl, A., Käse, R. H., Stammer, D., and Serra, N. (2007). Causes of changes in the denmark strait overflow. *Journal of physical oceanography*, 37(6):1678–1696.

Kuhlbrodt, T., Griesel, A., Montoya, M., Levermann, A., Hofmann, M., and Rahmstorf, S. (2007). On the driving processes of the atlantic meridional overturning circulation. *Reviews of Geophysics*, 45(2).

Lilly, J. M. and Rhines, P. B. (2002). Coherent eddies in the labrador sea observed from a mooring. *Journal of Physical Oceanography*, 32(2):585–598.

Lilly, J. M., Rhines, P. B., Schott, F., Lavender, K., Lazier, J., Send, U., and D'Asaro, E. (2003). Observations of the labrador sea eddy field. *Progress in Oceanography*, 59(1):75–176.

Macrander, A., Send, U., Valdimarsson, H., Jónsson, S., and Käse, R. H. (2005). Interannual changes in the overflow from the nordic seas into the atlantic ocean through denmark strait. *Geophysical Research Letters*, 32(6).

Macrander, A., Valdimarsson, H., and Jónsson, S. (2014). Improved transport estimate of the east icelandic current 2002–2012. *Journal of Geophysical Research: Oceans*, 119(6):3407–3424.

Marshall, J., Jones, H., and Hill, C. (1998). Efficient ocean modeling using non-hydrostatic algorithms. *Journal of Marine systems*, 18(1-3):115–134.

Mastropole, D., Pickart, R. S., Valdimarsson, H., Våge, K., Jochumsen, K., and Girton, J. (2017). On the hydrography of denmark strait. *Journal of Geophysical Research: Oceans*, 122(1):306–321.

Mauritzen, C. (1996). Production of dense overflow waters feeding the north atlantic across the greenland-scotland ridge. part 1: Evidence for a revised circulation scheme. *Deep Sea Research Part I: Oceanographic Research Papers*, 43(6):769–806.

McDougall, T. J. and Barker, P. M. (2011). Getting started with teos-10 and the gibbs seawater (gsw) oceanographic toolbox. *SCOR/IAPSO WG*, 127:1–28.

Nencioli, F., Dong, C., Dickey, T., Washburn, L., and McWilliams, J. C. (2010). A vector geometry–based eddy detection algorithm and its application to a high-resolution numerical model product and high-frequency radar surface velocities in the southern california bight. *Journal of Atmospheric and Oceanic Technology*, 27(3):564–579.

National Geophysical Data Center, NOAA (2006). 2-minute gridded global relief data (ETOPO2) v2

Pickart, R. S., Spall, M. A., Torres, D. J., Våge, K., Valdimarsson, H., Nobre, C., Moore, G., Jonsson, S., and Mastropole, D. (2017). The north icelandic jet and its relationship to the north icelandic irminger current. *Journal of Marine Research*, 75(5):605–639.

Rossby, T., Dorson, D., and Fontaine, J. (1986). The rafos system. *Journal of atmospheric and oceanic technology*, 3(4):672–679.

Rudels, B., Eriksson, P., Buch, E., Budéus, G., Fahrbach, E., Malmberg, S.-A., Meincke, J., and Mälkki, P. (2003). Temporal switching between sources of the denmark strait overflow water. In *ICES Mar. Sci. Symp*, volume 219, pages 319–325.

Rudels, B., Eriksson, P., Grönvall, H., Hietala, R., and Launiainen, J. (1999). Hydrographic observations in denmark strait in fall 1997, and their implications for the entrainment into the overflow plume. *Geophysical Research Letters*, 26(9):1325–1328.

Rudels, B., Fahrbach, E., Meincke, J., Budéus, G., and Eriksson, P. (2002). The east greenland current and its contribution to the denmark strait overflow. *ICES Journal of Marine Science*, 59(6):1133–1154.

Saberi, A., Haine, T.W.N., Gelderloos, R., De Jong, F., Furey, H. and Bower, A.(2019). Lagrangian Perspective on the Origins of Denmark Strait Overflow *submitted*.

Swift, J. H., Aagaard, K., and Malmberg, S.-A. (1980). The contribution of the denmark strait overflow to the deep north atlantic. *Deep Sea Research Part A. Oceanographic Research Papers*, 27(1):29–42.

Våge, K., Pickart, R. S., Spall, M. A., Moore, G., Valdimarsson, H., Torres, D. J., Erofeeva, S. Y., and Nilsen, J. E. Ø. (2013). Revised circulation scheme north of the denmark strait. *Deep Sea Research Part I: Oceanographic Research Papers*, 79:20–39.

Våge, K., Pickart, R. S., Spall, M. A., Valdimarsson, H., Jónsson, S., Torres, D. J., Østerhus, S., and Eldevik, T. (2011). Significant role of the north icelandic jet in the formation of denmark strait overflow water. *Nature Geoscience*, 4(10):723.

Valdimarsson, H. and Malmberg, S.-A. (1999). Near-surface circulation in icelandic waters derived from satellite tracked drifters. *Rit Fiskideild*, 16:23–40.

van Aken, H. M. and de Jong, M. F. (2012). Hydrographic variability of denmark strait overflow water near cape farewell with multi-decadal to weekly time scales. *Deep Sea Research Part I: Oceanographic Research Papers*, 66:41–50.

von Appen, W.-J., Mastropole, D., Pickart, R. S., Valdimarsson, H., Jónsson, S., and Girton, J. B. (2017). On the nature of the mesoscale variability in denmark strait. *Journal of Physical Oceanography*, 47(3):567–582.

Ypma, S., Brüggemann, N., Georgiou, S., Spence, P., Dijkstra, H., Pietrzak, J., and Katsman, C. (2019). Pathways and watermass transformation of atlantic water entering the nordic seas through denmark strait in two high resolution ocean models. *Deep Sea Research Part I: Oceanographic Research Papers*.

Zhao, J., Yang, J., Semper, S., Pickart, R. S., Våge, K., Valdimarsson, H., and Jónsson, S. (2018). A numerical study of interannual variability in the north icelandic irminger current. *Journal of Geophysical Research: Oceans*, 123(12):8994–9009.

Appendices

A. Definitions

Several definitions are used in this project and explained in this chapter.

A.1 Normalizing

A.1.1 Normalizing of a dataset on a map

Normalization in the context of a map is realized by dividing the numbers through the maximum counted particles in the grid, which is defined as:

$$x_i = \frac{A_i}{max(A)}$$

A are all the grid values of a map, "max" is defined as the maximum value within A and "min" is defined as the minimum value in A.

A.1.2 Normalizing of a 2D-dataset

Normalization in the context of 2D data, is realized by scaling the range of the data to [0,1], which is defined as:

$$x_i = \frac{A_i}{max(A) - min(A)} + \frac{|min(A)|}{max(A) - min(A)}$$

As described at https://nl.mathworks.com/help/matlab/ref/double.normalize.html.

A.2 Standard deviation

For a random variable vector A made up of N scalar observations, the standard deviation is defined as:

$$S = \sqrt{\frac{1}{N-1}\sum_{i=1}^{N}|A_i - \mu|^2}$$

μ is the mean of A:

$$\mu = \frac{1}{N}\sum_{i=1}^{N} A_i$$

As described at https://nl.mathworks.com/help/matlab/ref/std.html.

A.3 Volume transport

Values of volume transport are calculated for particular sections at certain times, which is defined as:

$$Volume\ Transport = u_{across} * Area$$

Where u_{across} is the perpendicular mean velocity $[m/s]$ and the area $[m^2]$ is taken over a transect, between two certain depths. These quantities will give the volume transport $[m^3/s]$.

A.4 Pearson correlation coefficient

The correlation coefficient of two random variables is a measure of their linear dependence. If each variable has N scalar observations, then the Pearson correlation coefficient is defined as:

$$\rho(A,B) = \frac{1}{N-1}\sum_{i=1}^{N}\overline{\left(\frac{A_i-\mu_A}{\sigma_A}\right)\left(\frac{B_i-\mu_B}{\sigma_B}\right)}$$

μ_A and σ_A are the mean and standard deviation of A, respectively, μ_B and σ_B are the mean and standard deviation of B. As described at https://nl.mathworks.com/help/matlab/ref/corrcoef.html, where they used the references: [Fisher, R.A., 1958]; [Kendall, M.G, 1979]; [Press, W.H. et. all., 1992].

B. Additional examples diversion B-EGC

Two examples of the diversion during the B-EGC are already shown in section 4.2. In this appendix, four more examples are shown to visualize the diversion. Figure B.1 and Figure B.2 show particles which are preferably going south-eastward, while Figure B.4 and Figure B.3 show results of particles which are flowing south-westward into the DS.

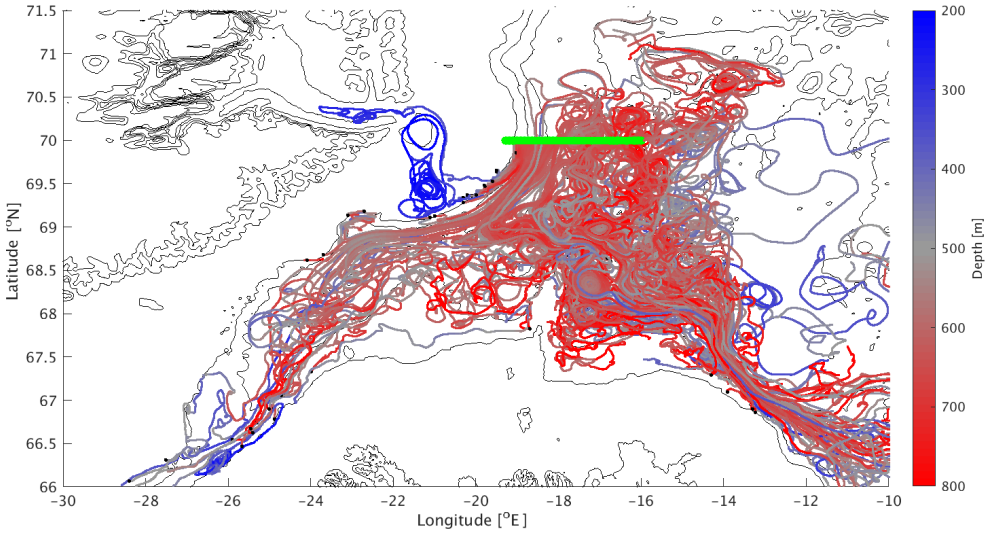

Figure B.1: Similar to Figure 4.5. Particle trajectories of a release date, as part of the B-EGC. Green dots correspond to the release coordinates of the particles. Small black dots correspond to a location where particles are "stuck" (see text) in section 4.2. Colours indicating the depth which particles reach. In this case, the launch date of particles is 01-12-2005. Adding 115 days to calculate the date where particles probably pass the investigated area is 26-03-2006, as described in section 4.4.3. Particles are considered to go relatively often to the south-east direction.

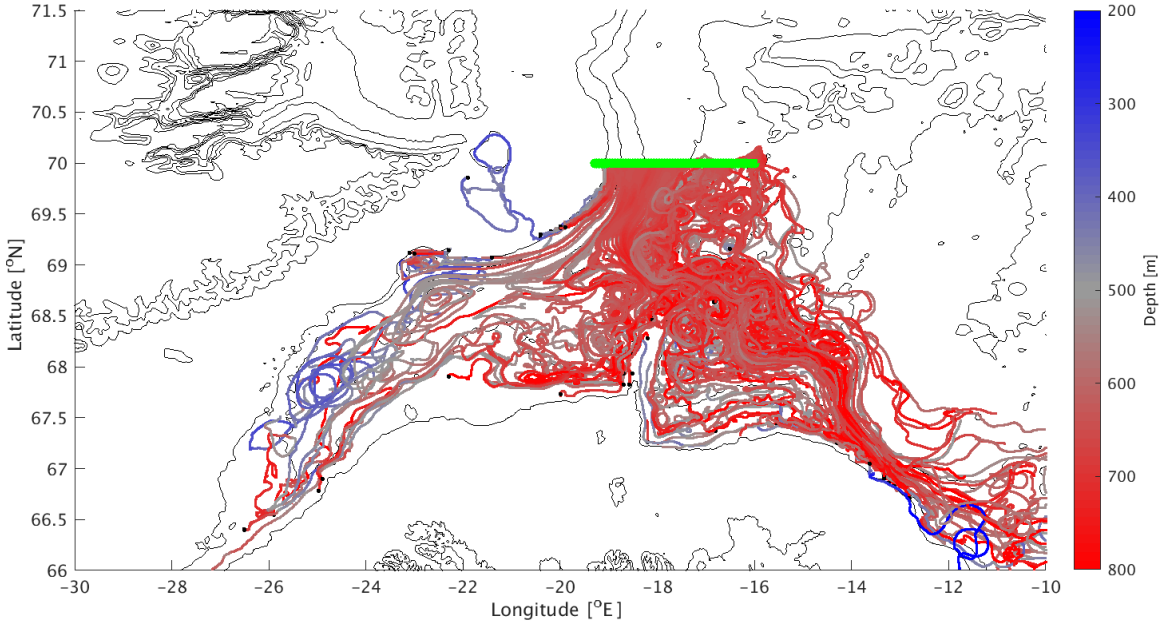

Figure B.2: Similar to Figure B.1. In this case the launch date of particles is 01-10-2008 and the date where particles probably pass the investigated area of section 4.4.3 is 24-01-2009. Particles are considered to go relatively often to the south-west direction.

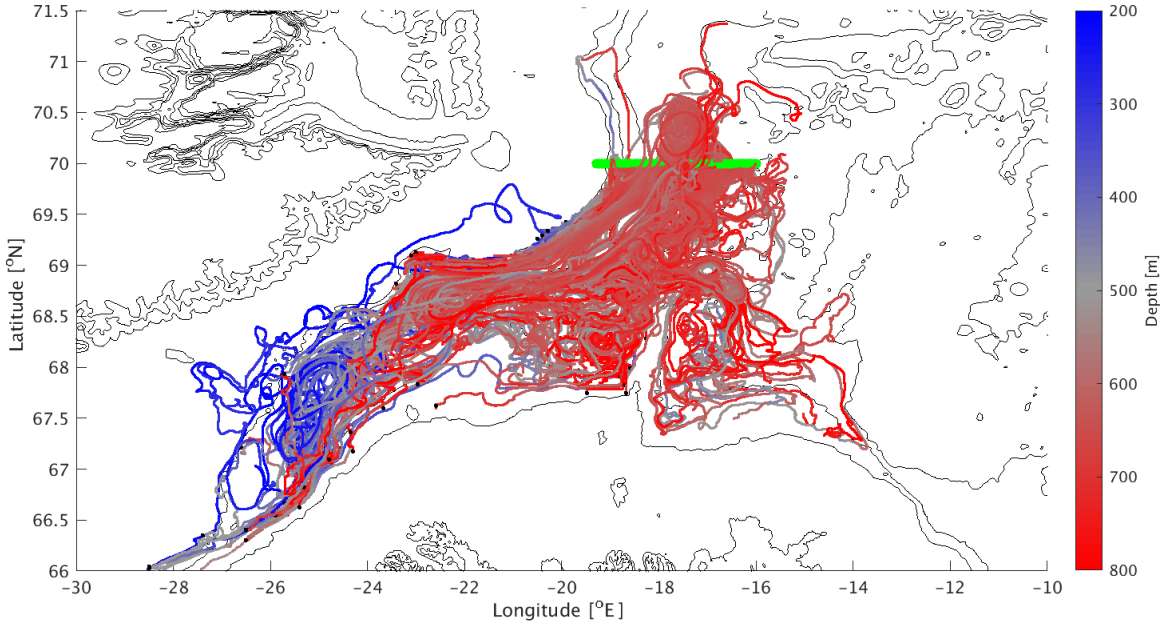

Figure B.3: Similar to Figure B.1. In this case the launch date of particles is 01-08-2010 and the date where particles probably pass the investigated area of section 4.4.3 is 24-11-2010. Particles are considered to go relatively often to the south-west direction.

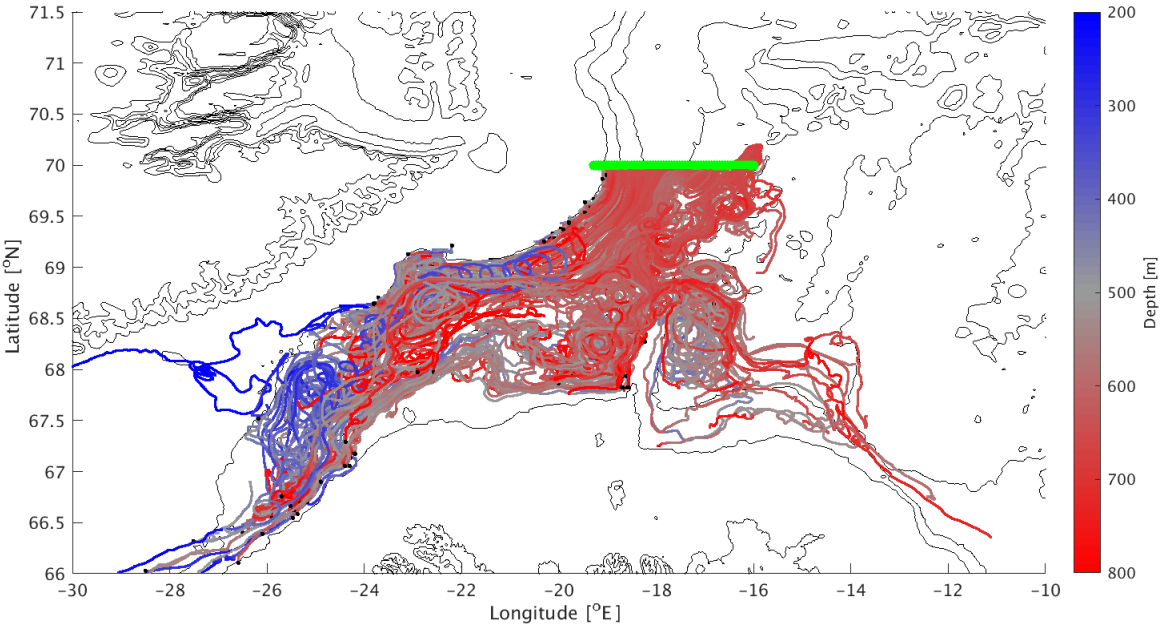

Figure B.4: Similar to Figure B.1. In this case the launch date of particles is 01-12-2009 and the date where particles probably pass the investigated area of section 4.4.3 is 26-03-2010.